Computational Virtual Measurement For Trees

Dissertation

Zur Erlangung des akademischen Grades doctor rerum naturalium

(Dr. rer. nat.)

Vorgelegt dem Rat der Chemisch-Geowissenschaftlichen Fakultät der Friedrich-Schiller-Universität Jena

von MSc. Zhichao Wang
geboren am 16.03.1987 in Beijing, China

Gutachter:

1. _____

2. _____

3. _____

Tag der Verteidigung: _____

我们的征途是星辰大海

My Conquest Is the Sea of Stars

--2019，长征五号遥三运载火箭发射

わが征くは星の大海

--1981，田中芳樹

Wir aber besitzen im Luftreich des Traums
Die Herrschaft unbestritten
--1844, Heinrich Heine

That I lived a full life
And one that was of my own choice
--1813, James Elroy Flecker

Contents

List of Figures

List of Tables

List of Symbols and Abbreviations

AGB	Above ground biomass
ALS	Airborne LiDAR scanning
AMDS	Artificial multiple data sources
AVG	Average value
BQP	Basic quasi physical
CA	Cellular automata
CM	Computational modeling
CVGE	Collaborative VGE
CVM	Computational virtual measurement
DBH	Diameter at breast height
DBSCAN	Density-based spatial clustering of applications with noise
DVGE	Distributed VGE
FAO	Food and Agriculture Organization of the United Nations
FPS	Frames per second
FRA	Global Forest Resources Assessment
GeoWeb	Geospatial web
GML	Geography markup languages
GSV	Growing stock volume
ICESat/GLAS	Ice, Cloud, and land Elevation Satellite with a Geosciences Laser Altimeter System
IDE	Integrated development environment
IMU	Inertial measurement units
LiDAR	Light detection and ranging
LoD	Levels of details
MBP	Multi box pruning
NFI	National forest inventory
OpenGIS	Open Geodata Interoperation Specification
PCA	Principal components analysis

pcd	Point cloud density
PCL	Point Cloud Library
PS	Phase shift
QSM	Quantitative structure model
RMSE	Root mean square error
RSD	Relative standard deviation
SAP	Sweep-and-prune
SDK	Software development kit
SFI	Stand-level forest inventory
SFM	Sustainable forest management
SfM	Structure from Motion
SDMS	Single-multiple data sources
STDEV	Standard deviation
T26	Tree No.26
T27	Tree No.27
TLS	Terrestrial LiDAR scanning
ToF	Time-of-flight
UAS	Unmanned aircraft systems
UAV	Unmanned aerial vehicle
VGE	Virtual geographic environment
VLS	Vehicle LiDAR scanning
VMT	Virtual measurement for trees
VNFI	Virtual NFI
VSE	Virtual social environment
VSP	Virtual sample plot
VWD	Virtual water displacement
VWM	Virtual water molecule
ZY3-02	Ziyuan3-02 satellite

Acknowledgments

I am incredibly grateful to Prof. Dr. Christiane Schmullius for supervision and for providing excellent research environments in the EO department of Uni-Jena. I benefited a lot from your motivation, suggestions, and comments. Your point-of-review and suggestions always helped me to keep moving forward efficiently and upgrade the papers to a higher level. You guided me on how to improve the manuscripts in a scientific way. The most important was that you provided me free spiritual and physical spaces, i.e., a conceptual playground and a cozy office, to develop the independent theory of computational virtual measurement. Although, lots of pains were on the way, you helped me to conquer.

I am incredibly grateful to Prof. Baitian Wang and Professorate senior engineer Yanli Zou for parenting. The title of doctor will be an final end of being a student for me. I thank your accompanying in this long journey. Although your names will not be in my co-author list, your thoughts are deeply rooted in this thesis and will continue influencing my future works.

I would like to thank Prof. Jia Wang in Beijing Forestry University and Dr. Xinlian Liang in Finnish Geospatial Research Institute for the wonderful collaboration on forest field measurements and supports in the development of the sunlight analysis method. Your excellent ideas were of vital importance in this work.

I would like to thank Dr. Jan Hackenberg, who graduated from Uni Freiburg, Germany. I still remember the day you sent me your video tutorial for processing tree models, although it was about five years ago. Your open-source software helps people in forest inventory over the world.

I can never give sufficient thanks to all my colleagues for your participation in my talks every time. Although my theory was a bit away from your specialty on remote sensing, you always tried best to offer help. You are Christian Berger, Christian Thiel, Cremer Felix, Dubois Clémence, Eckardt Robert, Glaser Andreas, Habenstein Annett, Heckel Kai, Jussi

Abstract

National forest inventory (NFI) is a systematic sampling method to collect forest information, including tree parameters, site conditions, and auxiliary data. The sample plot measurement is the key work in NFI. However, compared to the techniques 100 years ago, measuring methods and data‑processing (modeling) approaches for NFI sample plots have been improved to a minor extent. The limit was that the newly-developed methods introduced additional validation workflows and would increase the workload in NFI. That was due to that these methods were usually developed based on species-specific and site-specific strategies. In order to overcome these obstacles, the integration of the novel measuring instruments is in urgent need, e.g., light detection and ranging (LiDAR) and the corresponding data processing methods with NFI.

Given these situations, this thesis proposed a novel computational virtual measurement (CVM) method for the determination of tree parameters without the need for validation. Primarily, CVM is a physical simulation method and works as a virtual measuring instrument. CVM measures raw data, e.g., LiDAR point clouds and tree models, by the simulation of the physical mechanism of measuring instruments and natural phenomena. Based on the theory of CVM, this thesis is a systematic description of how to develop virtual measuring instruments.

The first work is to introduce the CVM theory. CVM is a conceptual and general methodology, which is different from a specific measurement of tree parameters. Then, the feasibility of CVM was tested using a conceptual implementation, i.e., virtual ruler. The development of virtual ruler demonstrated the two key differences between CVM and conventional modeling methods. Firstly, the research focus of CVM is to build an appropriate physical scenario instead of finding a mathematical relationship between modeling results and true values. Secondly, the CVM outputs can approach true values, whereas the modeling results could not. Consequently, in a virtual space, tree parameters

are determined by a measuring process without mathematical predictions. Accordingly, the result is free of validation and can be regarded as true values, at least in virtual spaces.

With the knowledge from the virtual ruler development, two exceptional implementations are further developed. They are the virtual water displacement (VWD) method and sunlight analysis method. Both of them employ the same CVM workflow, which is firstly measured in reality and secondly measured in virtual space.

The VWD aims to virtually measure the point clouds using the simulation of water displacement methods in reality. There are two stages in this method. The first stage is to apply the simulation of water displacement using massive virtual water molecules (VWMs). Some empirical regressions have to be employed in this stage, due to the limitation of computer performance. In the second stage, a single (or few) VWM (or VWMs) is developed to remove those empirical processes in VWD. Finally, VWD can function as a fully automatic method to measure point clouds.

The sunlight analysis method aims to virtually measure the tree models using the simulation of solar illumination during daylight. There are also two stages in this method. The first stage is to develop sunlight analysis for a single tree. The second stage is to analyze the interference from neighboring trees. The results include default tree attributes, which can be collected in the future NFI.

The successful developments of CVM, along with implementations of VWD and sunlight analysis methods, prove the initial assumptions in this thesis. It is the conversion of mathematical processing of data into virtual measurements. Accordingly, this is a different philosophy, i.e., the role of data is extended to the digital representative of trees. It opens an avenue of data processing using a more natural approach and is expected to be employed in the near future as a standard measuring instrument, such as a diameter tape, in NFI.

Zusammenfassung

Die Nationale Waldinventur (NFI) ist eine systematische Stichprobenmethode zur Erfassung von Waldinformationen, einschließlich Baumparameter, Standortbedingungen und Hilfsdaten. Die Messung von Stichprobenparzellen ist die Schlüsselarbeit der NFI. Im Vergleich zu den Techniken vor 100 Jahren wurden die Messmethoden und Datenverarbeitungsansätze (Modellierung) für NFI-Stichprobenparzellen jedoch in geringem Umfang verbessert. Die Grenze lag darin, dass die neu entwickelten Methoden zusätzliche Validierungsabläufe einführten und den Arbeitsaufwand in der NFI erhöhen würden. Dies war darauf zurückzuführen, dass diese Methoden in der Regel auf der Grundlage art- und standortspezifischer Strategien entwickelt wurden. Um diese Hindernisse zu überwinden, ist die Integration der neuartigen Messinstrumente dringend erforderlich, z.B. Light Detection and Ranging (LiDAR) und die entsprechenden Datenverarbeitungsmethoden mit NFI.

Vor diesem Hintergrund wird in dieser Arbeit ein neuartiges rechnergestütztes virtuelles Messverfahren (CVM) zur Bestimmung von Baumparametern ohne Validierungsbedarf vorgeschlagen. CVM ist in erster Linie eine physikalische Simulationsmethode und arbeitet als virtuelles Messinstrument. CVM misst Rohdaten, z.B. LiDAR-Punktwolken und Baummodelle, durch die Simulation des physikalischen Mechanismus von Messinstrumenten und Naturphänomenen. Basierend auf der Theorie des CVM ist diese Arbeit eine systematische Beschreibung, wie virtuelle Messinstrumente entwickelt werden können.

Die erste Arbeit dient der Einführung in die Theorie des CVM. CVM ist eine konzeptuelle und allgemeine Methodik, die sich von einer spezifischen Messung von Baumparametern unterscheidet. Anschliessend wird die Durchführbarkeit des CVM anhand einer konzeptuellen Implementierung, d.h. eines virtuellen Lineals, getestet. Die Entwicklung des virtuellen Lineals zeigte die beiden Hauptunterschiede zwischen CVM und konventionellen Modellierungsmethoden auf. Erstens besteht der

Forschungsschwerpunkt von CVM darin, ein geeignetes physisches Szenario zu erstellen, anstatt eine mathematische Beziehung zwischen Modellierungsergebnissen und wahren Werten zu finden. Zweitens können sich die Ergebnisse des CVM den wahren Werten annähern, während die Modellierungsergebnisse dies nicht konnten. Folglich werden in einem virtuellen Raum die Baumparameter durch einen Messprozess ohne mathematische Vorhersagen bestimmt. Dementsprechend ist das Ergebnis frei von Validierung und kann, zumindest in virtuellen Räumen, als wahre Werte betrachtet werden.

Mit dem Wissen aus der Entwicklung des virtuellen Lineals werden zwei aussergewöhnliche Implementierungen weiterentwickelt. Es handelt sich um die Methode der virtuellen Wasserverdrängung (VWD) und die Methode der Sonnenlichtanalyse. Beide verwenden den gleichen CVM-Workflow, der erstens in der Realität und zweitens im virtuellen Raum gemessen wird.

Das VWD zielt darauf ab, die Punktwolken virtuell zu messen, wobei die Simulation von Wasserverdrängungsmethoden in der Realität verwendet wird. Diese Methode besteht aus zwei Stufen. Die erste Stufe besteht in der Anwendung der Simulation der Wasserverdrängung unter Verwendung massiver virtueller Wassermoleküle (VWMs). Aufgrund der begrenzten Computerleistung müssen in dieser Phase einige empirische Regressionen angewandt werden. In der zweiten Stufe wird ein einzelnes (oder wenige) VWM (oder VWMs) entwickelt, um diese empirischen Prozesse im VWD zu entfernen. Schließlich kann VWD als vollautomatische Methode zur Messung von Punktwolken fungieren.

Die Methode der Sonnenlichtanalyse zielt darauf ab, die Baummodelle virtuell zu messen, indem die Simulation der Sonneneinstrahlung bei Tageslicht verwendet wird. Auch bei dieser Methode gibt es zwei Stufen. In der ersten Stufe wird die Sonnenlichtanalyse für einen einzelnen Baum entwickelt. Die zweite Stufe ist die Analyse der Interferenz von benachbarten Bäumen. Die Ergebnisse umfassen Standard-Baumattribute, die in der zukünftigen NFI gesammelt werden können.

Die erfolgreichen Entwicklungen von CVM, zusammen mit Implementierungen von VWD- und Sonnenlichtanalysemethoden, beweisen die anfänglichen Annahmen in dieser Arbeit. Es handelt sich um die Umsetzung der mathematischen Verarbeitung von Daten in virtuelle Messungen. Dementsprechend handelt es sich um eine andere Philosophie, d.h. die Rolle der Daten wird auf die digitale Darstellung von Bäumen ausgedehnt. Sie eröffnet einen Weg der Datenverarbeitung unter Verwendung eines natürlicheren Ansatzes und wird voraussichtlich in naher Zukunft als Standard-Messinstrument, wie z.B. ein Durchmesser-Band, in der NFI eingesetzt werden.

Chapter One

Study Objectives

1.1 Forest inventory and modeling methods

Forests are significant for both ecosystems and human economics. Various ecological balances on earth, e.g., carbon sink, biodiversity conservation, and climate stabilization, rely on forests. Meanwhile, people harvest food, fuel, and building materials from forests to meet humanity's expanding needs of resources [1]. Unfortunately, people had no awareness of the importance of forest conservation over a long period of time in history. So far, lots of human activities in forests still lead to deforestation [2]. Harvesting of trees happens instantaneously. On the contrary, the recovery process of forests takes decades or even longer [3]. Forests loss from 1990 to 2015 was estimated at 129 Mha, which took 3% of global forest cover [4]. The impact of deforestation is significant for global climate change and carbon-cycle because of the release of a huge amount of CO_2 [5]. Therefore, keeping a balance between human consumption of forest resources and protecting the ecological function of forests is of vital importance nowadays.

Aiming at this, sustainable forest management (SFM), one of the methods for forest management under the framework of the Global Forest Resources Assessment (FRA), was proposed by the Food and Agriculture Organization of the United Nations (FAO) since 1948 [6]. The overall goal of SFM is to maintain forests' economic, ecological, and social values, at the same time, to keep them continuously beneficial both to humans and nature [7]. Forest inventory is a key method to provide comprehensive forest information to support a successful SFM. National forest inventory (NFI), nationwide forest inventory, was taken by 112 countries since 2014 and covered 81% of the global forest area [8]. Well-developed NFI systems in some countries in Europe, North America, the Caribbean, East Asia, and Western-central Asia led to the expansion of forest areas nationwide. However, deforestation still happened on the global scale [4,9].

Technically, forest inventory and NFI are sample-based statically ground sampling methods to collect tree (forest) parameters [10]. The Tree parameters, e.g., diameter at breast height (DBH), tree height (H), stem volume, and above ground biomass (AGB), are

significant indicators for tree status and forest conditions [11]. Some of the tree parameters can be directly determined from measuring instruments without additional mathematical processes. For example, DBH is measured using a diameter tape, which physically contacts stem surfaces. Due to the definition of DBH, the raw reading from the diameter tape is usually regarded as true values [12]. Compared to the measuring of DBH, the measuring of stem volume is much more complicated because conventional measuring methods are hard to record complicated tree structures precisely [13-15]. Therefore, modeling methods are employed to further deal with raw readings from measuring instruments.

Modeling is a powerful mathematical tool, which predicts the required parameters from other quantities. In forest inventory, allometric methods are widely used modeling tools used for the estimation of stem volume and AGB [13]. For example, the stem volume is usually regressed from several physical quantities, e.g., DBH and tree height [6]. In this modeling process, a tree (stem) is modeled using cones and cylinders. Nevertheless, the shape of allometric models significantly differs from the real tree. This geometrical difference between allometric models and real trees is insignificant for the stem volume estimation. Because the stem volume itself is a mathematic value that has no ability to restore the structural information of trees. Therefore, the allometric modeling accuracy can only be evaluated using the simple consistency of values between allometric models and ground truth references. Even though the allometric models contributed in forest inventory obviously, there is still one problem. The allometric methods are site-specific and tree species-specific. For decades, scientists devoted great efforts to produce specific allometric equations for numerous forest areas over the world [16].

With the development of new measuring technologies, e.g., LiDAR, millions of targets can be measured instantly in a forest sample plot [17,18]. The massive sampling quantities and tiny sampling spaces are two features in a LiDAR scanning [19]. In order to serve those new features of LiDAR measuring instruments, new data processing methods were developed [17,20,21]. Compared to conventional allometric methods, tree models derived from LiDAR data riched the tree model in tree geometry [22-27]. As shown in Fig.1-1,

Liang et al. classified tree models into five classes using Levels of Details (LoD), which were made by computational modeling (CM) methods [11]. LoD1 represented the roughest level of tree models, which contained the information of DBH and tree height only. Ascending by modeling richness, more details were added at each level based on the previous level. LoD2 models used few cones and cylinders to represent a tree stem, instead of raw tree parameters in LoD1 models. The change from LoD1 models to LoD2 models was similar to the modeling process of conventional allometric methods in the current NFI sample plot measurement. As shown in Fig.1-1(e), LoD5 models were the highest accurate models in CM methods. Meanwhile, the analytical methods in the current NFI sample plot measurement could provide similar tree models using destructive and labor-intensive approaches.
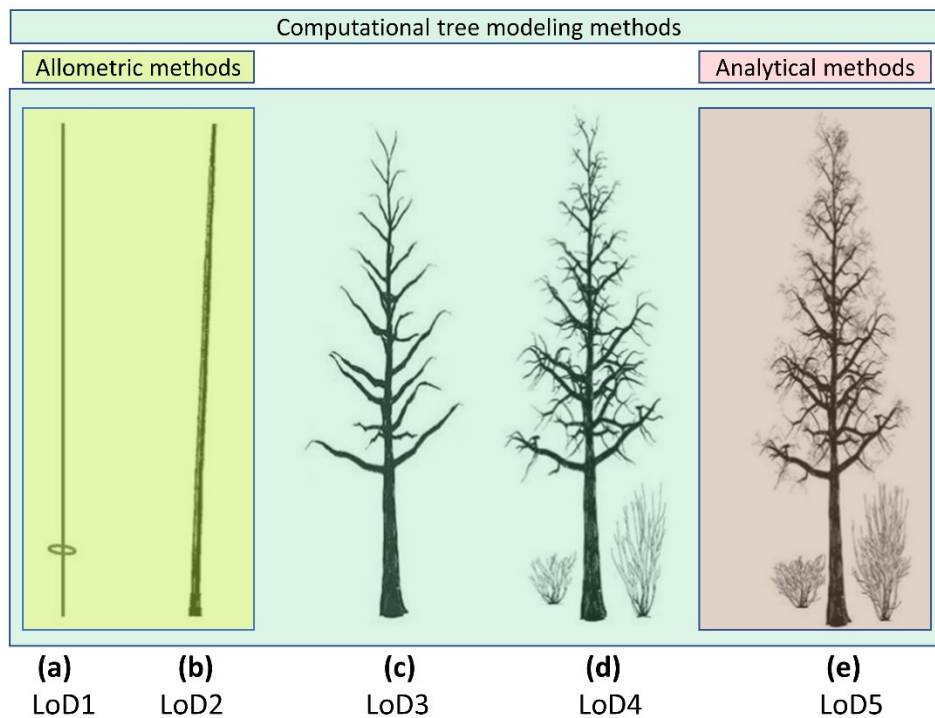
Figure 1-1. Levels of details (LoD) of tree models in CM methods [11] and the corresponding conventional methods in the current NFI sample plot measurement; (a-e) LoD1 to LoD5 models, ascending according to richness of tree structures; the yellow zone represents the modeling capability of conventional allometric methods; the red zone represents the modeling capability of conventional analytical methods; the green zone represents the modeling capability of computational modeling methods.

Theoretically, CM methods can provide all kinds of tree models, which are collected in the current NFI workflows. Reports of NFI workflows in five major countries, Canada, China, Finland, Germany and the USA, were reviewed [28-33]. However, no country utilizes LiDAR scanning and CM methods in the NFI sample plot measurement. Compared to measuring methods in the early NFI in northern Europe [34], little changes happened in measuring instruments and data processing methods. Why are the LiDAR scanning and CM methods excluded in NFI workflows? There must be a reason.

1.2 Dependency of methods and chain of validation

For many years, studies in forest inventory focus on how to improve estimation accuracy for a specific tree parameter. Despite the technological improvements in specific algorithms, the overall methodology is remaining. The fixed pattern of those studies was: (i) build a bridge connecting raw data with tree parameters, which was called as "modeling"; (ii) validation with additional ground truth reference. It was demonstrated that validation is a necessary step in any modeling methods at the algorithm level. The essence of modeling methods is to make mathematical predictions. However, how far the specific prediction is away from the true values remains unknown, when there is no ground truth reference. Therefore, all the modeling methods are dependent methods. They rely on additional data sources to develop and validate themself. As is well known, the growth of a tree is affected by various factors. Consequently, the effective domain of a model is limited to a specific forest area and specific tree species. Therefore, no matter how perfect of a bridge is, researchers have to build bridges repeatedly for any new forest area.

Besides the dependency of modeling methods, the chain of validation is also a problem. For allometric methods, their models are validated using another method, e.g., analytical methods. There is only one step in this validation chain. For CM methods, as shown in Fig.1-1, a CM tree model (LoD3 to LoD5) was superior to allometric models and provided more details in tree structures. However, many studies referred the ground truth values from allometric methods to evaluate modeling results using CM methods [24,25,35-37]. This

validation chain is considered to be inappropriate. There are two reasons: (i) CM methods have a high level of LoD. It should not use low LoD data sources as true values to validate high LoD models; (ii) the simple consistency on physical quantities, e.g., stem volume, has no relationship to the right distribution of tree structures.

Figure.1-2 shows the chain of validation for allometric methods and CM methods. Despite the impropriety of validation of CM methods using allometric methods, CM methods bring an additional validation step to the overall workflow of NFI sample plot measurements. If it is beneficial to include this additional step remains unknown.
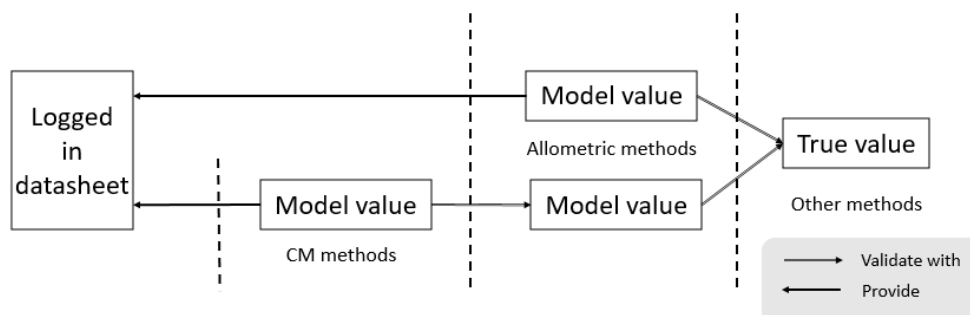
Figure 1-2. Chain of validation for allometric methods and CM methods.

1.3 Study objectives

The measuring techniques in forest inventory keep up with the rapid evolution. Compared to the plastic ruler in the early NFI in the 1920s, a LiDAR scanner has the capability to measure millions of objects in a sample plot instantly. However, the data processing methods, i.e., modeling methods, stay as they were in an early time. According to the findings in previous sections 1.2, there are three negative features of modeling methods for NFI. The first feature is that a modeling method cannot investigate a tree or forest parameters without additional methods to provide ground truth reference. The second feature is that modeling methods are highly tree species-specific and site-specific, which prevent the re-use of modeling results in another forest area. The third feature is that the development of modeling methods relies on destructive methods eventually, which provide

true value to train and to validate modeling methods.

Those negative features are born at the algorithm level. Attempts using modeling methods are not expected to get any improvements. Therefore, the objectives of this study are to discover novel data process methods to extract of tree and forest parameters. Meanwhile, these new methods are expected with the feature of validation-free and nonspecific to trees and site conditions.

Accordingly, two research questions are raised as follows:

1. Are there new methodologies to process raw data from forest sample plots, instead of modeling methods?

2. How many tree or forest parameters can be extracted using the potential new methods?

1.4 Thesis structure

This dissertation is formulated as a monograph and therefore structured as follows:

■ Chapter 1 introduces the modeling methods in forest inventory and the objectives of this work.

■ Chapter 2 is the state of the art that integrates knowledge in NFI, LiDAR measurements, and computer science.

■ Chapter 3 describes the design of computational virtual measurement (CVM) and a conceptual implementation of CVM, i.e., the virtual ruler, as an example to show how CVM works.

■ Chapter 4 shows the data collection of two formal implementations of CVM, i.e., the virtual water displacement (VWD) method, and the sunlight analysis method.

■ Chapter 5 includes the detailed processes of the VWD method and sunlight analysis method.

- Chapter 6 displays and discussed the results of VWD and sunlight analysis methods.

- Chapter 7 is the conclusion and outlook of this work.

Chapter Two

State of the art

2.1 National forest inventory

2.1.1 Additional reviewing materials from websites

National forest inventory (NFI) is a state-run systematic sampling strategy, which aims to monitor forests nationwide. NFI is regularly undertaken by a state-run agency, e.g., State Administration of Forestry and Grassland, China. Therefore, documents from official NFI authorities' websites (in Tab.2-1) of five countries, i.e., Canada, China, Finland, Germany, and the USA, were reviewed in order to investigate the common concerns, methods, and workflows in NFIs. They function as supplements to research papers. In these five countries, Canada, China, and the USA have significant forest reserves with rich and accessible NFIs datasets. Finland has the oldest NFIs records. Germany has well-developed theories and methods for NFIs. In addition, video logs for sample plot measurements were also included so as to better understand their field measurement procedures.

Table 2-1. Website links for five NFIs authorities (last visited Oct. 2018).

Nation	Websites
Canada	nfi.nfis.org
China	211.167.243.162:8085/8/index.html
Finland	www.metla.fi/ohjelma/vmi/info-en.htm
Germany	bwi.info
USA	fia.fs.fed.us

2.1.2 Scopes and working divisions of NFI

The first NFI was established in Scandinavia in 1920s [34]. In early times, forest information was collected solely from simple plot measurements. Since 1980s, the multi-source data was formally included in NFI workflows in Finland [31]. Correspondingly, the measuring instruments vary from fabric tapes [6] to satellite-based sensors [7,8]. As was reported, NFIs were undertaken in Finland at 11 times with a rolling period of 5 to 10 years till 2013. Similar procedures were also found in other countries. NFIs were taken by 112 countries in the year 2014 and covered 81% of the global forest area [8]. It was reported that well-developed NFI systems had positive impacts on the forests recovering in some countries. Meanwhile, deforestation happened on a global scale [4,9]. The common scopes

of NFI were concluded as the following: (i) evaluation of quantity, quality, structure and distribution of forest resource; (ii) data support to forest policy, forest industries, and nature protection; and (iii) scientific research.

Regarding differences in spatial scale, NFI workflows are divided into two major parts, i.e., sample plot measurements and forest thematic mapping. Sample plot measurements are the kernel and conventional procedure to collect physical parameters of trees for the regular update of forest information. General workflows of sample plot measurement have six aspects (learned from German NFI): systematic sampling design, preparation for field surveys, sample plot measurement, quality control, evaluating data, and the comparability of results [33]. Compared to sample plot measurements, forest thematic mapping is much likely to provide auxiliary information for NFI. For example, some quantitative results (as by-products) of forest thematic mapping are not accepted by the NFI authorities. For instance, the growing stock volume (GSV) is determined using data from sample plot measurement. However, the GSV map from remote sensing methods is for the purpose of visualization in most instances [32].

2.1.3 Sample plot design and measurement

An NFI sample plot has fixed shape and distribution. The shape of sample plots (or subplots) is typically a circle with specific radiuses, except for China (using square sample plots). Meanwhile, the radiuses of sample plots vary between different countries. Even within the same country, for example, the radius can be different, e.g., 12.52 m in south Finland and 12.45 m in north Finland. To be simplified, one set of radiuses was used to represent one country in this study. Thus, the radiuses of sample plots for each country are 11.28 m (Canada), 12.45 m (Finland), 17.95 m (USA), and 25 m (Germany). China uses square sample plots with 25.8 m side length as the dominant shape for NFI sample plots [32].

A cluster is a superior structure that usually contains several sample plots with a certain spatial distribution. It is used to organize a few sample plots (or namely subplots), equaling to a namely integral plot by statistical design in Finland, Germany, and the USA.

For example, a USA cluster has four subplots that represent a literal sample plot. In this cluster, a subplot is in the center with three subplots located 120 feet (36.6 m) from the center point at azimuth angles of 0, 120, and 240 degrees [10,28,29]. Designs of sample plots and clusters of five countries are compared in Fig.2-1.
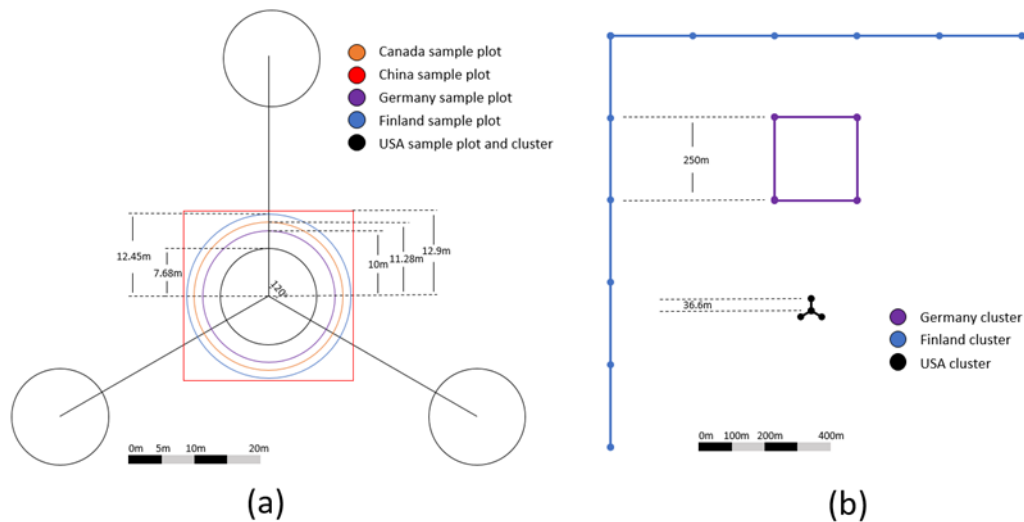
Figure 2-1. Spatial distributions of the NFI sample plots and clusters of five countries; (a) spatial distribution of sample plot and sample plot cluster for USA (black), and spatial distribution of sample plot for other four countries (other colors); (b) spatial distribution of sample plot cluster.

In a sample plot measurement, four kinds of information are usually collected by NFIs field crews, i.e., property (the ownership) information, tree information, undergrowth information, and ancillary attributes. As was shown in the example video made by Johann Heinrich, Thünen Institute, Germany [38], a typical NFI crew field workflow contains the following steps: (i) determining the location of a sample plot; (ii) pinpointing the center of the sample plot; (iii) measurements of DBH using diameter tape, measurements of diameter of the upper part of the tree trunk (optional); (iv) measurement of tree height using angle gauge; (v) collecting dead wood and undergrowth information; (vi) logging tree parameters using a laptop. Figure 2-2 shows the common works of NFI crews in sample plot measurements.
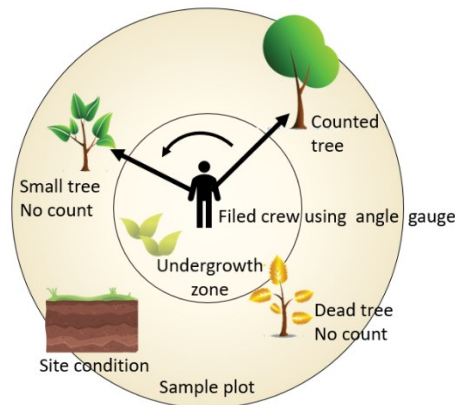
Figure 2-2. Works of NFI crews in sample plot measurements.

With the development of remote sensing methods, Canada uses "photo plot" as the primary source replacing the conventional field sample plot. A photo plot is a square area with 2 km side length. Within this area, biomass, carbon content, and tree volume are collected from aerial photo interpretation along with other remote sensing data sources [39]. The use of photo plot is to reduce human labor with a degrading accuracy. Eventually, tree parameters derived using remote sensing methods have to be validated with conventional sample plot measurements.

2.1.4 Forest thematic mapping

As previously stated (in 2.1.2), sample plot measurements are the primary data source for NFI. Under these circumstances, most forest thematic maps play a role as providing visualization only, e.g., GSV map and forest type map. Those maps are generated using remote sensing methods combined with statistical results from sample plot measurements [18]. Although those maps can produce quantitative results, those quantitative results are not logged in the NFI database.

There is one exception for forest thematic mapping, which is the delineation of forest/nonforest using remote sensing approaches. The forest cover map is the key product of the delineation of forest/nonforest. Besides taking a role in visual display, the quantitative result is logged in NFI databases [40]. The measuring instruments for the forest cover map varied, e.g., optical [41], infrared [42], and radar [43]. The improvement in

accuracy can be achieved by the fusion of multiple data sources [44].

2.2 Measuring forests using LiDAR

2.2.1 LiDAR sensors

LiDAR is a non-contact method that employs pulsed laser for range measurements. The distance between the sensor and the target is derived from the time-of-flight and the speed of light [45]. Generally, there are two different kinds of LiDAR sensors, i.e., discrete return LiDAR and full-waveform LiDAR. A discrete return LiDAR sensor records reflectance as separate returns [46]. A full-waveform LiDAR sensor records reflectance in a continuous waveform, which stores information on energy changes. It is facile to distinguish peaks in a waveform LiDAR return and to convert the full-waveform return to discrete returns [47]. Furthermore, these two types of sensors can be further combined with two scanning modes. A profiling LiDAR always records returns directly below the sensor, and a scanning LiDAR records across a wide swath on one side of the sensor [48].

2.2.2 LiDAR data sources, classified by the visibility of tree structures

It is used to classify LiDAR data sources according to carriers of LiDAR sensors, e.g., spaceborne LiDAR, airborne LiDAR (as well as airborne LiDAR scanning, ALS), terrestrial LiDAR (as well as terrestrial LiDAR scanning, TLS), and vehicle LiDAR (as well as vehicle LiDAR scanning, VLS). In this study, a new classification system for LiDAR data sources was developed specifically for tree measurements. The criterion of classification was based on the increasing visibility of LiDAR sensors against tree structure, and the capability to retrieve tree parameters. The first class of LiDAR data sources was defined as "vertical data source", which means that only information of the tree height can be extracted from these data sources. All spaceborne LiDAR and some airborne LiDAR at middle and high altitudes belong to this class. The second class of LiDAR data sources was defined as "horizontal data source", which means that the positional information along the horizontal direction can be distinguished from these data sources. Some airborne LiDAR at low altitudes belongs to this class. The beam from those LiDAR sensors can penetrate the tree canopy structure and collect enough information on the basal height area.

Consequently, DBH can be determined. The third class of LiDAR data sources was defined as "high-density data source", which means that the sampling quantity in a LiDAR scanning is far exceeding the needs of tree parameter extraction. Meanwhile, most of the tree structures can be recorded at very high resolution. The terrestrial LiDAR and all other similar ground LiDAR data sources belong to this class. The summary of this classification system is shown in Tab 2-2.

Table 2-2. The new classification system for LiDAR data sources according to the visibility of tree structures.

Class	Carries	Attitude	Resolution	Visibility of tree structure	Topic
Vertical	ICESat/GLAS	600 km	50-70m fp[1]	H	Forest AGB and carbon [49]
	ZY-3 02	505 km	50m fp	H	Experimental [50]
	Helicopter / Falcon aircraft	150 m / 400 m	0.45m fp , 4 pcd[2] / 0.25m fp , 20 pcd	H	Canopy height and forest AGB [51]
Horizontal	RiCOPTER	90 m	2965- 5344 pcd	H, DBH	H and DBH measurement [52]
	Droidworx Skyjib Oktokopter	30 m	174 pcd / 5652 pcd	H, DBH	Difference of ALS and SfM [53]
High-density	Leica HDS6100	Ground	25200 pcd	H, DBH, V	Effects on TLS scan position [54]
	Leica HDS6100	Ground	20000-50000 pcd	Modeling	Single tree modeling [55]

[1] fp refers to footprint size (unit:meter); [2] pcd refers to point cloud density (unit:points/square meter); pcd =1 / fp.

2.2.2.1 Vertical data source

Compared to other remote sensing approaches, e.g., optic and radar, LiDAR provides much more accurate information of height. As previously stated (in 2.2.2), if only vertical information can be extracted from the point cloud, this data source is a vertical data source. The resolution of vertical data sources is usually described with the unit "footprint". It is facile to convent footprint into point cloud density (pcd), based on the reciprocal relationship.

There are a few spaceborne LiDAR satellites, which can be used in forest measurements. The Ice, Cloud, and land Elevation Satellite with a Geosciences Laser

Altimeter System (ICESat/GLAS) includes a single beam, near-infrared (1.064 mm), 40 Hz waveform profiler with 50–70 m footprints, and an along-track post-spacing of 172 m [49]. Recently launched satellite, Ziyuan3-02 (ZY3-02), is equipped with an experimental laser altimeter with frequency at 2Hz and 50m footprint size [50,56].

The term "footprint" can be further divided into two groups, i.e., large footprint and small footprint. Large footprint data is usually provided by space-borne LiDAR. Small footprint data is usually provided by ALS at middle and high altitudes. There are four components in an ALS system: a LiDAR sensor to collect ranging and intensity information, a GPS receiver to track the altitude and location, inertial measurement units (IMU) to record flight attitude, and a data recorder [57]. Compared to spaceborne LiDAR satellites, much more researches preferred small footprint ALS for forest inventory, due to the flexibility and the size of footprints [48,51,58].

2.2.2.2 Horizontal data source

Compared to vertical data sources, the key feature of horizontal data sources is that it can provide enough positional information on basal height area. Accordingly, DBH can be measured from these datasets. In order to penetrate the upper structures of trees, an effective way is to decrease the distance between LiDAR sensors and trees. Compared to ALS at middle and high altitudes, near ground (near canopy) ALS can gather enough positional information on the basal area.

A near ground ALS is usually undertaken by drones instead of airplanes. Unmanned aerial vehicle (UAV) and unmanned aircraft systems (UAS) are two terms referring to drones. Literally, UAV is a component in UAS [59]. In most studies, UAV was to refer to a fixed-wing drone at relatively high cruising altitudes at several hundred meters above ground. Meanwhile, UAS was referred to fixed or rotating wing drones, which were controlled by human on the ground nearby [60]. Therefore, to be simplified, UAV was classified into vertical data sources, and UAS was classified into horizontal data sources.

More than LiDAR sensors, the optical camera can also be loaded on a UAS. Structure from Motion (SfM) algorithm is utilized to generate image-based point clouds from optical

photos [61]. If a LiDAR sensor and a camera loaded on the same carrier, the image-based point cloud usually have a higher point density than the LiDAR point cloud. However, image-based point clouds have an inferior performance on the penetration of tree structure [53]. Image-based point clouds can be an alternative method to save the cost of field measurements for forest measurements [21].

2.2.2.3 High-density data source

High-density data source records full positional information of trees, which contains much more information than the requirements of measuring tree height and DBH. Tree structure at the branch and even trig level can be clearly detected from this data source. Compared to other LiDAR scanning methods, TLS produces the densest point cloud. The point cloud density of TLS varies from a few hundred points per square meter to over 25000 points per square meter [54,62]. Phase shift (PS) and time-of-flight (ToF) sensors are the two main working modes of TLS sensors. A PS sensor records only one return for each beam and has very high point quantities with fast acquisition speed. ToF sensor is a full waveform sensor and exhibits slow scanning speed and short ranging distance, compared to PS sensor [63]. The quantity of positional information in a high-density data source is far more than the requirement of the conventional measurement of tree parameters. In a broad vision of virtual geographic environment (VGE) [64], a TLS derived point cloud is positional freeze for every irradiated object in three-dimensional space in an instantaneous moment.

2.2.3 LiDAR data processing algorithms for tree parameters

As previously stated (in 1.2), LiDAR methods are not utilized in the NFI sample plot measurements. It's worth noting that all algorithms summarized in this section were developed under the circumstance of stand-level forest inventory (SFI). SFI is different from the NFI in three aspects: (i) The spatial scale of SFI varies from a few acres to a few square kilometers. On the contrary, NFI sample plots have fixed shape and spatial distribution; (ii) SFI aims to extract tree parameters in a specific forest area. Consequently, the developed method is significant for a specific forest area only. Whereas, NFI uses

unified methods to measure all sample plots nationwide; (iii) SFI usually has a particular threshold for measurement error. While NFI pursues high accurate measurement on sample plots. Thus, it is hard to apply experience from SFI to NFI directly.

2.2.3.1 Tree (stem) distribution

As soon as entering a sample plot, the first step for NFI field crews is to draw a sketch for tree distribution or make confirmation from previous logs. Reviewed studies had no report on a fully precise detection for tree distribution. The detection rates varied from 22% to 97% differed with methods and stem density [65,66]. The common method was to identify individual trees in a horizontal slice from original point clouds around the height of DBH. In this method, an appropriate threshold for fitting circles was significant for a successful detection [65]. Improvements in the algorithm level were helpful for more accurate detection. For example, Chen et al. introduced a new distance-adaptive search radius method. The distance between sensor and object was also employed in supporting vector machine algorithm. The detection rate in this method was 76.1% [67].

Compared to efforts on algorithm developments, improving the quality of point clouds is significantly much more helpful for tree detection. Both multi-single scan and multi scan provide better coverages for a sample plot using multiple scanning positions. The use of reflectors or not showed insignificant for tree detection [68]. Additionally, instead of circle, other shapes, e.g., cylinder, were used to fit subsets of point clouds to detect tree locations [55]. Voxel methods were also reported for tree detection. For example, Heinzel et al. detected tree stems using 3D voxel grids, and the detection rate varied from 84% to 97% [69]. Besides influences from scanning scenarios, stem density and the distance between sensors and objects had great influence on tree detection rate. Meanwhile, the occlusion effect seemed to be unavoidable in the middle and high-density forest [70].

Despite the insufficient in tree detection rates, locations of NFI sample plots also have negative effects to tree detections. Because those locations are determined by systematic sampling designs. Consequently, site conditions exhibit a great variety. Therefore, it is impossible to utilize a standard LiDAR protocol for NFI field crews, which can produce a

theoretical fine point cloud for certain algorithms.

2.2.3.2 DBH and the upper part diameter

DBH is one of the essential tree parameters. Similar to tree detection methods, DBH is determined by circle or cylinder fitting algorithms as well. Technically, measurements of tree location and DBH are processed simultaneously. The choice of scanning scenarios does not have significant affairs on the accuracy of DBH. For example, the accuracy was reported as 1.5 cm in both multi-single scan and multi scan scanning scenarios [65]. While it was reported as 1.3 cm in the single scan [17]. An additional UAS flight could enhance the positional information of the upper parts of trees, which was reported helpful for the measurement of the upper part diameter [71].

Significantly, LiDAR shows its potential as an alternative for conventional measurement methods on DBH and the diameter of the upper parts with minimal error. Due to the scanning mechanism of LiDAR, it can integrate all those independent and manual measuring events by NFIs field crew into one (or few) measuring processes. Consequently, all the measured objects share the same system of error. It would be helpful for data quality control.

2.2.3.3 Tree height

The foremost challenge for the tree height measurement is the visibility of the treetop from a ground-scanning position. This is due to the complex structure of canopy, in which occlusion is unavoidable, especially in leaf-on season. For example, Moskal et al. compared field measurements with single side TLS scannings. In this study, laser range finder, which had the same beaming mechanism as TLS, was applied as the measurement equipment. Results showed that LiDAR metrics only predicted 57.27% of tree height with Root Mean Square Error (RMSE) at 0.75 m [72]. Similar studies showed that the RMSE in tree height varied from 0.8 m to 6.5 m [19,68,70].

Similar to tree detections and DBH measurements, the data quality of the point cloud is also sensitive to the tree height measurement. All of them indicated that the data quality is a vital issue for utilizing LiDAR in a routine NFIs sample plot measurement. For

enhancing the data quality for tree height measurement, a UAS flight, in addition to TLS scannings, is specifically helpful due to the view of angle. Because tree height is extracted using the difference between the height from the crown peak and the corresponding stem ground point [73,74].

2.2.3.4 Volume and biomass

Under normal circumstances, the volume and biomass of trees cannot be measured directly using measuring instruments. The volume and biomass are regressed using allometry methods [75]. Both conventional and LiDAR measurements share the same role, which provides parameters for allometric equations. One major drawback of allometric methods is that they are sensitive to tree species and site conditions [16]. A unified allometry equation (and parameters) for all sample plots over the world was not reported. The precise measurement of volume and biomass can be utilized by analytic methods, which is a destructive and labor cost approach [76]. Therefore, the utilization of the analytic methods is limited in NFI. Their role is to provide ground truth reference for calibration allometry equations.

As previously stated (in 2.2.2.3), LiDAR scanning provides massive positional information in a sample plot. According to this feature, CM methods were developed to extract volume and biomass from point cloud [11,48]. Compared to allometric methods, the advantage of CM methods is that they are independent of tree species and site conditions. In other words, CM methods simulate the mechanism of analytic methods. This advantage shows the potential of CM methods to be an alternative to allometric methods. Raumonen et al. proposed the quantitative structure models (QSM) method in 2013 [25]. This method was a geometric-primitive-based approach using massive cylinders to represent the structure of a tree. From the viewpoint of NFI sample plot measurements, QSM method simulated the process of disassembling a tree to stem disk with volume measurement. However, QSM was a modeling method, which required validations with other ground truth reference. It will introduce additional procedures in the workflows of NFI.

2.2.3.5 Crown width

Crown width is a representative for vital tree parameters, but it is not regularly collected by all NFI authorities. The main reason is no effective process to limit uncertainties from field measurement by field crews. By definition, crown width is the average crown spread. Due to different crown shapes, there are corresponding equations. The simplest equation is the mean value between the longest spread and the shortest spread [77,78]. However, conventional measuring instruments cannot determine where is the longest or shortest point of a tree crown. Recognition of crown edges relies on human visual inspection. Therefore, the recognition of the hight point of a tree exhibits much greater uncertainty. The determination of the highest point of a tree can be simplified into an issue in 2D liner space by human consciousness. On the contrary, the determination of the crown shape remains in 3D space, in which the complexity increases significantly.

Full information on a crown structure can be recorded by LiDAR scanning. This is due to that one of the inspiring features of LiDAR scanning is the unconditional sampling of its target. Thus, a projection of the crown area, instead of crown width, can be extracted from point clouds. The crown area is more advanced than the crown width in one additional dimension. Moreover, similar to the measurement of the tree height, ALS has better performance than that on TLS measurement, attributing to the similar occlusion issue as in tree height measurement [79].

2.2.3.6 Light conditions of single trees

In nature, light is the primary energy source for plant growth. Lots of biological activities for plants directly relies on light conditions, e.g., photosynthesis and transpiration [80,81]. Competition for a better light condition is a common growth strategy for individual trees by extending canopy structures in vertical and horizontal directions [82]. Therefore, the quantitative assessment for light conditions is preferential to study tree biology. However, the light conditions for single trees or sample plots are not collected by NFI due to technical difficulties.

Radiation detection is the dominant method for assessing light conditions in forests

[83-85]. In a forest field, the light intensity is usually recorded by quantum sensors [86]. Photosynthetic photon flux density (PPFD) is the quantitative indicator for light conditions [6]. The measuring for PPFD above canopies is straightforward because shading effects do not exist. This is because clouds do have shading effect also to the top of canopy. On the contrary, the distribution of sensors under canopy has a great influence on the value of PPFD due to uneven tree shades [87]. Moreover, for a single tree in forests, radiation sensors cannot distinguish interference from surrounding objects (adjacent trees). At the meantime, the sensor readings are affected by many environmental variables, e.g., the date, clouds, air humidity, and wind [88].

Including radiation detection, several measuring methods can provide general indications for light conditions of a single tree. Those methods were divided into two groups, direct and indirect. The direct methods provide the natural characteristics of the targets. One kind of measurement is based on crown morphology [89]. The conventional dendrometrical description for crown shapes is facile. Regular shape objects such as cone and semi-spherical ball are used to represent tree crown [90]. Allometric relationships between tree height DBH are used to make tree crown models [91]. Some studies include crown width in the modeling process [92,93]. With the development of LiDAR, high precise estimations for crown shapes are available [11,94]. Canopy gaps are also a significant indicator of light conditions [95,96]. However, its scope is usually for multiple trees in the forest. Different from the methods for crown (canopy) measurement, the leaf area index (LAI) is recognized to be better for single tree analysis. LAI is the total one-sided area of leaf tissue per unit ground surface area [97]. LAI is an allometric method, which connects the area with the capability of photosynthesis for leaves. Meanwhile, LAI is characterized as a systematic sampling method [98].

Besides the direct measurements, indirect methods can be used to evaluate light conditions by measuring the metabolites of trees [99]. At the leaf level, canopy photosynthesis and transpiration measurement system (CAPTS) is utilized to measure and describe the intensity of photosynthesis using CO_2 uptake rates indirectly [100]. However, it is a labor-intensive work for a single tree [101].

2.3 Virtual geographic environment and physical simulation

2.3.1 General information

This study aimed to measure data using physical simulation instead of conventional modeling methods. As a pilot study, there was no previous reference of extracting tree parameters using physical simulation. Therefore, experiences from other study fields were reviewed. Some of them even had no direct relationship with forest science. However, the general methodologies of these studies were worth to be investigated.

2.3.2 Virtual geographic environment

2.3.2.1 Concept development of virtual geographic environment

"Virtual geography" was firstly introduced by Batty et al. in the 1990s [102]. In 2001, Lin et al. extended this concept as "Virtual Geographic Environments" (VGE) [103]. In an ideal VGE, all the components in the realistic environment, e.g., water, air, soil, plantation, and human beings, have corresponding electrical forms. Furthermore, all those components keep continuously changing as a dynamic system. As was demonstrated by Lin et al., the VGE system helps the researchers to "feel the geographic scenarios in person" and to "know the geographic laws beyond reality" [104,105]. In the early stage, the concept of VGE was limited to the visual simulation of natural environments and had no cases in quantitative studies.

With the continuing enhancement of computer performance, scientists could employ quantitative simulation in VGEs starting from the 2010s. For example, Mekni et al. simulated human behavior in VGEs in 2010 [106]. Liang et al. applied physically based methods to visualize the dynamics of shallow water in 2015 [107]. Up to date (Oct. 2019), there is no case on VGEs applied in forest science. Therefore, in order to learn the development experience of VGEs, cases in other fields were investigated in the following section.

2.3.2.2 Primary mechanism of VGE

In this study, the primary mechanism of VGE was concluded as the following:

Applying dynamic processes on static objects and waiting to see what happens next.

2.3.2.3 Study cases using VGE

VGE acts as a more conceptual method than a specific method. Compared to image analysis using ENVI, spatial analysis using QGIS, there are no specific applications for VGE studies. Therefore, various technologies have been utilized in the development of specific VGEs.

Based on web services, Zhang et al. (2007) developed a distributed VGE (DVGE) system. The approach developed in their work aimed to integrate available GIS tools with the concept of VGE together. Two third-party applications were implemented in DVGE, which were open geodata interoperation specification (OpenGIS) and geography markup languages (GML). Finally, a simulation of water pollution in Yangzhou, China was applied in DVGE. Aimed to integrate multiple data sources and simulation methods, Xu et al. (2011) proposed the concept of collaborative VGE (CVGE) [108]. There were two key works in this study. The first work was to develop the concept and system framework of CVGE. The second work was to implement CVGE for air pollution simulations of the Pearl River Delta. Compared to conventional methods in the air pollutions analysis, CVGE provided the function of geo-visualization.

Chen et al. (2013) developed virtual social environment (VSE) [109]. The aim of VSE was to enhance the users' experience by providing feelings of real scenarios in VGE. There were four elements in VSE: (i) real geographic data associated with time dimension; (ii) dynamic simulation of natural phenomena and processes; (iii) virtual shared spaces for enhancing participants' interaction; (iv) shared hot spots for investigating social phenomena from user behaviors. In the same year, Song et al. (2013) simulated how to evacuate crowds out of the subway station [110]. Realistic modeling of the subway station was vital of importance in this study. A similar study was reported by Lv et al. (2015) with the simulation of traffic passenger flow in a much larger geospatial scale [111].

In geographic fields, LÜ (2011) proposed the framework, structures, and functions for geographic analysis-oriented VGE [112]. Four sub-functions of VGEs were introduced, i.e.,

virtual environments for data, modeling, expression, and collaboration. The conclusion was that further development of VGE would be taken to provide convenient simulations and better virtual scenes. Lin et al. (2013) regarded VGE as the next generation of geographic analysis tools after the ten-year development of VGE [105]. Compared to conventional visualization methods, VGEs had three diffident features: (i) More than visualization, VGE was capable of geographic analysis; (ii) Each VGE had a specific task, which was not a general platform; (iii) VGE was an extension beyond geospatial web (GeoWeb) [113]. In another case, Zhu et al. (2014) simulated a scene of the dam-break flood [114]. Compared to cellular automata (CA) methods, advantages of VGE appeared in intuitive, efficient, and interactive visualization to users. OpenSceneGraph [115] and osgEarth [116] were two visualization tools in this research. However, the simulation of the flood was still applied with a combination of conventional methods. VGE played a role in integrating conventional methods.

Recently, Liang et al. (2015) applied physically-based methods to visualize the dynamics of shallow water [107]. It was the only case that applied physical simulation in VGE. Compared to other VGE studies, it introduced the physical calculation for refraction. Whereas in all other contemporaneous studies, geographic information was regarded as virtual lands only [117-119]. The significance of this study was to illustrate the feasibility of the qualitative simulation of natural phenomena.

To sum up, the current VGE studies focus on three research directions: development of computer platform (computer science), simulation of human behaviors (social science), and enhancing geographic analysis (geographic science).

2.3.3 Physical simulation

2.3.3.1 Physical simulation at desktop computers

Physical simulation has a wide range of applications, e.g., atomic-level simulation for thermal conductivity (physics) [120], physics-based hydrologic-response (hydrology) [121], and earthquake simulation (geology) [122]. Those studies required high-performance computing clusters, which are significantly different from the computers used

in daily life. Unlike these methods, in this thesis, the physical simulation refers explicitly to the physical simulation driven by physics engines at desktop computers. The range of this simulation is usually in classical Newtonian mechanics [123]. However, limited by the performance of the desktop computer, the precision of simulation could not compare with professional simulations using high-performance computing clusters. Meanwhile, as an end-user of physics engines, it is usually not capable of revising algorithms in physics engines. Moreover, it is not intended to know the complicated internal workflow of physics engines.

2.3.3.2 Physics engines

Serval physics engines were developed to provide solutions to physical simulations at desktop computers. There are two types of physics engines. The first type is scientific engines, which are highly professional engines, e.g., computational fluid dynamics engine [124]. It is usually hard to apply a scientific engine in another field of study. Meanwhile, a scientific engine is usually cannot be supported by desktop computers. The second type is game engines. Compared to high-precision scientific engines, game engines process real-time physical simulation on desktop computers with relatively low precision [125]. Game engines are a bundle of math equations based on classical Newtonian mechanics and computer graphics. Various simulations of physical phenomena are supported by the same engine. Fig.2-3 shows how a game engine calculates physical processes for the collision of two objects [126]. Afterward, secondary software developers can utilize physical simulations by calling the interfaces of these physics engines [127].
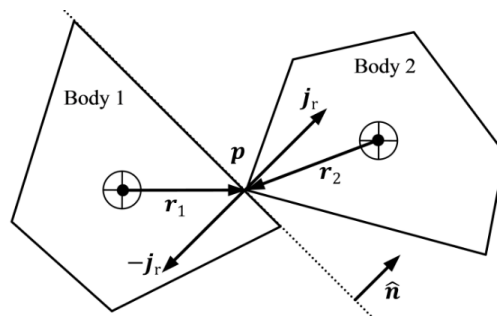
Figure 2-3. The calculation for a collision of two rigid bodies [128]. The calculation is enclosed within physics engines without the need for users to know the exact mechanism.

Adrian et al. (2007) investigated the simulation accuracy of game physics engines [129]. Five features in each physics engine were tested and evaluated, i.e., integrator performance, material properties, constraint stability, collision system, and stacking. The results indicated that there was no single physics engine obtained the best scores in all tests. Erez et al. (2015) performed a similar study in comparison to different physics engines [130]. It concluded that PhysX and Havok had the best performance on physical accuracy. Both of them are the most popular physics engines in the current commercial market.

2.3.3.3 Study cases using PhysX

NVIDIA PhysX software development kit (SDK) is a physical simulation solution for multi-platform [127]. Unity is an integrated development environment (IDE) to support the development of 2D and 3D games by integrating multiple functions, including the PhysX engine [131]. An application of physical simulation can be simply developed using Unity on desktop computers. Compared to previously stated VGE studies (section 2.3.2.3), there were very few studies using PhysX (not in computer and information sciences).

Maciel et al. (2009) proposed solutions for simulating the real-time tissue response and force feedback in surgery [132]. Basic objects in PhysX SDK were used to simulate different human tissues. Rigid bodies were used to represent surgical instruments, e.g., scalpel and needle. Cloth was used to simulate membranous tissues. Fluids were used to simulate human blood. Soft bodies had similar physical characteristics of organs when touched by rigid bodies. A similar application of using PhysX to simulate human tissue was also reported by Lu [133].

In aircraft manufacturing, Wang et al. (2012) simulated the assembly procedure using PhysX. Motion simulation and collision analysis were two key steps in this study [134]. A similar study was reported by Martínez-Franco (2018), which was to solve the container loading problem using physics simulation [135].

2.4 Drawbacks of existing forest field measuring methods and potential directions for future improvements

As stated in 1.2, the disadvantages of existing forest field measuring methods are not in the accuracy of data processing, but in the effective domains of their models. Looking through cases listed in 2.2.3, there was no doubt that highly accurate results could be achieved under certain conditions. However, their achievements were bond to specific forest sites and specific modeling parameters. It is well known that the growth of a tree is affected by numerous factors, e.g., soil, water, irradiation, competition, microorganism, even animals [136-138]. Accordingly, the growth of a tree has great specificities to each others. Consequently, a developed model cannot be usually applied to another forest site, no matter how accurate it is. For example, people have to make massive allometric equations of stem volume for different forest sites on a global scale. Those repeated developments of allometric equations magnify the overall workloads. Meanwhile, there is also a problem at single tree scale, which is the simple consistency in the form of mathematical equations was unable to be achieved [16]. In NFI, it is common for a tree species, which has different forms of mathematical equations for stem volume estimation. Under this situation, a question arises that why is a linear regression better than (or equivalent to) an exponential regression? Except for using mathematical indicators, it cannot find an appropriate answer related to the natural features of trees.

In fact, a ready-made method shows the path of how processes data in a natural way. It is the physical scenario in conventional measuring instruments. For example, DBH is measured using a diameter tape. The physical scenario of this measuring process was concluded as the following: (i) the initial movement of diameter tape (start to surround trees); (ii) the dynamic change (shrinking) of the spatial distribution of diameter tape; (iii) the physical contact between tree stem and diameter tape. In this process, actually, two measuring instruments are involved. The first instrument is the diameter tape that response to provide the reading of length. Meanwhile, physical behaviors of diameter tape are also important, e.g., no elastic deformation, no penetration by trees. The second instrument is the human recognition. It is used to recognize measuring targets, to drive the movement of diameter tape, to evaluate the termination condition. Usually, the raw reading from

diameter tape is regarded as the true value of DBH [12]. That is because, under normal circumstances, no additional measurement using other instruments is employed to validate the DBH measured by diameter tape. The reason is that the physical scenario of diameter tape comes closest to fitting the definition of DBH than all other measuring methods [139].

The advantage of conventional measuring instruments is obvious. For the same tree parameters, e.g., DBH, in forests, the essential difference between direct measurements and modeling methods is the need for prior knowledge. For a measurement using diameter tapes, it is no need to know what the shape of the main stem of trees is. Meanwhile, a modeling method, e.g., circle fitting algorithm, has to use a preset assumption, i.e., the basal area is round. This assumption causes geometric loss even before the data processing begins.

Is it possible to reproduce this physical scenario using computer approaches? The answer would be yes. Firstly, the development of VGE provides theoretical support to the assumption of measuring trees in virtual space. According to VGE, trees are geographic entities with no doubt. Secondly, well-developed physics engines are expected to reduce the development difficulties of computer programs. With the help of those tools, the feasibility of virtually measuring trees by simulating the physical mechanism of real measuring instruments is ballooning.

Chapter Three

COMPUTATIONAL VIRTUAL MEASUREMENT

3.1 Method description

Computational virtual measurement (CVM) is a virtual measuring method in computational virtual spaces. The primary mechanism of CVM is described as the following:

To measure the data in a virtual space by simulating the physical mechanism of measuring instruments and natural phenomena in reality.

The key feature of CVM is that no apparent mathematical processes are included in a CVM process. All the mathematical processes are enclosed in the physic engines as a Blackbox to users. In a virtual space, the target tree parameter is waiting to be measured by the virtual measuring instrument. As a measuring process, no predictions can be made by algorithms. Consequently, no calibration or validation procedures are required, at least in the virtual space.

According to this description, the first step of a CVM procedure is changing the role of the data. In conventional data processing methods, the data act as an information pool. Algorithms use their intrinsic logics to filter, evaluate each element in datasets, and make final predictions as the output. This procedure leads to a question that can we trust the decision of algorithms? In order to get an answer, validation and calibration are necessary works during the development of algorithms. Compared to conventional data processing methods, CVM regards the data as an integrated and undecomposed object. In a virtual space, data act as solid object and is waiting to be measured, not to be processed. For forest studies, the solid object is usually a virtual tree that refers to a corresponding tree in reality.

The second step of a CVM procedure is to simulate the physics mechanism of real measuring instruments and natural phenomena. This simulation can be conceptually regarded as the development of virtual measuring instruments. The physics mechanism of a virtual measuring instrument is usually provided by third-party applications, e.g., PhysX and Unity [140,141]. A virtual measuring instrument usually consists of not only the simulation for one physical behavior but also many physical processes. For example, four physical procedures were simulated in order to investigate light conditions for single trees

in this study, i.e., the motion of the sun, the emission of sunlight, the shading effect, and the radiation sensor.

Figure 3-1 shows the general workflow of a CVM procedure. This workflow is divided into two continuous measurements in different realities. The first reality is the measurement in the real world. The task of this measurement is to record tree information, e.g., tree structures, using a digital form. Then this digital form of trees can be processed in a computer system. For example, a LiDAR scanning has the capability to record tree structures in high detail, which creates a digital form of trees using point clouds. The second reality is the virtual measurement in a virtual space. In this stage, the role of data, e.g., point clouds, changes at the beginning of physical simulations. After the imports, the data wait to be detected in a virtual space. A virtual measuring instrument will begin to measure the data, e.g., the simulation of a ruler for measuring DBH, which shows in the following section.
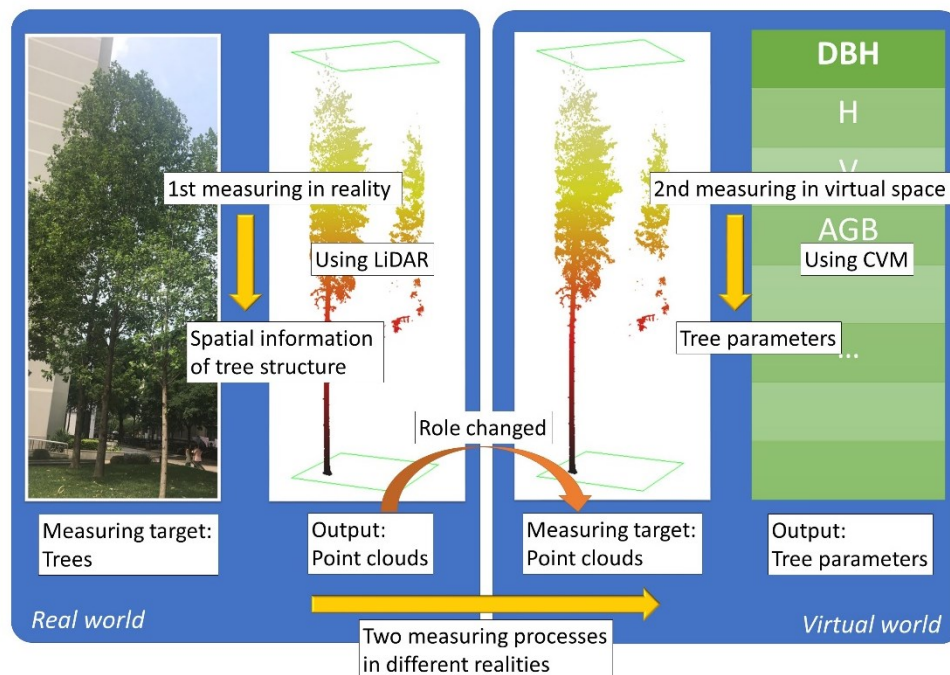
Figure 3-1. The workflow of a CVM procedure for the extraction of tree parameters using two times of measurements, once in reality, and the other in a virtual space (photograph taken by Prof. Baitian Wang in Beijing Forestry University).

3.2 Virtual ruler, a conceptual implementation of CVM

3.2.1 Aims of the conceptual implementation of virtual ruler

CVM is a general and systematic concept, which is not bonded to a specific study topic. A conceptual implementation of CVM was the primary step to verify all the supposes in CVM. Then the CVM would be eligible to be formally implemented with specific studies, i.e., measuring stem volume and light conditions for single trees. This conceptual implementation of CVM was the virtual development of a virtual ruler. The virtual ruler aimed to measure DBH from point clouds instead of the basal area modeling using circle fitting algorithms.

3.2.2 The semi-empirical data processing

The primary aim of this section (3.2) was to demonstrate how to implement CVM with a specific tree parameter and highlight the logical difference between CVM and conventional modeling methods. The conventional data comparison was unable to highlight this difference. Therefore, we developed and utilized the semi-empirical data processing method. This semi-empirical processing was significantly different from the conventional data processing. Generally, conventional data processing methods are suitable for computer processing. However, much of the mathematical processes in computer processing, e.g., spatial filtering [142], are not eligible for manual calculations. Therefore, semi-empirical processing abstracted logic in key steps in computer processing. After then, potential outputs in key steps were simulated by human recognition with the help of computational measuring tools.

Technically, this semi-empirical processing consisted of two steps, i.e., conceptual processing and computational processing. The first step was to simulate the decision procedure of algorithms conceptually. I simulated the decisions conceptually and output a general result, e.g., the position and spatial distribution of a virtual ruler. The second step was to measure the conceptual output using computational measuring tools, e.g., the exact perimeter (length) of the virtual ruler. Subsequently, the conceptual outputs would be

granted with a conventional physical quantity, i.e., area and length, that was facile to compare with each other.

The reason for applying this semi-empirical processing was that the actual data processing was unable to distinguish the difference between static modeling methods and dynamic physical simulations. The significant difference between those two methodologies was discovered at the intern mechanism. In other words, what we compared was the logic of the algorithms, which was not final results. Therefore, the role of data was only a necessary element in formulating the workflow of studies. The results were not the indicator for the comparison of method logic.

3.2.3 Artificial stem disk, point cloud, and key points

As shown in Fig.3-2, an artificial stem disk was created on a 2D plat (2D virtual space) using the paint tool in Windows 10 (Microsoft, State of Washington, USA). This artificial stem disk was a digital representative for a stem disk at DBH height (usually 1.3 m above ground). There were three parts in this artificial stem disk. The main part was a red circle, shown in Fig.3-2(a), which represented a regular-shaped stem disk. It is well-known that any tree stems cannot have regular geometry bodies naturally. Therefore, two convex triangles were added on the left and right side of the red circle to represent irregularity. In Fig.3-2(b), those two triangles were marked in green and yellow. The perimeters of artificial stem disk were determined using ImageJ (National Institutes of Health, Maryland, USA). After then, the DBH of this artificial stem could be determined using the following Eq.3-1. Due to the simple linear relationship between DBH and perimeter, the perimeter was preferred as the indicator for the method comparing between virtual ruler and circle fitting methods in the following sections.

$$DBH = \frac{Perimeter}{\pi} \tag{3-1}$$
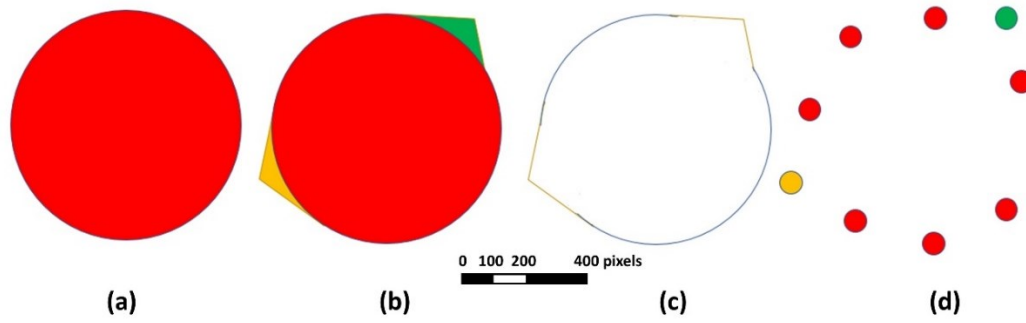
Figure 3-2. Artificial stem disk and point cloud; (a) circle shape stem; (b) circle shape stem adding two convex triangles; (c) high-density point cloud of the stem disk; (d) resampled sparse point cloud with nine key points.

After the creation of the artificial stem disk, a virtual LiDAR scanning was applied to target the artificial stem disk. This virtual scanning produced a point cloud, which recorded the positional information of the outliner of the artificial stem disk. As shown in Fig.3-2(c), if the point density of this point cloud was high enough, this point cloud would look like a continuous line. However, not all points in this point cloud shared the same weight when processed by cycler fitting algorithms. Therefore, some key points were extracted from the raw point cloud, as shown in Fig.3-2(d). Algorithms had to make decisions to include key points in the modeling process, or not. Consequently, the final result was affected by different decisions by algorithms.

3.2.4 Establishing a virtual space

Establishing a virtual space was the next step for the developing *virtual ruler*. Virtual space is the container of physical simulation. A virtual space is usually a 2D or 3D Euclidean space. In this chapter, a 2D Euclidean was suitable for the simulation of diameter tapes because no 3D information was required. This Euclidean space could be supported by third-party applications, e.g., Unity (Unity Technologies, San Francisco, USA), which provided fundamental infrastructures for virtual spaces with easy approaches [131]. As a conceptual development of virtual ruler, there was no need to apply Unity in this chapter. Figure 3-3 shows the establishing of the virtual space with two steps.

(a)   (b)
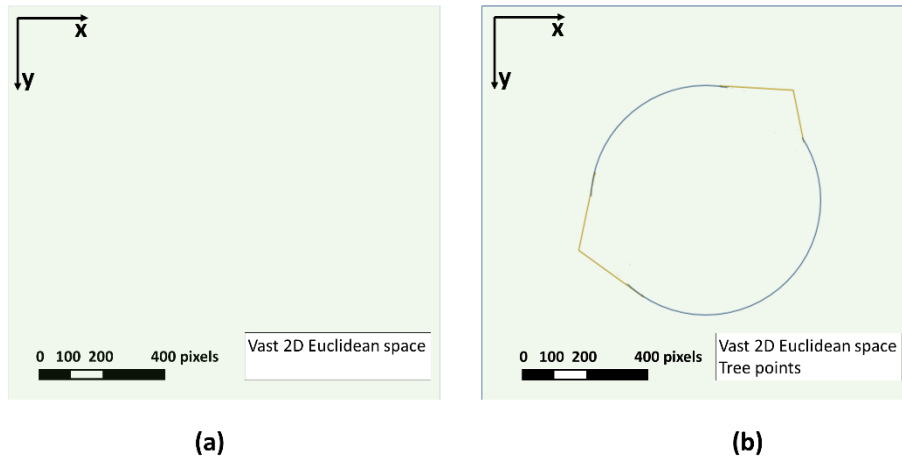
Figure 3-3. The establishment of virtual space; (a) creating a vast 2D Euclidean space; (b) importing the artificial point cloud into this space.

3.2.5 Designing a physical simulation scenario

For a CVM implementation, the essential work was to design an appropriate physical simulation scenario. This procedure was apparently different from common works in modeling methods, which were utilized to find a mathematical relationship between measured quantities and tree parameters. On the contrary, the measured quantities in a CVM implementation were the tree parameters. Consequently, there was no mathematical relationship between measured quantities and tree parameters. Moreover, it could be expected that some physical simulation scenarios in virtual space were unable to be reproduced in reality.

Specifically, for the virtual ruler, the primary physical principle was that the ruler could not penetrate any points in the virtual space. The impenetrability could be provided by physical simulation engines using the simulations of rigid body and collision. Figure 3-4 shows the assumed physical behaviors of a virtual ruler when collides with points in virtual space. According to the assumed functions of virtual ruler, a virtual ruler could not move into the intern area of points. In other words, the inner area was an exclusive area for external detection methods in virtual space.
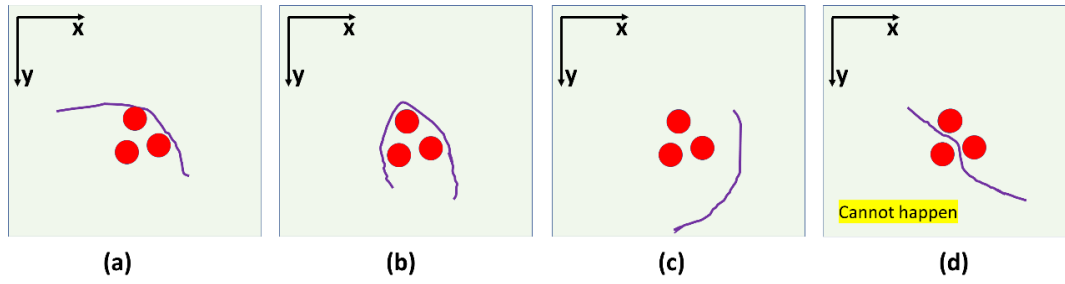
Figure 3-4. The assumed reactions of the collision of the virtual ruler with points; (a-c) assumed different reactions of the virtual ruler when collides with points; (d) the reaction which cannot happen.

The physical simulation scenario of virtual ruler is shown in Fig.3-5. The simulation of virtual ruler began at the creation of a ruler (time 0, t0). At this moment, the ruler lay in the rare area of the virtual space. As shown in Fig.3-5(a), the initial shape of the ruler was not limited. Sooner after t0, the perimeter of the virtual ruler began to shrink continuously. Figure.3-5(b) shows an instantly status (t1) of the virtual ruler. t1 referred to a time point that after the time point t0. With the elapse of simulation time, Fig.3-5(c) shows an instantly status (t2) of the virtual ruler, when it contacts a point (object) for the first time. This collision was a flag event that indicted not only the virtual ruler, but also the points was active (as objects) in the simulation scenario. Meanwhile, the primary physical principle of virtual ruler, i.e., impenetrability, was also evoked to prevent a wrong simulation (Fig.3-4d). With the further elapse of simulation time, an instantly status (t3) of the virtual ruler was close to the true value in Fig.3-5 (d). When the virtual ruler could not shrink any further, the perimeter of this point cloud would be measured as close as the true value.
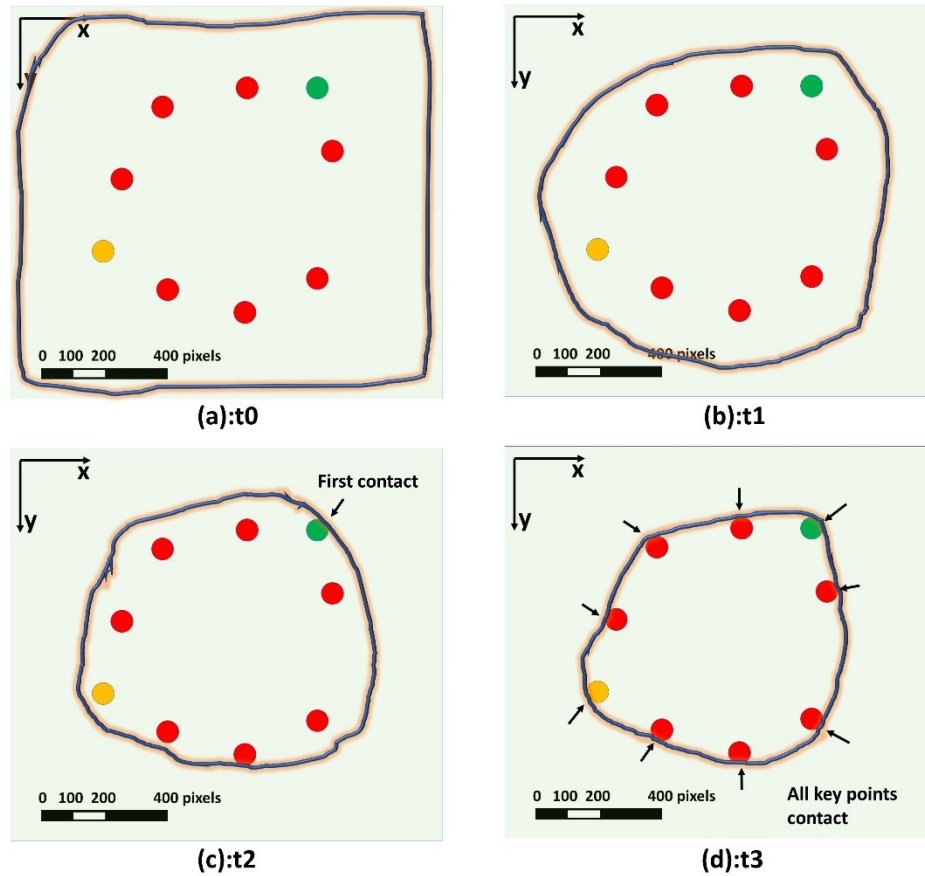
Figure 3-5. The demonstration of the physical behavior of the virtual ruler; (a) the simulation begins at the moment of t0; (b) an instantly status (t1) of the virtual ruler at the moment of t1; (c) the virtual ruler contacts a point firstly at the moment of t2; (d) with enough elapse of simulation time, all (key) points can be contacted with the virtual ruler (t3).

3.2.6 Modeling methods, the circle fitting

In order to make a clear comparison between CVM method and modeling method, the artificial point cloud was conceptually processed using the circle fitting algorithm. The circle fitting algorithm was preferred in many studies for the determination of basal area [17,143,144]. Despite the difference in algorithm details, the circle fitting algorithms had the same mechanism. There were two steps: (i) abstracting key points from whole point clouds, as shown in Fig.3-2(d); (ii) decision making for whether a certain key point should be included in the predicted circle. The problem was that there was no internal mechanism to ensure if the decisions made by algorithms was correct or not. Theoretically, each model of basal area was required to be validated. As previously stated (in 1.2), this additional

validation process prolonged the overall workflow. Figure.3-6 shows different schemes made by the circle fitting algorithm.

(a):m1

(b):m2

(a):m3

(b):m4
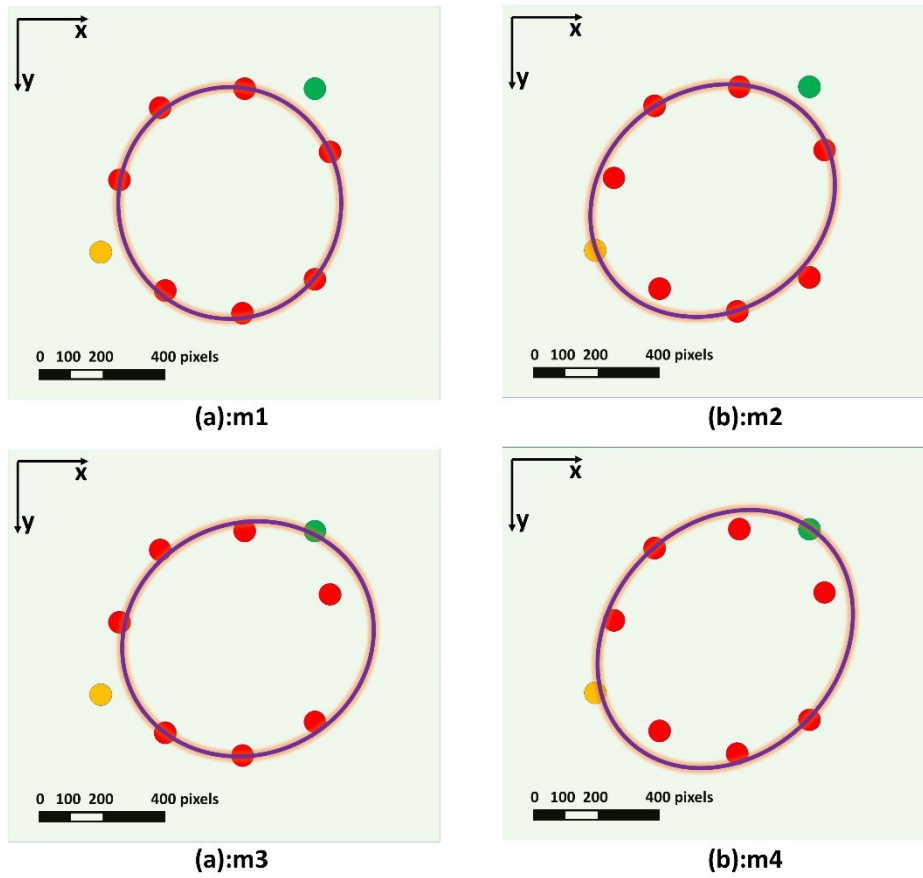
Figure 3-6. A demonstration of different decisions made by circle fitting algorithms; (a) both yellow and green points are not recognized significantly for fitting; (b) yellow point is recognized significantly for fitting, but not for green point; (c) green point is recognized significantly for fitting, but not for yellow point; (d) both yellow and green points are recognized significantly for fitting.

3.2.7 Results

Figure.3-7 shows the comparison of the output between the virtual ruler (in Fig.3-5) and circle fitting methods (in Fig.3-6, four decisions). The perimeters of each step for virtual ruler and schemes in circle fitting methods were measured using ImageJ on Fig.3-5 and Fig.3-6 on the original scale.
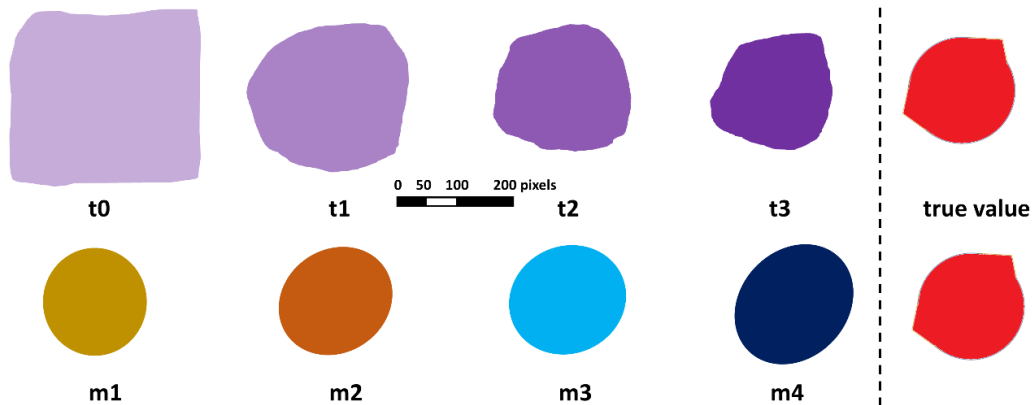
Figure 3-7. Measurement results using virtual ruler (steps from t0 to t3) and Modeling results of the circle fitting method (m1 to m4 referred to corresponding decisions in Fig.3-6).

The comparison of absolute values was unimportant at all. The key difference of two methodologies, i.e., physical simulation and modeling, was the independence of those two methodologies. As shown in Fig.3-8(a), the CVM method has the ability to approach the true value with the elapse of simulation time. Therefore, with appropriate settings of the physical simulation scenario, the output of CVM methods will be close to the true value. The convergence can be used as a mathematical indicator to evaluate a specific CVM procedure.

On the contrary, the modeling methods were not independent methods. As shown in Fig.3-8(b), it was not possible to know the accuracy of a modeling result without knowing the true values. That was where the problems are. The determination of true values required additional steps and workloads. As previously stated (in 2.1.2), the scope of NFI was the collection of forest information. The prolonged chain of validation by the new method made it hard to be applied by NFI authorities. In this case, the CVM was beneficial for NFI, i.e., importing no additional workflow.
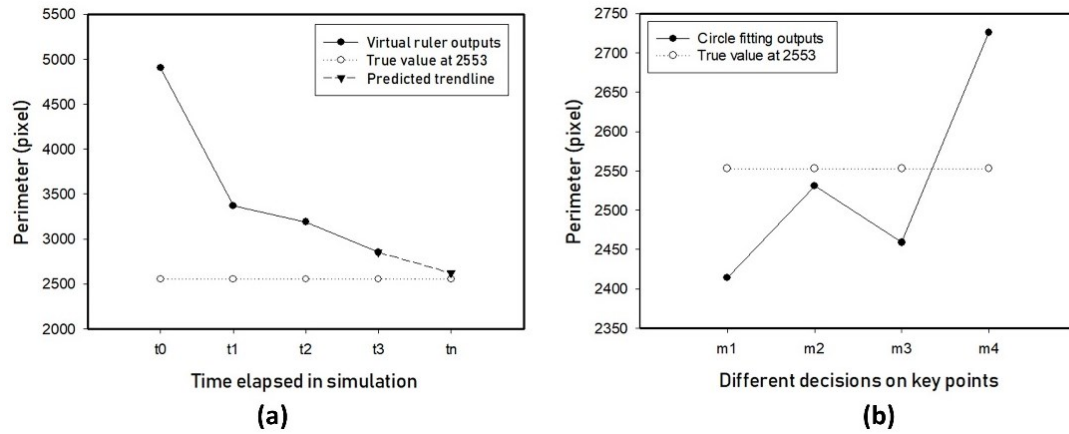
Figure 3-8. The comparison of the features of virtual ruler (a) and circle fitting method (b); (a) the output of f virtual ruler was approaching the true value; (b) couldn't evaluate the accuracy of modeling methods without the knowledge about the true value.

3.3 Development stages of two formal implementations

CVM was developed as a conceptual method in this chapter and was demonstrated using a conceptual implementation, i.e., the virtual ruler in the previous section (section 3.2). The following chapters in this thesis presented two formal implementations of CVM, i.e., virtual water displacement (VWD) method and sunlight analysis method, which were the main parts of this study.

VWD was the simulation of water displacement method in virtual space. VWD simulated the physical behavior of water molecules. The stem volume was determined by the displaced quantity of virtual water molecules (VWMs). This implementation had two stages of development. The first stage was using massive VMMs to measure LiDAR point clouds. In this stage, due to the restriction of computer performance, empirical equations had to be employed. The second stage aimed to eliminate the empirical processes in the first stage and optimizes the simulation of water displacement. In the second stage of VWD, the quantity of VWMs diminished from a few thousand to a few.

Sunlight analysis was the second implementation of CVM, which aimed to investigate the distribution of solar energy on a single tree. Compared to the development of VWD

method at low-level development, the simulation of solar illumination was fulfilled by well-developed software in architecture, which simplified the difficulty of development significantly. There were also two stages of development. The first stage was to analyze light conditions of single tree in stand-alone condition. The second stage analyzed interferences from surrounding trees. Figure.3-9 shows the development stages both of CVM itself and two implementations.
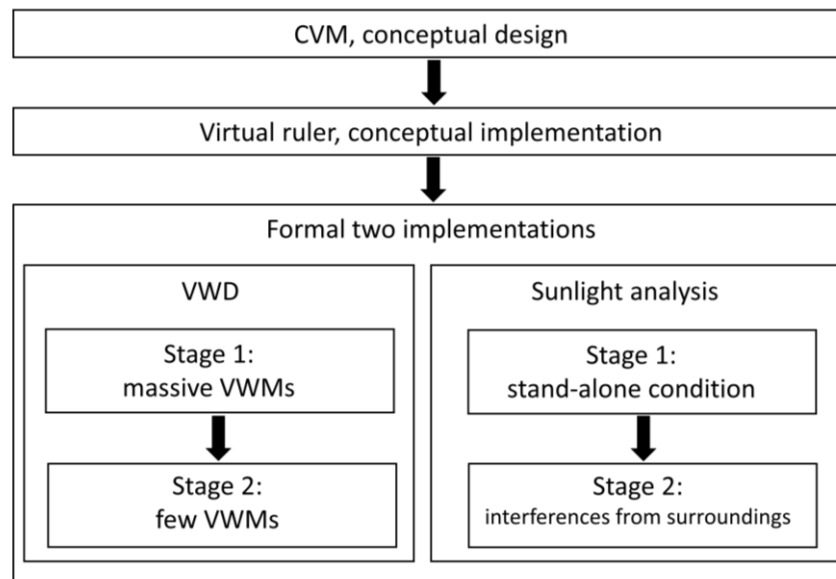
Figure 3-9. Development stages of CVM and two implementations of CVM.

3.4 Conclusion of CVM method

CVM was developed as a general methodology in this chapter. Actually, the extent of CVM was not limited to measuring trees. Tree specific CVM can be also called using virtual measurement for trees (VMT) in order to highlight the measuring target. As an abstract concept, CVM had to be connected with a specific tree parameter. This process was so-called the implementation of CVM. As an introduction to how to implement a CVM method, the development of virtual ruler was showed. The key issue related to a successful implementation of CVM was an appropriate design of physical scenarios. Different from conventional modeling studies, the role of true data declined in importance. That was because, the tree parameter was derived from the physical status of virtual measuring

instruments, which was not from mathematical predictions. It indicated that the conventional calibration process was no use in CVM.

Compared to real point clouds collected from forests, the artificial point clouds were better to introduce processing logic of virtual ruler and CVM. Accordingly, the semi-empirical data processing approach was developed. Meanwhile, it was facile for method compassion between physical simulations and modeling methods at the algorithm logic. This chapter acted as a theoretical preparation of CVM. In the followed two formal implementations of CVM, this conceptual implementation of CVM would be omitted, and conventional computational processing approaches would be employed directly.

Chapter Four

Data Collection

4.1 Artificial objects and stems for the VWD methods

4.1.1 General information

As previously stated (in 3.3), there were two stages of the VWD methods. Both of two stages shared the same data source, which was artificial objects and stems serving as artificial ground truths. Artificial ground truths were created by algorithms or 3D model tools. Each of them had a determined value in the standard unit system in Unity. This unit system didn't have a specific fundamental unit, e.g., meter. In the development of VWD methods, one standard unit in Unity conceptually corresponded to one centimeter in reality. There were two types of artificial ground truths: (i) regular shaped objects were used to support algorithm development of VWD; (ii) artificial stems were representatives of real trees.

4.1.2 Regular shaped objects

Three basic 3D models were created using model tools in Unity [145]. They were a sphere, a cube, and a cylinder. Each of them had a coordinate, a scale parameter, and a surface mesh in virtual space supported Unity Scene [146]. The coordinate and scale parameter were designated variables by user input. The mesh was a collection of vertices and triangles, which was used to organize and display 3D models. Firstly, Unity assigned a pre-build mesh to the determined position. Then, the appropriate size was granted to this mesh. Finally, an object existed in the virtual space and was visible to the user. As shown in Fig.4-1, a sphere mesh has 515 vertices and 768 triangles. A cube mesh has 24 vertices and 12 triangles. A cylinder mesh has 88 vertices and 80 triangles.
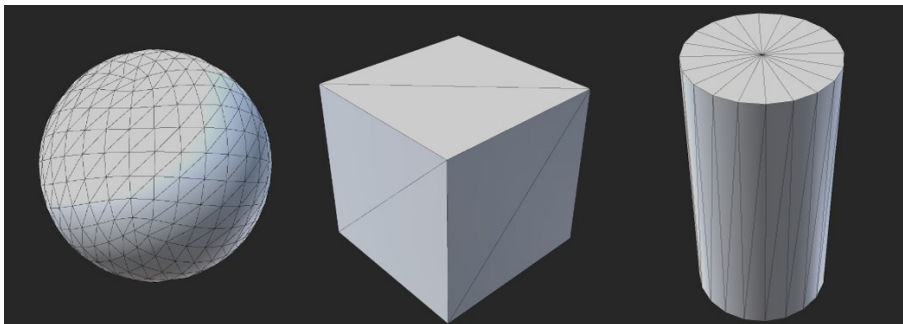
Figure 4-1. Pre-built meshes for the sphere, cube, and cylinder in Unity.

According to the structures of the meshes, the volumes of sphere and cylinder differed from their theoretical values. A method using a normalized vector was applied to calculate the volume of the meshes [147]. As shown in Tab.4-1, there was approximately 2% of the difference between the theoretical volumes and mesh volumes for sphere and cylinder.

Table 4-1. Difference between theoretical volume and mesh volume for Unity sphere, cylinder, and cube meshes.

Model	Equation	Parameters	Theoretical Volume	Mesh Volume	Difference	Calibration Coefficient
Sphere	$V = \dfrac{3}{4}\pi r^3$	r=10	4188.79	4098.68	90.11	97.85%
Cylinder	$V = \pi r^2 h$	r=10 h=40	12566.37	12360.69	206.68	98.36%
Cube	$V = r^3$	r=20	8000	7999.99	0.01	none

Once the volumes were determined, the next step was to convert 3D models to point clouds. Two methods were used in this process. For the sphere, its vertices could be used directly as the corresponding point cloud. The cube and cylinder had fewer vertices and were not enough to be used directly as point clouds. Therefore, an additional process (in 4.1.3) was applied to re-sample them into point clouds. Fig.4-2 shows point clouds for regular shaped objects.
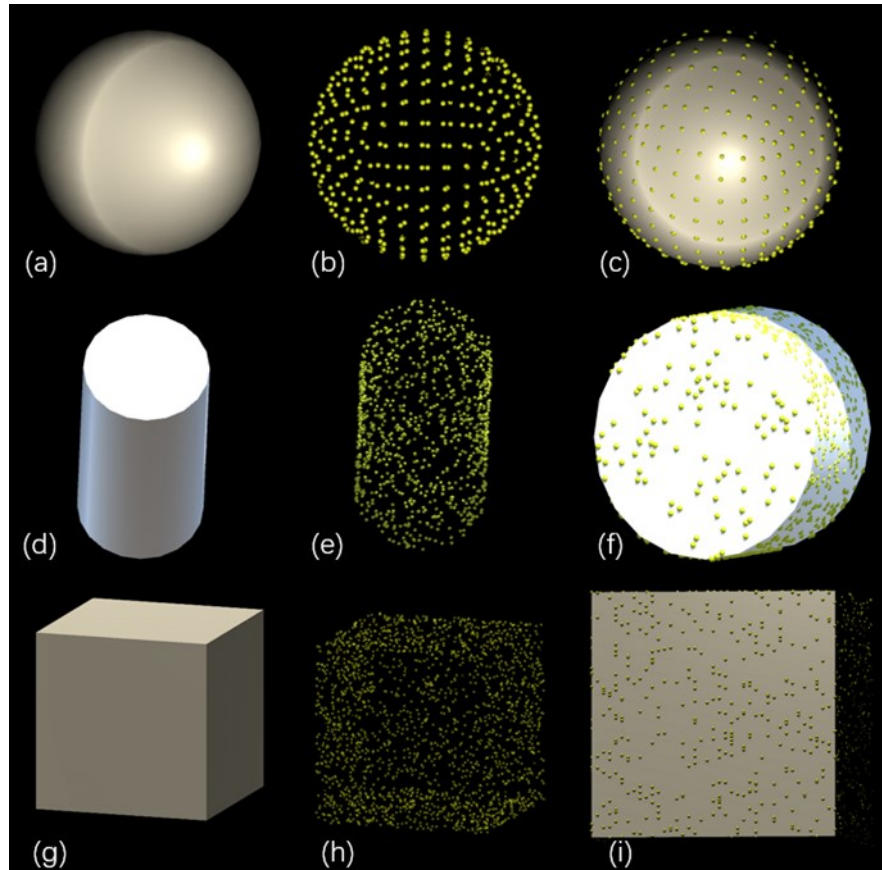
Figure 4-2. Regular shaped objects and corresponding point clouds: (a) Unity default sphere model; (b) sphere mesh vertices used as point cloud, 515 points in total; (c) overlap of sphere with its point cloud; (d) Unity default cylinder model; (e) cylinder re-sampled point cloud,1000 points in total; (f) overlap of cylinder with its point cloud; (g) Unity default cube model; (h) cylinder re-sampled point cloud; (i) overlap of cube with its point cloud.

4.1.3 Artificial Stems

After the tests using regular shape objects, the next attempt was to apply VWD in point clouds of artificial stems. It should be noted that the artificial stems were simpler than the artificial trees generated by algorithms in other studies [148]. The reason was that Unity is not designed for scientific purposes. Meanwhile, the physical simulation is a high-power consumption process. Therefore, a stem with a minimum crown area would help to reduce the consumption of virtual water molecules (VWMs). Tree editor in Unity was used to create two artificial stems manually [149]. As shown in Fig.4-3, the "stem" model had only a main stem without any branches. The "stem with branches" model had three additional

children branches based on the "stem" model. They were re-sampled to a point cloud using the following method.
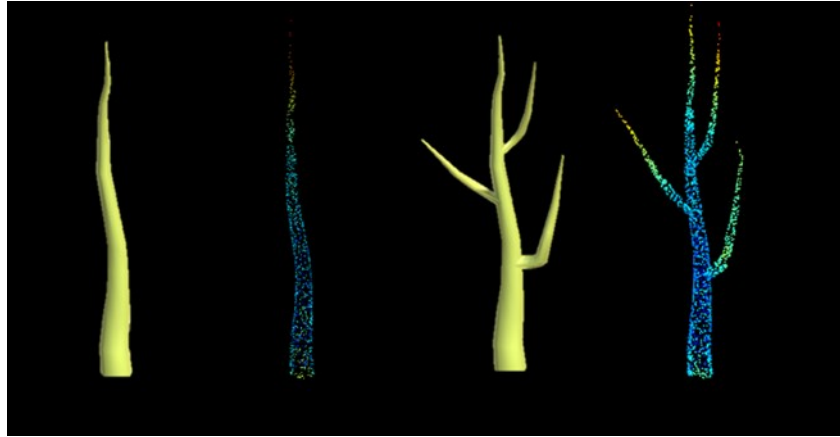
Figure 4-3. 3D models and the corresponding point clouds of two types of artificial stems. Left: the" stem" model and its point cloud; Right: the "stem with branches" model and its point cloud.

Point Cloud Library (PCL) [150] and Visualization Toolkit [151] were used to re-sample 3D models back to point clouds. Once a 3D model was re-sampled, a pair of a 3D model and the corresponding point cloud was determined. The volume of the corresponding point cloud was known, which was the volume of the 3D model. This was how the exact ground truth for a point cloud was obtained.

This re-sampling work was utilized by an interface in PCL. There were actually two similar interfaces in PCL, which were *<fromPCLPointCloud2>* and *<pcl_mesh_sampling>*. A simple call of the *<fromPCLPointCloud2>* interface would lead to the points concentrated around the area of vertices and left great gaps on the surface of triangles. It was insufficient to generate an evenly distributed point cloud to simulate a terrestrial LiDAR-derived point cloud. Therefore, the *<pcl_mesh_sampling>* interface was used. This interface could be further combined with the Visualization Toolkit. After that, a 3D object, e.g., a tree model, could be re-sampled into a point cloud with an even distribution of points. In addition, a random method was applied to simulate the natural distribution of points on the stem surface. As shown in Fig.4-2 (f) and (i), the larger gaps might represent the data defect caused by perspective blocking or noising.

Moreover, QSM modeling on the point cloud of "stem with branches" was applied

using Simpletree (Jan, Freiburg, Germany) [152]. The modeling process was a single-blind experiment. Without knowledge of ground truth, the tester's most satisfactory result was marked as "Fine". Then random jitters on the tester's input parameters were applied. This test was recorded in Tab.4-2. The full workflow for preparing the artificial objects and artificial stems are shown in Fig.4-4.

Table 4-2. A simulation of human influence in the volume of whole tree (V) estimation using Simpletree: Fine refers to a first fine quantitative structure models (QSM) model before the others; R.1 to R.10 refers to the No.1. to No.10 QSM model using random changes on parameters based on the first fine QSM model; P.1 to P.10 refers to parameters using in the "choose thresholds" UI in Simpletree [152]; Vol(l) refers to the stem volume (total wooden volume in this dataset) with the unit litter.

Parameters	Fine	R.1	R.2	R.3	R.4	R.5	R.6	R.7	R.8	R.9	R.10
P.1	1.634	1.647	1.626	1.622	1.626	1.632	1.619	1.645	1.630	1.630	1.630
P.2	0.048	0.047	0.049	0.049	0.049	0.049	0.047	0.049	0.047	0.047	0.049
P.3	0.052	0.051	0.051	0.051	0.051	0.053	0.051	0.053	0.051	0.053	0.053
P.4	0.030	0.029	0.031	0.031	0.029	0.029	0.031	0.031	0.029	0.029	0.031
P.5	173	174	172	173	173	173	175	174	172	173	171
P.6	10000	9915	9967	10042	9913	9975	9953	10053	9907	9957	10052
P.7	3	4	3	4	3	3	4	3	4	3	4
P.8	5	6	6	4	4	6	6	4	4	4	4
P.9	0.094	0.095	0.095	0.093	0.093	0.093	0.093	0.095	0.093	0.093	0.09
P.10	0.063	0.062	0.064	0.062	0.064	0.062	0.062	0.062	0.062	0.062	0.062
Vol (l)	26.44	24.97	26.32	26.31	26.96	25.58	26.81	26.44	25.86	25.86	26.16

Ground truth volume is 27.945 l (27945 in unit system in Unity).
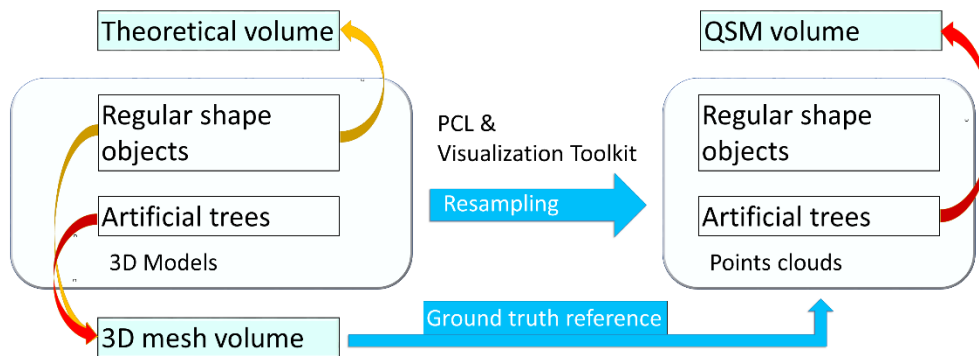
Figure 4-4. Workflow for preparing artificial ground truths with the re-sampling process using Point Cloud Library (PCL) and Visualization Toolkit.

4.2 LiDAR field measurements for the sunlight analysis methods

4.2.1 General information and acknowledgments

Different from the development of VWD methods, each stage of sunlight analysis methods had its own data sources. In stage one, the field measurement was undertaken on the campus of Beijing Forestry University, incorporated with Prof. Jia Wang and colleagues in his department. In stage two, the field measurement was undertaken in a forest site in Finland, incorporated with Dr. Xinlian Liang and colleagues in his department. Hereby, I express my sincere thanks again for the excellent cooperation with them.

4.2.2 LiDAR field measurement in stage one

On 14th Jan 2015 (winter season, leaf-off), the field data collection was carried out on the campus of Beijing Forestry University (40°0'07" N; 116°20'33" E), 44 m above sea level, 12 km northwest of the city center of Beijing, China. The mean annual precipitation sum amounts to 542.7 mm with a mean annual air temperature of 13.1 °C, ranging between a monthly average minimum air temperature of -2.9 °C and a maximum of 26.9 °C. The tree species were American sycamore (*Platanus occidentalis L*) and the trees have been planted as landscape trees.

At daytime, three TLS multi-single scans were made using FARO Photon 120 scanner (FARO Technologies Inc., Orlando, USA) for an area of about 15mX25m, including eight trees. Table 4-3 shows its specifications. The scan mode was set to 360° horizontal scanning with the measuring speed at 244,000 pts/sec. No reflectors or reference balls were implanted. Eight trees were in this plot as shown in Fig.3(a). A tree in the plot center, marked using green, had the best scanning condition. Therefore, this tree was selected as the demo tree and was processed by the following sunlight analysis. The scan positions were set up along the main road of the campus with the intervals about 10-30 m. Fig.3(a) also shows the distribution of scanning positions.

Compared to a typical setting for the single tree scanning [26], there was an absence

of a scan position in the west-south area. This absence simulated what may happen in real forests. Many factors, e.g., tree density, season, accessibility, terrain, prevent an ideal distribution of scanning positions for single tree modeling. Sunlight analysis aimed to provide a fast and easy method for assessing the theoretical light conditions for NFI sample plots. Therefore, the compatibility to adopt different data quality had to be considered in this developing stage. Further, LiDAR has been utilized in forest studies for decades, produced a varied amount of archive data. It cannot be guaranteed that all archive data are perfect for single tree modeling if we intend to make a time-series sunlight analysis. Thus, the impact on data quality is worth to be investigated in this developing stage of sunlight analysis.

Table 4-3. Technical data of the FARO Photon 120.

Parameter	Value
Wavelength	785 nm
Beam divergence	Typical 0.16 mrad (0.009°)
Beam diameter at exit	3.3 mm, circular
Range	0.6 m -120 m
Measurement speed (Pts/Sec)	122,000 / 244,000 / 488,000 / 976,000
Ranging error	±2mm at 10m and 25m, each at 90% and 10% reflectivity
Field of view (vertical/horizontal)	320° / 360°
Step size (vertical/horizontal)	0,009° (40,000 3D-Pixel on 360°) / 0,009° (40,000 3D-Pixel on 36(

4.2.3 LiDAR field measurement in stage two

The LiDAR field measurement was applied in April/May 2014 with a Leica HDS6100 scanner (Leica Geosystems AG, Heerbrugg, Switzerland) [18]. Table 4-4 shows its specifications. This LiDAR sample plot was a rectangular forest plot, 32-by-32 m in size, in a southern boreal forest in Evo, Finland (61.19ºN, 25.11ºE). The main tree species were Scots pine *(Pinus sylvestris L.)*, Norway spruce *(Picea abies L. Karst.)*, silver *(Betula pendula Roth),* and downy *(Betula pubescens Ehrh.)* birches. The stem density was about 600 trees/ha. There were 51 trees in this sample plot.

Table 4-4. Technical data of the HDS6100.

Parameter	Value
Wavelength	650–690 nm
Beam divergence	0.22 mrad (0.013°)
Beam diameter at exit	3 mm, based on Gaussian definition
Range	79 m
Measurement speed (Pts/Sec)	Up to 508,000
Ranging error	±2mm at 10m and 25m, each at 90% and 10% reflectivity
Field of view (vertical/horizontal)	310° / 360°
Step size	8 mm at 25m; 14mm at 50m

4.3 Conclusion of data collection

The raw format of data in two CVM implantations were point clouds. However, raw point clouds in sunlight analysis method would be further processed into tree models. Thus, literately, the measuring targets exhibited great differences in two CVM implementations. In the followed chapters, VWD methods would measure raw point clouds, and sunlight analysis method would measure tree models. From another perspective, they were united again in represent real trees (as solid objects) in virtual space despite their data forms. Could see that from here, the principle of CVM method was that the data were regarded as objects. Meanwhile, the format of data was not limited.

Another difference of data in two CVM implementations was their origin. Artificial point clouds, which contained a few thousand points, were used in VWD methods. That was because, current computer performance was not capable of supporting full-size point clouds scanned from real trees for VWD method. Meanwhile, real tree point clouds were utilized in sunlight analysis because sunlight analysis was not an independent method. The preprocessing data steps converted millions of points in point clouds into tree models, which had simple data structures.

Chapter Five

Methods

5.1 Methods in virtual water displacement

5.1.1 General information of VWD methods

VWD methods aimed to simulate the water displacement method in virtual space. The virtual measuring tool of VWD methods consisted of the simulation of the physical behaviors of water. The measuring target was the point cloud. The input was the point cloud. The output was the stem volume. There were two stages in the development of VWD methods, i.e., stage one: VWD using massive virtual water molecules and stage two: VWD using few VWMs. In stage one, the study focus was on how to reconstruct the physical scenarios of real water displacement method in virtual space. Meanwhile, it was a pilot stage to provide experience to all the following works in this thesis. In stage two, serval problems found in stage one was solved. The improvement in stage two showed a potential fully automatic workflow to measure the volume directly on the point cloud without modeling.

5.1.2 VWD Methods in stage one, displacement using massive VWMs

5.1.2.1 Water displacement method

The physical characteristic of water is vital of importance for water displacement method. Any shaped object can be encased by the water completely, which is a perfect method for the volume measurement of irregular objects only if the vessel is large enough [153]. For some small objects, such as the human body, LiDAR showed the potential to provide an equivalent accurate estimation of volume, compared with conventional water displacement methods [154,155]. However, the complexity of tree structures prevents the delicate surface reconstruction using LiDAR data.

As shown in Fig.5-1, the water displacement method is used primarily in stem density measurements currently. In this measurement, both volume and weight are directly measured variables. Then, wooden density and volume of the tree can be determined with the following equations [156]. Where ρ is wooden density; m is the weight of stem disk; v is the volume of stem disk; M is the weight of whole tree (all stem disks); and V is the

volume of whole tree.

$$\rho = \frac{m}{v} \tag{5-1}$$

$$V = \frac{M}{\rho}. \tag{5-2}$$

Figure 5-1. Water displacement method for wood density (photograph taken by Prof. Baitian Wang in Beijing Forestry University).

5.1.2.2 Ideal point clouds and ideal tree models

As previously stated in 4.1.2 and 4.1.3, the artificial point clouds were re-sampled from 3D models. Compared to point clouds from real LiDAR scannings, those point clouds had the following features: (i) all structural information on the object surface was recorded; (ii) a generally equivalent distribution of points. Those point clouds were defined as ideal point clouds.

After the definition of ideal point clouds, an assumption was raised that applying a computational modeling (CM) method, e.g., QSM method, on an ideal point cloud could result in an ideal tree model. In an ideal tree model, each cylinder has a perfect fitting on each part of a tree. However, a specific CM procedure is depended on method parameters. Due to the diversity of tree structure and the modeling mechanism of CM methods, it is believed that it would not be possible to have a specific group of parameters that can generate all cylinders in the right position. Because the modeling target of CM methods is the tree, but not the cylinder (the tiny part of trees). Trees and cylinders are in different

spatial scopes. In the end, a simple conclusion could be made that, for an ideal point cloud, the corresponding ideal tree model could not be made using CM methods.

5.1.2.3 Primary mechanism of VWD

The virtual water displacement method is a series of computer algorithms, including physical simulation functions from PhysX, to simulate the laboratory process of water displacement method for stem volume measurements in virtual space. Instead of collecting the increment data from a graduated cylinder or weighing the mass of water, the quantity of displaced virtual water molecules (VWMs) is counted one by one to calculate the mass of water, subsequently, the volume of stem will be determined. This procedure can be described as the following equations, where V is the stem volume; k is the coefficient of volume calibration; N is the predicted number of VWMs for a vast vessel; n is the actually filled number of VWMs in a vessel with a tree point cloud inside; and v_s is the sphere volume of a VWM.

$$V = k(N - n)v_s. \tag{5-3}$$

5.1.2.4 The establishment of the VGE

The establishment of VGE is the first step. A vast 3D Euclidean space was created using the default setting in Unity Scene [146]. The position of each object in this space was determined by three coordinates (x, y, z). The original point was (0, 0, 0). According to the human acts of cognition, a flat (z=0) was used to separate this space into the aboveground and the underground visually. Then, a cube which represented a graduated cylinder in reality (Fig.5-2) was set on this flat. There were two reasons for choosing a cube as a vessel for water displacement. First, the circular packing problem was the primary consideration, as the rectangle (2D) and cube (3D) exhibited well-discussed solutions [157]. The secondary consideration was that the shape of cube had a simple 1-1 relationship with the Array data structure in C# [158]. Finally, a tree point cloud, which was a virtual representative for a tree in reality, was imported into the center area of the vessel.

58
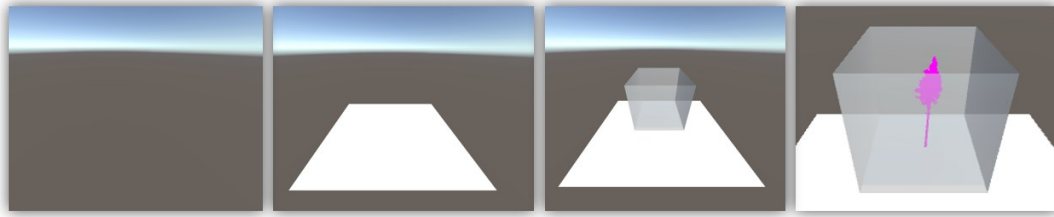
Figure 5-2. The procedure of the establishment of the virtual geographic environment (VGE).

5.1.2.5 Virtual water molecule

Visualization is a major research focus in computer graphics, but not quantitatively [159-161]. One liter of water contains ~55.56 mol of water molecules, which equals ~$55.56*6.02*10^{23}$. The simulation on this order of magnitude was impossible and meaningless using a desktop computer. A test showed that the capability of VMWs was less than 10000 in the desktop computer used in this study. Thus, it had to use a limited number of VWMs by enlarging the diameter of VWMs dramatically. In this case, a VWM is no longer a representative of a water molecule (cluster) on molecular scale. A VWM is a collection of certain quantity of water with a fixed shape on normal scale, which can be observed by human eyes.

VWMs are of vital importance, with particular regard to two aspects: static and dynamic.

Static: A VWM plays as a volume placeholder. Visually, a VWM is a sphere made up of a mesh; in the physics simulation process, it is a sphere with dynamic coordinates and a fixed user-determined radius. The exclusivity is its key feature. No matter where it is, it is not allowed for other objects to overlap with it. In this way, a VWM can exclusively occupy an area in Euclidean space in a VGE, which is equivalent to the behavior of a water molecule (cluster) in reality. As a volume placeholder, the volume of the VWM consists of two parts: one is its own sphere volume, which is a determined value related to radius; the other one is the gap volume shared with other neighboring VWMs, which is related to the quantity and distribution all of VWMs. A specific VWD process has a corresponding coefficient for volume calibration. How to determine this coefficient is discussed in 6.1.1.2. Because this coefficient was not designed at the stage of method development. The volume

of VWM can be described as in the following equations, where v_s is the sphere volume of a VWM; r is the radius of a VWM; V is the volume of VWM; v_g is the gap volume shared with other VWM; and k is the coefficient of volume calibration from VWM sphere volume to VWM volume (as a volume placeholder).

$$v_s = \frac{4}{3}\pi r^3 \qquad\qquad (5\text{-}4)$$

$$V = v_s + v_g \qquad\qquad (5\text{-}5)$$

$$V = kv_s. \qquad\qquad (5\text{-}6)$$

Dynamic: Physics research regards water molecules (clusters) as rigid bodies which are solid bodies with no deformation or with deformation so small that it can be neglected [162]. The simulation of rigid body dynamics is supported by the PhysX engine in Unity [163].

The motion simulation of single VWM is the first step. Four key features in rigid body dynamics were applied, in order to move a VWM like a water molecule (cluster) in VGE. (i) Velocity: The simulation for velocity is the fundamental function for the physical engine. The motion of a VWM is separated into linear and angular velocity components. By calling the corresponding interfaces, *<PxRigidBody::setLinearVelocity>* and *<PxRigidBody::setAngularVelocity>*, the motion of six degrees of freedom was simulated. (ii) Mass Properties: According to a real water molecule (cluster), a VWM needs a mass as well. With a mass, it can fall from the generation point down to the bottom of a vessel. By calling the interface *<PxRigidBodyExt::updateMassAndInertia>*, it could set a mass to a VWM and all VWMs share the same value of mass. (iii) Applying forces and torques: A force could be applied to a VWM if it has a mass by the following equation [164]. Where $\vec{F}$ is a force on a VWM; m is the mass of a VWM; and $\vec{a}$ is an acceleration parameter.

$$\vec{F} = m\vec{a}. \qquad\qquad (5\text{-}7)$$

In addition to adding a force for the movement in Euclidean space, a torque could be applied to a VWM using Eq.5-7 as well. (iv) Gravity: if $\vec{a}$ is replaced with $\vec{g}$ (gravity) in

Eq.5-7, it could simulate a VWM motion that was attracted by gravity with the following

equation [164], where $\vec{F}$ is a force on a VWM; m is the mass of a VWM; and $\vec{g}$ is the

gravity.

$$\vec{F} = m\vec{g}. \tag{5-8}$$

Gravity is a common force supported by PhysX in scene-wide (VGE-wide). The

magnitude of the gravity value does not affect the VWD result; it only affects the running

speed of the program. These four key features together with other auxiliary simulations

supported a VWM in behavior as a water molecule (cluster) in reality [141].

The interaction simulation between VWMs is the second step. As discussed within

this section, the exclusivity is its key feature for VWM. Rigid body collision was used to

ensure a VWM cannot penetrate with other VWMs as well as the boundary of vessel in the

motion simulation [165]. There are two key steps to set up the collision detection. (1) A

sphere collider was added to a VWM with exactly the same centroid and radius. This

collider is not drawn in VGE using mesh in the user interface (UI) visually, the surface of

a collider is perfect sphere by real-time mathematical calculation. Any object colliding with

the surface of the collider can trigger the movement on both objects. (2) The selection of

collision detection algorithms, sweep-and-prune (SAP) and multi box pruning (MBP) are

supported by PhysX [166]. MBP is a newer method that uses box shape as collider surface

and is more efficient than SAP. However, SAP was used because it can handle the original

shape of the VWM collider [167]. Once the collision was detected, objects will be granted

a new direction of movement and velocity following the physical law in Eq.5-7. To sum up,

a VWD is the carrier of both static and dynamic processes. A demonstration for a VWD

taking on different roles is in Fig.5-3.
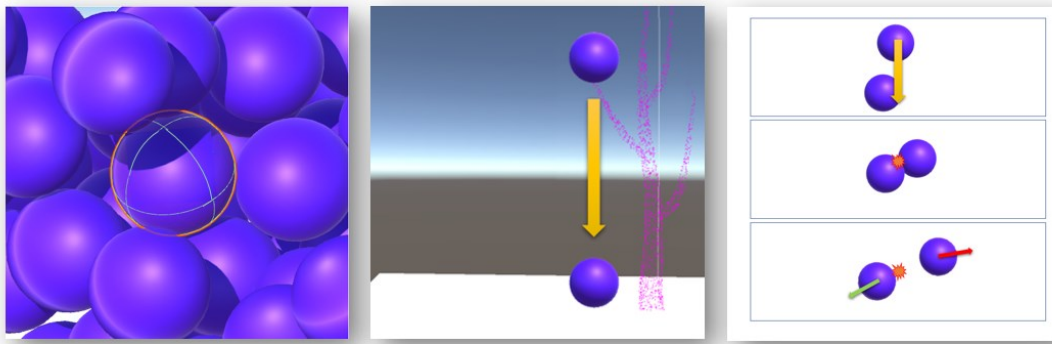
Figure 5-3. Static and dynamic roles of virtual water molecules (VWMs). Left: The exclusivity of a single VWM is guaranteed by a rigid body sphere collider. A VWM volume is made of its sphere volume and its surrounding gap volume shared with other VWMs; Middle: A VWM has a mass and is attracted by a gravity field. Right: Collision of two VWMs.

5.1.2.6 Point clouds as object

In VWD, each single point in the point cloud is not data to be processed. Each point is recognized as a living being in VGE, that holds its own position and rejects VWMs during the whole simulation process. In this study, each point was replaced by a sphere object which had a tiny diameter (not zero). All points together in VGE are equal to a tree in reality. Both the roles of VWMs and real water are to measure the objects.

5.1.2.7 Diminishing the modeling complexity

Compared to CM methods, the key feature of VWD is diminishing the modeling complexity by do not make tree models anymore. The previously stated section (5.1.2.2) assumed the concepts of ideal point cloud and ideal tree model. Theoretically, each ideal point cloud has a corresponding ideal tree model.

Now, two VGEs were conceptually created. Then, an ideal point cloud was installed in a VGE, and its corresponding ideal tree model was installed in another one. Then, a sphere collider was applied to each point in the ideal point cloud and a mesh collider to the corresponding ideal tree model. Both colliders had the same function, which prevented the penetration of a VWM to move from one side to another side [168].

As shown in Fig.5-4, if VWMs were used to collide with the point cloud and tree model at the same time, colliders on points or the tree model would hold an exclusive space, which was a wooden part of a tree. Thus, for the purpose of stem volume estimation only, the computational modeling procedure is no longer necessary. That is why VWD method is a "modeling free" method.

As previously stated in 5.1.2.2, it is impossible to build a perfect computational tree model from an ideal point cloud. On the contrary, VWMs can detect all of the surface areas on an ideal point cloud, which is equivalent to the surface of an ideal tree model. The only requirement is that the diameter of VWM is larger than the gaps for adjacent points. The VWD estimations of volume should be equivalent no matter if the input is an ideal point cloud or its corresponding ideal tree model. Thus, for the estimation of stem volume, VWD is a superior method compared to computational tree models at the algorithm level.
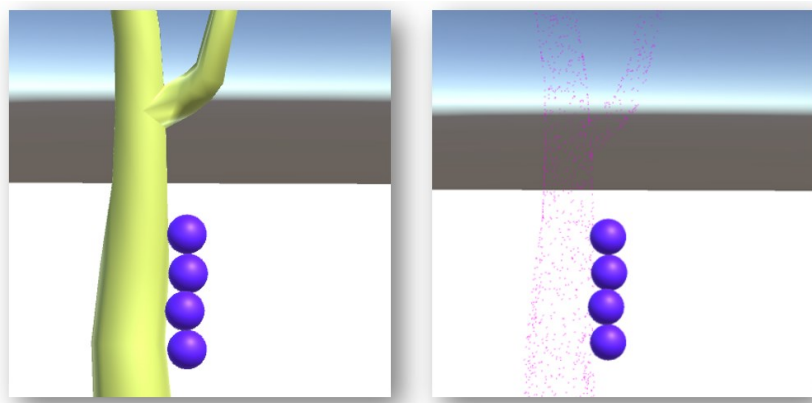
Figure 5-4. The demonstration of the similar response of VWMs for the solid tree model (left) and its corresponding point cloud (right).

5.1.2.8 VWD workflow

Finally, a VWD simulation can be start, which measures the point cloud in VGE, as the WD method measures the stem disk in reality. They share the same principle, which is the volume displacement by an alternative material, water. VWD use colliders attached on point cloud to simulate the water resistance in nature. In an ideal point cloud, VWD can provide a volume estimation on a true volume in VGE theoretically. The summary of the workflow of VWD is in Fig.5-5.
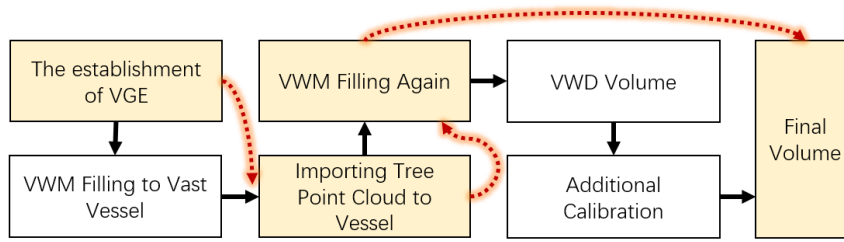
Figure 5-5. Theoretical (yellow) and full workflow for virtual water displacement (VWD) simulation.

5.1.2.9 Sphere packing problem

The coefficient k in Eq.5-3 and Eq.5-6 is a key parameter for VWD. The sphere packing problem was used to determine how many spheres (n) can fill a certain vessel. After that, k can be determined by the following equation. Where k is the coefficient of volume calibration from VWM sphere volume to VWM volume (as a volume placeholder); V_{vessel} is the volume of vessel; n is the number of theoretical maximal filling of VWMs; and v_s is the sphere volume of a VWM.

$$k = \frac{V_{vessel}}{n v_s}.$$

(5-9)

For the determination of n, the basic quasi physical (BQP) method was used [169]. BQP regards each sphere as a non-rigid body. Each sphere has its own elastic potential energy. By releasing the elastic potential energy in the whole system step by step, the energy of each sphere would be equal in the end. However, the motion of VWMs is driven by virtual gravity in VGE. It is not possible to distribute to the form of mathematical maximal. Thus, an imperial method was included to determine k with the following equation. Where k is the coefficient of volume calibration from VWM sphere volume to VWM volume (as a volume placeholder); V_{vessel} is the volume of vessel; n' is the actually filling number of VWMs; and v_s is the sphere volume of a VWM.

$$k = \frac{V_{vessel}}{n' v_s}.$$

(5-10)

In Eq.5-10, the actual filling experiment for each diameter was performed, repeated five times, to determine the value of n'.

5.1.3 VWD Methods in stage two, displacement using few VWMs

5.1.3.1 Aims of the development of stage two

In the development of stage one in the VWD, the water displacement method was simulated using massive VWMs. The simulation of massive VWMs was similar to the natural phenomenon of water, which is the accumulation of water molecules. However, due to several factors, e.g., computer performance and limitations in PhysX, few empirical calibrations had to be employed. Obviously, no empirical processes are included in the water displacement method in reality. Therefore, in this second stage of VWD method, several improvements were made to get rid of all empirical processes.

5.1.3.2 Flood area using single (or few) VWM: the new physical simulation scenario

As previously stated (in 5.1.2.5), each VWM was of vital importance, regarding two aspects, i.e., static and dynamic processes. In the static process, a VWM played as a volume placeholder. In the dynamic process, it simulated the motion of water molecule (cluster) in reality to reach an even distribution in VGE. In order to optimize the consumption of computer performance, this new flood area mechanism was developed using a few VWMs, instead of the simulation of the interaction of massive VWMs. The following were the steps of flood area mechanism.

(i) Voxelization. All the areas in the virtual space (a vast vessel for filling water) were converted to the voxel space. Each voxel was filled with a negative mark, e.g., 0 or false, indicating that the voxel was not occupied by water.

(ii) Generated a single (or few) VWM inside the vessel. The diameter of the VWM should be great than the average gap of the adjacent points of the tree point clouds.

(iii) Applied a gravity field in VGE with a random 3D direction.

(iv) The VWM was attracted by the gravity field and started to move. Its footprint was recorded in the voxel using positive values, e.g., 1 or true, indicating that the voxels were occupied by water.

(v) The direction of gravity was set to a new random value, once the VWM collided

with point clouds or the walls of the vessel.

(vi) Repeating step (v) until meeting a specific threshold, e.g., the running time.

By performing these steps, the flood area mechanism could be fulfilled using only one VWM, which significantly diminished the consumption of computer performance. Meanwhile, the uncertainty from the interaction of VWMs no longer existed. Thus, Eq.5-3 in the first stage could be transformed into a simpler form as the following Eq.5-11. Where V refers to the volume of the tree; V_{vessel} refers to the volume of the vast vessel; V_{flood} refers to the volume where the VWM has been visited.

$$V = V_{vessel} - V_{flood} \tag{5-11}$$

From the viewpoint of users of VWD, the only actions that the user has to do are the release of VWMs and the stop of simulation. The whole processes are parameters free, which are equivalent to operate water displacement method in reality.

5.1.3.3 Improvements on time efficiency

The flood area mechanism was designed as a parameter-free and empirical-regression-free method. Meanwhile, it was improved on computer performance. However, as a compromise of the using of few VWMs, the running time of the flood area mechanism prolonged to an ultra-long scale. The reason was that the position of one VWM was calculated frame by frame using PhysX. In the computer graphic, Frames Per Second (FPS) was used to evaluate the performance. It simply assumed that the FPS of a VWD simulation was 100, which meant a VWM could visit 100 voxels per second. It assumed further that a cube vessel with side length 100. Then this vessel had 1,000,000 voxels. In order to take a full visit to all voxels using a VWM, it took 10,000 seconds (~2.7 hours). Furthermore, the motion of the VWM was driven by a random gravity field. It would also extend the time for a full visiting.

Two strategies were developed to improve time efficiency. The first strategy was the multiple releasing of VWMs. By duplicating one VWM to multiple (n) VWMs, the time efficiency increased to the maximal n times without the consideration of a voxel. The voxel

was visited by the same or different VWMs repeatedly. However, more VWMs consumed more computational resources and decreased FPS. The second strategy was to apply the buffer for the visited voxel. As shown in Fig. 5-6, if a buffer with 1 unit was made, 27 voxels would be marked as the flood area.
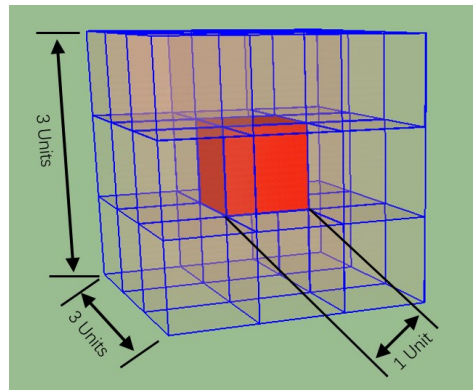
Figure 5-6. Voxel buffering for the improvement on time efficiency.

5.2 Methods in sunlight analysis

5.2.1 General information of sunlight analysis

Sunlight analysis methods aimed to simulate the interaction between sunlight and tree surfaces. The virtual measuring tool consisted of serious simulations including the motion of the sun, the emission of sunlight, the shading effect, and the radiation sensor. The measuring target was the tree surfaces and solar irradiation. The input was the tree models. The output was the distribution of solar irradiation on tree models.

5.2.2 Sunlight analysis methods in stage one, investigating single tree light condition

5.2.2.1 Overall workflow for sunlight analysis

There were two major steps in sunlight analysis: (i) creating a VGE with a tree model inside. The tree model is a receiver for recording illumining conditions of sunlight which correspond to full coverage on a real tree with radiation sensors; (ii) simulating the motion of the sun and the interaction of sunlight with the tree model.

The primary work in the first step is to set up a virtual representative for a real tree in the computer system. LiDAR was adopted as the data source, attributing to its high

positional resolution, fast scanning speed, and simple source of error [48,170]. After field scanning using LiDAR, a living tree in the reality was transferred into a digital form as a point cloud. However, the form of the point cloud only contains unconditional information of positions and intensities. It had to be converted into tree models, which could be recognized by human beings. In this process, the quantitative structure model (QSM) was applied to modeling trees. The feature of QSM is the accumulation of cylinders, which is close to the natural form of trees [55]. Finally, the tree model was imported into another application, i.e., SketchUp, which is a 3D modeling software for architecture designs [171]. The built-in 3D Euclidean space in SketchUp and the QSM tree model together composed the static part of the VGE.

The second step is to simulate the motion of the sun, and the interaction between sunlight and tree models. Methods in the daylighting design of the architecture design were directly used to simulate a daylight condition for tree model [172]. There are various commercial software for sunlight analysis [173]. Due to availability, the Sunshine_pro_2019 (Arcdot, Beijing, China) was applied to perform the simulation with function restrictions [174]. After the sunlight analysis, statistics was conducted based on the analysis results, an illuminated tree model, using a self-developed application. Figure.5-7 shows the full workflow.
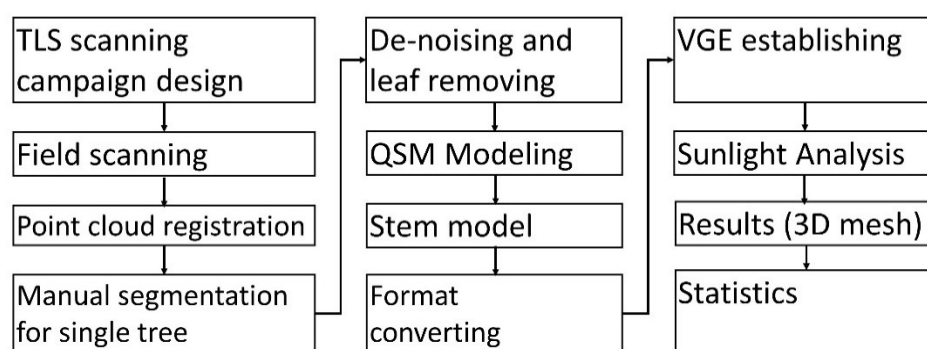
Figure 5-7. Full workflow from field data collection to the sunlight analysis results

5.2.2.2 Data pre-processing

The purpose of the data pre-processing is to extract point clouds for single trees from the raw TLS scans. Registration tools in CloudCompare were used by point pairs picking

to register point clouds from different scans [175]. The point pairs were chosen at corner parts of the campus building. After then, a rough dataset for the single tree was segmented manually.

Denoising and leaf removing are the critical works in data pre-processing. Based on the rough segmentation of the point cloud, manual deletion for the apparent parts was utilized, which did not belong to the single tree. Then, a voxel-based outlier filter was applied to remove the discrete points [176]. All the remaining points were clustered spatially using the density-based spatial clustering of applications with noise (DBSCAN) method [177]. Different thresholds were tested, and the results were inspected visually.

The process of leaf removing is similar to the denoising works. The leaves were regarded as noises in this study. A curvature filtering was applied to the point cloud. This method was based on the principal components analysis (PCA) for point's neighborhood [152]. Appropriate PCA parameters could distinguish the leaf from the stem structure of the tree. In the end, manual deletion for the remaining leaves, and manual repairing of some points on the stem were added.

5.2.2.3 Tree modeling

The role of the tree model is to provide a radiation receiver to receive virtual sunlight in the VGE. QSM method was applied to model the tree using SimpleTree application [152]. This application was also utilized in the data pre-processing work. SimpleTree was a user-friendly software and responded instantly to the change of parameters. Several parameters affected the tree modeling process. Initially, the default settings in SimpleTree with the function of parameter optimization was applied [152]. The outputted model was evaluated using visual inspection by overlaying the model with the point cloud. Furthermore, very small random changes with the amplitude within 5% on the modeling parameters were tested to find potential better modeling results.

5.2.2.4 Simulation of sun movement and solar irradiation

Simulation of sun movement and solar irradiation is the central process in sunlight

analysis. Compared to instant methods stated in section 2.3.3.6, sunlight analysis is a dynamic method, which measures the virtual tree from the sunrise to sunset. Moreover, it is a direct and full sampling measuring method, which gets rid of validation, calibration, and systematic sampling procedure. Previous steps prepared the virtual space and the virtual tree as a static radiation receiver. In this step, the motion of the sun in the sky, the sunlight emission, the shading in the tree structure, and the virtual radiation receiver were simulated by calling a third-party interface. Those four simulations contributed together as a specific virtual measuring tool for sunlight analysis.

Figure 5-8(a) describes the full process of sunlight analysis during the daytime. The virtual measurement started at the point of sunrise. According to a user-defined period, the position of the virtual sun changed step by step. In each step, a vector was calculated using the position of the virtual sun and the tree model to determine the direction of virtual sunlight. Then, a global parallel light was generated to illustrate entire rooms in the virtual space and followed with a prospective analysis [178]. Figure 5-8(b) shows the detail demonstration of perspective analysis.
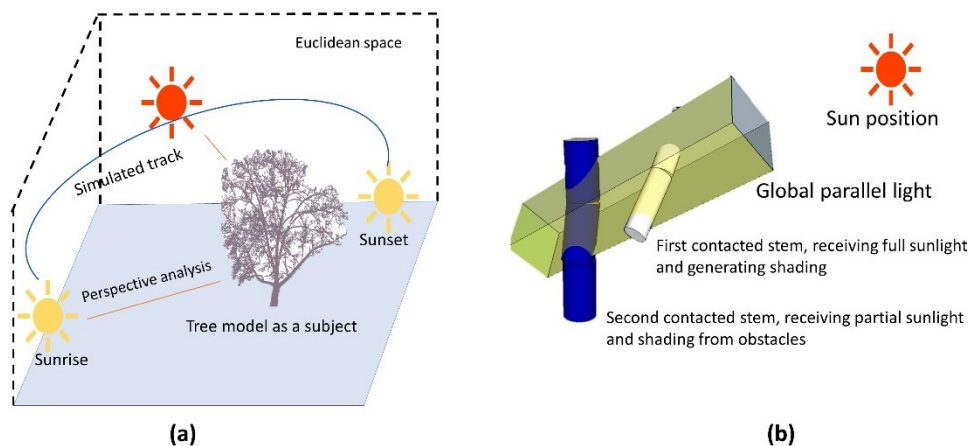
Figure 5-8. The procedure of sunlight analysis; (a) demonstration of the full process during the daytime; (b) detail demonstration of perspective analysis.

Sunshine_pro_2019, which is a plugin in SketchUp, was applied to perform sunlight analysis in this study. It is an application to assess light conditions for buildings [172]. The similarity between tree models and building models was analyzed. Both of them have

multiple faces and vertexes. They spread their bodies in 3D Euclidean space with exclusive occupation. Therefore, Sunshine_pro_2019 was utilized and successfully processed the demo tree model for assessing light conditions. In addition, the process for the demo tree model was restricted by the free licensed version. The simulation of sun motion was fixed in 6 and 8 hours in two specific days.

The parameters applied in the Sunshine_pro_2019 are as the following: (*geolocation* : 40°0'07" N, 116°20'33" E; *date* : "Da Han Ri", which refers to 20, January, sunrise at 07:33:08, sunset at 17:18:56, *simulating time span* : 08:00:00 to 16:00:00; *sweep angle* : not set; *minimal sunshine duration* : 5 minutes; *sample point spacing* : 0.5 m; *time interval of sun position*: 8 minutes). Notably, the tree model was magnified 30 times on each side length. Consequently, the equivalent *sample point spacing* for the original tree model is 1.67 cm.

5.2.2.5 Statistics

The result for sunlight analysis is a 3D mesh using the format of wavefront (obj), which is a commonly used 3D format in computer graphics [46]. Obj files use plain text to record 3D geometry including the following elements: vertex coordinates, vertex normals, faces with their corresponding vertices, texture vertices, texture rendering, and UV position for texture filling. Vertex coordinates, faces with their corresponding vertices, and texture rendering from the outputted mesh formed a new processing dataset. In this processing dataset, the area of each triangle was calculated [147], and the information of color and height was recorded. Four elements, the processing order, the area of triangle, the color, and the height contributed together to form the final result dataset. Finally, the final result dataset was imported into MATLAB for further statistics. Furthermore, the obj file is also the middleware for transferring data between different applications.

The statistical output of sunlight analysis contains the information of area connected with exposure duration with nine groups, of 0-1 hour,1-2 hours,2-3 hours,3-4 hours,4-5 hours,5-6 hours,6-7 hours, and 8 hours. Furthermore, three additional information are provided: (i) relative area of faces (triangles) is the area of all faces in an exposure duration

group divided by the full surface area of the; (ii) relative quantities of faces (triangles) is the quantity of all faces in an exposure duration group divided by the overall quantity of faces in the 3D result model; (iii) a ratio is relative area of faces (triangles) by relative quantities of faces (triangles).

5.2.2.6 Validation procedure

In general, no external reference was needed, which was one feature of this study. There were two major steps in this study, tree model and light condition analysis for tree model. For evaluating the tree model, it was preferred to use the visual inspection. Because the raw LiDAR point cloud itself was the ground truth reference for the spatial distribution of tree structure. Many studies used the comparing of physical quantities of stem volume to validate tree models *[24,26,148,152]*. However, from our perspective, the simple quantitively consistency has no relationship to the right distribution of tree structure. Therefore, the overlaying is an effective method. Furthermore, no more external reference was needed. The result of light condition analysis was free of validation. Because this method is a widely developed method in the field of architectural design. For decades, daylight analysis software is well developed. The principle of daylight software is also simple. As shown in Fig.5-8(b), form the perspective of computer simulation, there is no room of error. Therefore, it doesn't need to validate the sunlight analysis procedure. The uncertainty of sunlight analysis approached zero.

5.2.3 Sunlight analysis methods in stage two, investigating interferences from surroundings for single tree light condition

5.2.3.1 Aims of the development of stage two

In forests, every single tree generates shades to surroundings. While a single tree is affected by shades from other trees. Thus one primary growth strategy of trees is extending canopy structures in vertical and horizontal directions [82]. Through this strategy, single trees compete for sunlight by avoiding shades from other trees. Forest is an aggregate of trees. The effect of shades has been extensively studied at the scales of forests [84,179,180]. However, it is hard to be analyzed at single tree level. Because conventional measuring

instruments cannot distinguish the source of shades. Some studies tried to manually control the variables in reality. For example, Giday et al. analyzed shade levels on the survival and growth of planted trees with three canopy cover density [181]. Vanhovea et al. studied the positive relationship between tree shades and agricultural crops using artificial shades [182]. Ashton et al. demonstrated an effect of shade on leaf structure and physiology of tree seedlings [183]. However, those studies could not reflect the real situation in nature.

In the development of stage two in sunlight analysis method, the measuring targets were extended to be sample plots from single trees. By the establishment of virtual sample plots, the interference could be controlled manually. Finally, a quantitative assessment for how much shades reached to single tree from neighboring trees was achieved. Unlike the development of VWD methods in stage one, the changes of this stage two development were only in the different measuring targets.

5.2.3.2 Establishing a virtual sample plot

Similar to stage one development of sunlight analysis methods, there were two major steps, i.e., establishing a specific VGE and casting virtual measurement. In this stage, a specific VGE referred to a virtual sample plot (VSP). A VSP was a representative of a real forest sample plot in virtual space. The LiDAR measurements in the forest field provided two information to build fundamental infrastructures for the VSP, which were tree models and the spatial distribution of tree models. However, the raw LiDAR data was massive points. Those points contain information of positions and intensities, which cannot be utilized directly by the following sunlight analysis method. Therefore, two tree modeling methods, i.e., voxel modeling and QSM modeling, were applied to converted raw LiDAR data into 3D tree models. There were 51 single trees (DBH greater than 5 cm) in total. Due to the limitation on computer performance, it was not possible to apply sunlight analysis on a VSP with all 51 trees. Therefore, according to usual settings of NFI simple plots [11,184], the VSP was created with few trees, which was a subset of the full LiDAR plot.

Figure 5-9 shows the layout of the VSP and the full LiDAR plot. The shape of VSP was a circle with the diameter at 15m. Tree No.27 (T27) and Tree No.26 (T26) were

selected as target trees for investigating the shade effect. T27 was marked using a purple hexagon. It was a mature tree. Its height was 18.7m and DBH was 20.8cm. T26 was marked using a blue hexagon. It was a young tree. Its height was 7.9m and DBH was 5.4cm. Tree No.23, No.46, No.20, No.47, No.22, and No.29 were marked using green diamonds. Those six trees played the role of sunlight blocking obstacles for T27 and T26 in the VSP. Markedly, Tree No.29 was located out of the VSP. However, it was expected to project its shades on T27 and might on T26. Therefore, Tree No.29 was included in the VSP and be modeled. A conceptional line, marked using a dotted line, linked those six trees together. They belonged to the group of the closest neighboring trees, which projected shades on T27 and T26. Tree No.33 and No.34 were not modeled because they were in the north of T27 and T26. Tree No.18 was not modeled because it did not belong to the closest neighboring group.
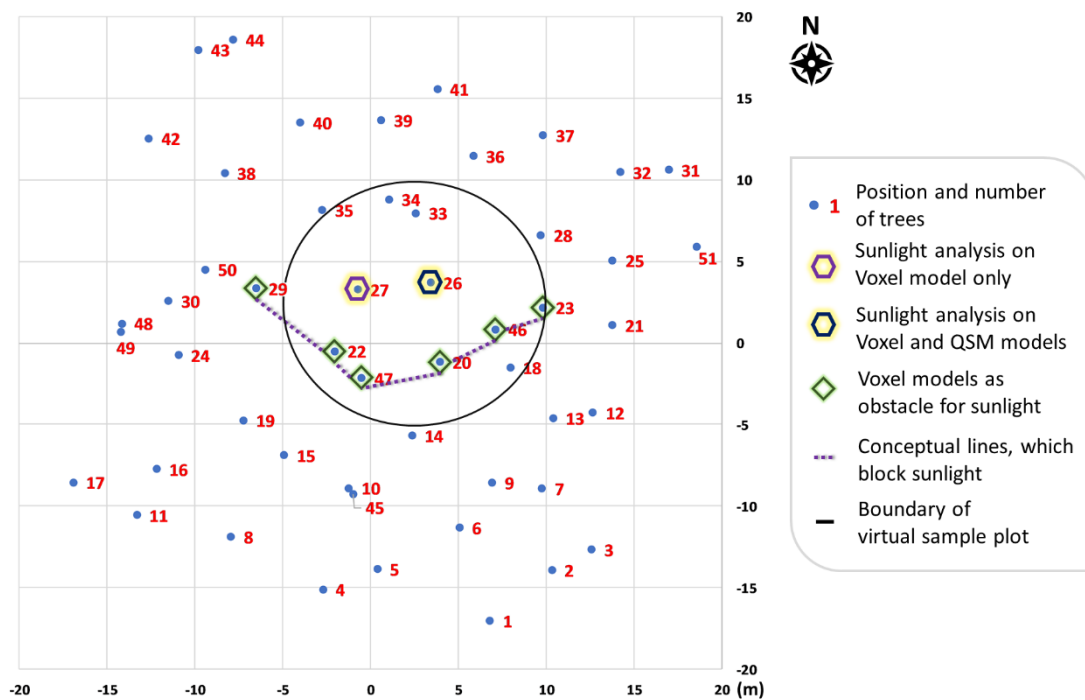
Figure 5-9. Layout of virtual sample plot prepared for sunlight analysis.

Two tree modeling methods were applied, i.e., voxel modeling and QSM modeling. In stage one development, QSM method was applied. Because the QSM model could be validated by visual inspection. It was easy to be manually corrected and had less prediction on tree structures [26,55]. Less prediction on tree structures was virtual of importance

because the tree model in virtual space was regarded as a copy of the real tree in CVM. Theoretically, each part of a tree model should be located in the real tree. However, the establishment of minimal prediction tree models required many conditions, e.g., winter leaf-off season, very low stem density and multiple scanning positions. Those requirements were hard to be fulfilled in some natural forest fields, e.g., the LiDAR plot in Finland. Thus, voxel modeling method was introduced in stage two. All eight trees were made using voxel method [185]. According to the principle of minimal prediction, leaves and stem were not distinguished. No matter how a voxel belonged to leaves or stem, there was no difference in receiving and blocking sunlight. Moreover, a QSM model for T26 was made because of the relatively good data quality. Finally, a VSP with eight tree models was constructed. T27 and T26 were the target trees for sunlight analysis. Six trees were used as the sunlight blocker.

5.2.3.3 Sunlight analysis in VSP

After the successful installation of the VSP, six sunlight analyses were applied on T27 and T26. Figure.5-10 shows these six scenarios with or without the interference from neighboring trees. Figure.5-10(a) shows that T27 was the only object in the VSP. The sunlight analysis provided the theoretical distribution of solar energy on the condition of receiving no shades from the environment. Then, the surrounding trees were imported, as shown in Figure.5-10(d), and applied sunlight for the same tree again. This result was affected by shades generated form six obstacle trees and T26. In the final step, a sample calculation was applied, to quantitatively assess the energy loss for a single tree duo to neighborhood shading. This was the difference from the two simulation scenarios.
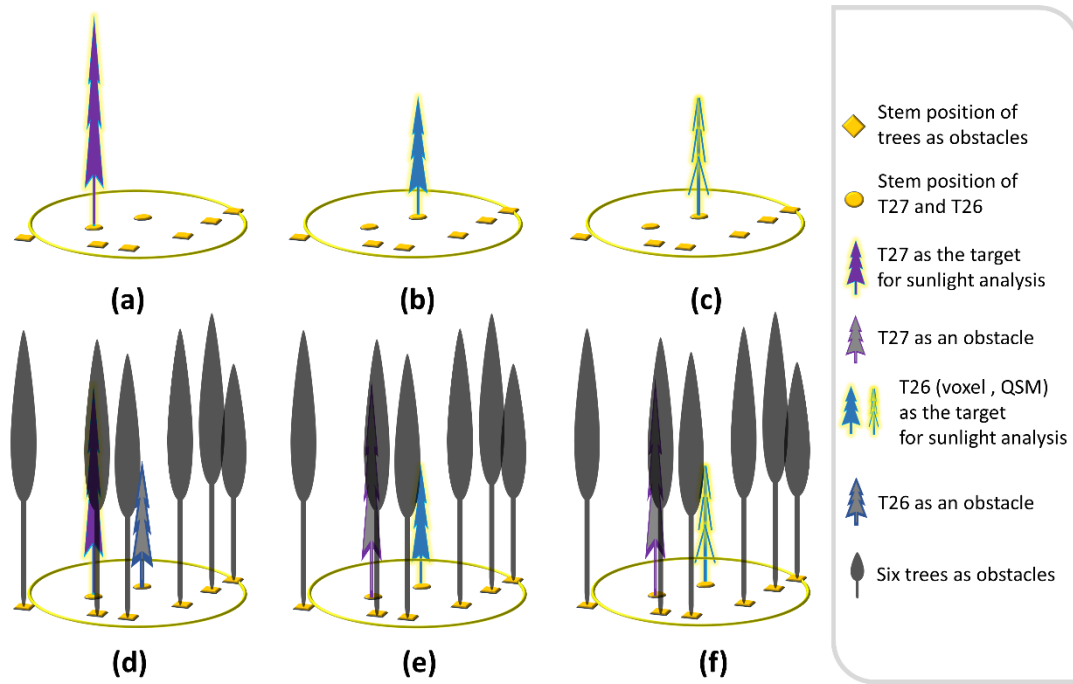
Figure 5-10. Six scenes for sunlight analysis; (a) sunlight analysis for T27 (voxel model) without neighboring trees; (b) sunlight analysis for T26 (voxel model) without neighboring trees; (c) sunlight analysis for T26 (QSM model) without neighboring trees; (d) sunlight analysis for T27 (voxel model) with neighboring trees; (b) sunlight analysis for T26 (voxel model) with neighboring trees; (c) sunlight analysis for T26 (QSM model) with neighboring trees.

Similar to sunlight analyses on T27, the same procedure was applied on T26 with voxel and QSM models. The QSM modeling was the initial modeling method applied in stage one. QSM model stored detail information of tree stem and branches structure. Compared to the QSM model, the voxel model depicted the main stem and the outlier of the canopy. Although, the shape of voxel, i.e., cube, was away from the shape of leaf. There was no difference in the role of blocking sunlight. Furthermore, T26 showed an example of applying the same sunlight analysis process on different tree models for the same tree.

5.2.3.4 Statistics and validation

There was no change in the mechanism of stage two of sunlight analysis. Accordingly, the statistics and validation procedure of stage two were exactly the same as stage one in section 5.2.2.6. To sum up, the tree models were validated by overlaying them with raw point clouds. The sunlight analysis process was regarded as free of validation.

5.3 Conclusion of methods

As demonstrated in chapter three, the primary work of a CVM implementation was an appropriate design of physical scenarios. After then, how to implement the design of physical scenarios was the next step. Two presented CVM implementations exhibited two solutions to the implementation of physical scenarios.

VWD method showed the first solution, which was the fully independent development. This solution required to explore in an uncharted area due to the lack of similar research. Therefore, regular-shaped objects were employed to test each physical scenario in both stages of VWD method. Then, the artificial stem was followed behind. The mechanism in the first stage of VWD tried to reproduce the physical scenario of water displacement method exactly. However, empirical processes had to be included, which did not need in reality. Therefore, stage two of VWD was developed and fulfilled the initial vision of CVM: a virtual measuring instrument without additional mathematical process. To sum up, the fully independent development was a difficult way to achieve the goal. It required the integration of multiple disciplines. Meanwhile, it was facile to manipulate raw data, improve algorithm logic and distribute independently.

Sunlight analysis was another solution to implement CVM with a specific tree parameter. It integrated exiting methods as a virtual measuring instrument literally. Compared to VWD method, two stages of sunlight did not change the physical scenario. The difference was the measuring target extended to a sample plot from a single tree. Although modeling methods were involved in the full workflow. Tree models made by QSM or voxel could be validated by raw point clouds. In this validation procedure, no additional reference was required. Therefore, broadly speaking, these modeling processes had less interference with the feature of CVM. To sum up, the development experience of sunlight analysis demonstrated an efficient way for CVM implementations.

Chapter Six

Results and Discussion

6.1 Results and discussion for virtual water displacement methods

6.1.1 Results and discussion of stage one, displacement using massive VWMs

6.1.1.1 Theoretical and actual filling of VWMs

The movement of each single VWM was driven by virtual gravity. VWMs were generated in a limited area above the vessel and had similar gravitational potentials in VGE. As same as the water molecules (clusters) in reality, the disorder in individual VWM movement was easy to be observed. Fig.6-1 shows a comparison between a theoretical filling and an actual filling of VWMs in the standard vessel. The standard vessel is a cube and its side length is 400. The spatial distribution for VWMs varied in each time of actual fillings. However, as the collection of all VWMs, it is hoped that the distribution of VWMs would not affect the quantity of VWMs.
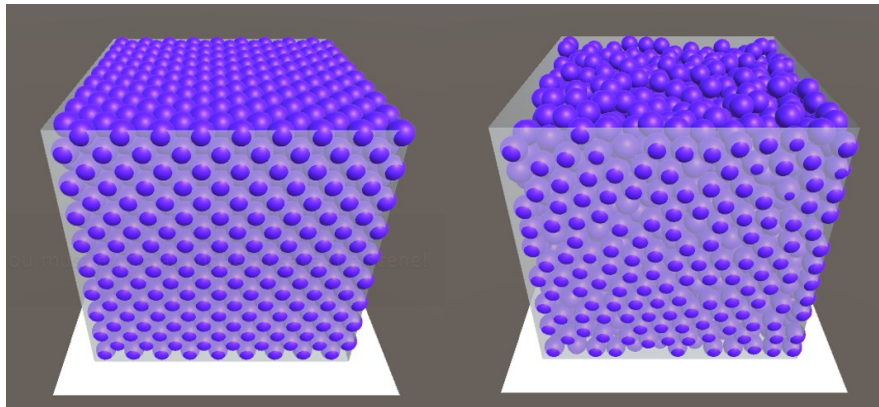
Figure 6-1. The spatial distribution of theoretical and actual filling of VWMs. The vessel is a cube with a side length of 400; VWM diameter is 30.72; Left: the theoretical maximal filling (2916); Right: the actual filling driven by PhysX (2431).

For the standard vessel, the theoretical filling was calculated using the BQP method for VWM in 17 different diameters from 21.416 to 43.245. The result varied from 8788 to 1000. The corresponding actual filling results were from 7227 to 891. Fig.6-2 shows the quantity difference between the theoretical and the actual. There is a clear trend that the relative difference between the two numbers increases with the shrink of VWM diameter. From the perspective of a whole system, introducing more VWMs amplified the disorder

of the system as well. On the contrary, the relative standard deviation (RSD) for filling test decreases with the VWM diameter at the same time. The largest diameter of VWM is 43.245 and the RSD is 1.375%; the smallest is 21.416 and the RSD is 0.465%. This indicates that the VWD method has high interobserver reliability in VGE.
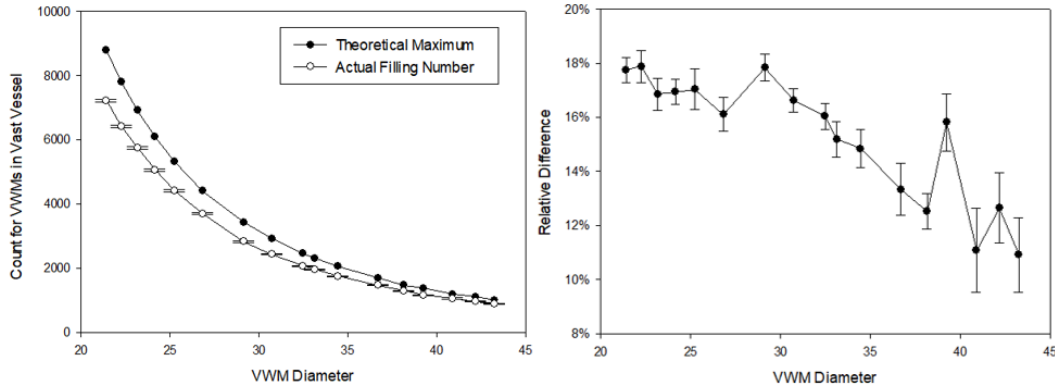
Figure 6-2. the actual filling experiment using VWMs with different diameters from 21.416 to 43.245 in a vast vessel. Left figure: The quantity difference between the theoretical and the actual with standard deviation; Right: Shows the relative difference between the theoretical and the actual with relative standard deviation.

Based on this result, the relationship between the theoretical and actual filling was investigated. Fig.6-3 shows a there is a strong linear relationship (r^2=0.999) between them. First, it proves the accurate performance of rigid body simulation by PhysX. On the other hand, it is possible to regress the actual filling number form the theoretical. Meanwhile, it indicates that skipping one filling step in the workflow (Fig.5-5) is possible. Subsequently, the *k* can be calculated using Eq.5-9 and Eq.5-10 as well.
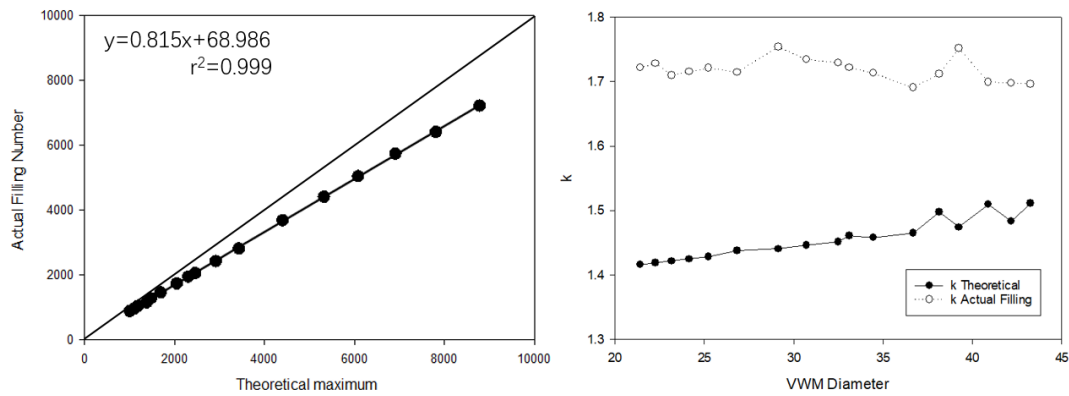
Figure 6-3. The mathematical relationship between the theoretical maximum and actual filling of VMWs. Left: there is a simple linear relationship with the theoretical and the actual (r2=0.999); Right: the theoretical and empirical k in Eq.5-9 and Eq.5-10.

6.1.1.2 Regular shaped objects

Fig 6-4 shows a VWD process for a cube object in the standard vessel. It can be seen that no VWMs could penetrate into the object inside. Compared to the computational modeling method, VWD does not require human visual inspection, which reduces human error from the source. Meanwhile, it is free of validation only if the diameter of VWM is larger than the maximal gap of adjacent points.
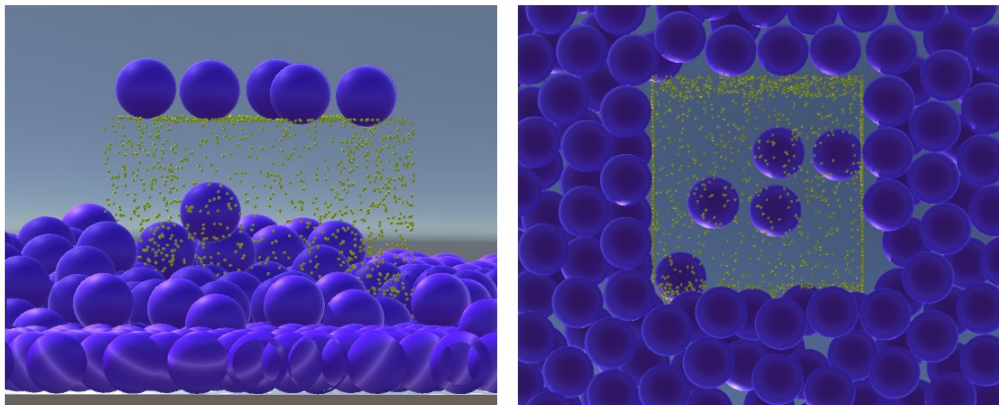
Figure 6-4. A VWD process for a cube, side length is 100, VWM diameter is 29.136. Left is from front perspective; Right is from bottom perspective.

Cube, cylinder, and sphere were selected to be tested in the standard vessel. Fig.6-5 shows that the VWMs filling had a similar response comparing to filling into the vast vessel.

Due to the performance restriction on computer, VWMs with six different diameters were selected and the VWM with a diameter less than 29.136 did not have a smooth simulation (FPS>1) in this study. Therefore, it was unable to do VWD process using VWMs where the diameter was smaller than 29.136.
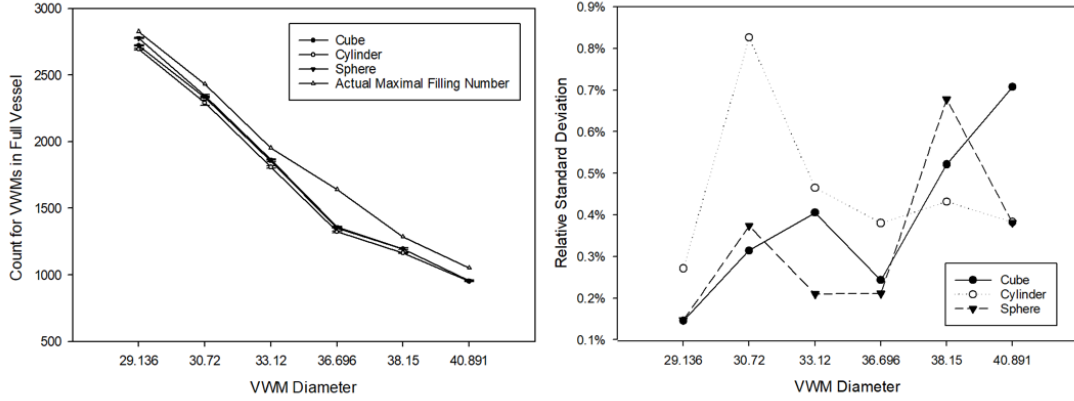
Figure 6-5. The filling using VWMs for cube (side length=100), cylinder (diameter=100, height=200), and sphere (diameter=100). Left: The quantity difference between the actual maximal filling number and the filling number with standard deviation; Right: The relative standard deviation for each filling was repeated five times.

At first glance, the performed data appeared incredible. Fig.6-6 shows the huge difference between VWD estimation and the true volume, which indicated many more VWMs were evacuated by the point cloud inside, compared to the theoretical number. With the shrink of VWM diameter, this difference decreases dramatically as well. Based on equations 9 and 10, it had to apply a new additional coefficient, j, to calibrate the VWD volume to true volume by the following equations, where V_{ture} is the true volume of object; V_{VWD} is the object volume derived by VWD process; j is an additional coefficient for calibration by force; k is the coefficient of volume calibration from VWM sphere volume to VWM volume (as a volume placeholder); V_{vessel} is the volume of vessel; n' is the actually filling number of VWMs; and v_s is the sphere volume of a VWM.

$$j = \frac{V_{ture}}{V_{VWD}} \tag{6-1}$$

$$k = j \frac{V_{vessel}}{n' v_s}. \tag{6-2}$$

From another aspect, j is an indictor to evaluate the accuracy of VWD estimation. On the condition of $j = 1$, the evacuated VWMs precisely represented the volume of the detected object. Fig.15 (right) indicates an obvious negative correlation between VWM diameter and j. Therefore, it could assume that, when the VWMs diameter reaches small enough, would lead to j so close to 1 as to be neglected. From Fig.6-6 (left), it was also known that the response of VWM is different according to shapes.
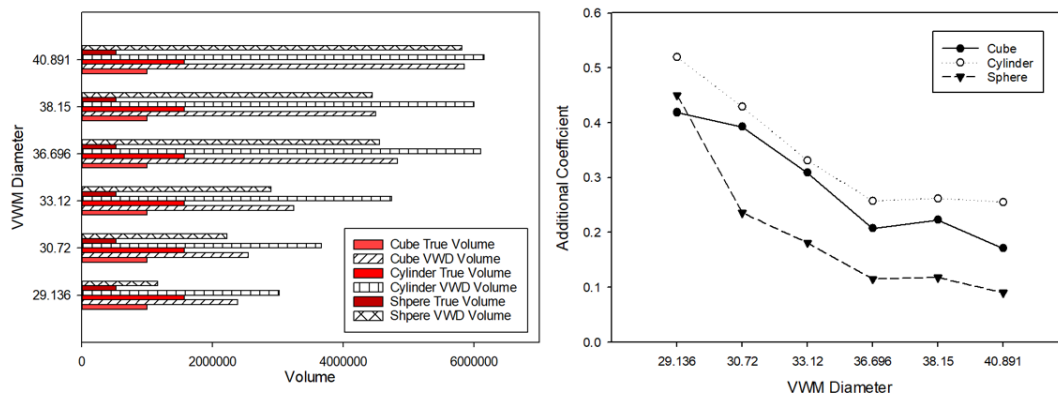
Figure 6-6. The VWD volume estimation for three regular shape objects with VWMs in six different diameters; Left: The quantitative difference between VWD volume and true volume; Right: An additional coefficient using true volume dividing VWD volume.

6.1.1.3 Artificial stems

With the knowledge in the previous section 6.1.1.1 and 6.1.1.2, the VWD process could be applied on the point clouds of artificial stems. As shown in Fig. 6-7 and Fig. 6-8, the standard vessel was not good for a VWD process because the diameter of the tree is close to the VWD diameter. According to the experience from regular shape objects. According to the scale effect (in 6.1.1.4(iii)), relatively smaller VWD diameter would be helpful in estimation accuracy. Therefore, due to computer performance (in 6.1.1.4(ii)), VWD diameter was assigned to 10, and meanwhile shrank the outliner of the vessel. Figures 6.7 and Fig.6-8 are comparisons of two settings. The point clouds are the same in two VGEs.

For artificial stems, full VWD workflow was applied. The additional coefficient j (in Eq.6-1 and Eq.6-2) was calculated according to the result of "stem" point cloud. Then j was used to calibrate VWD estimation for the "stem with branches" point cloud.
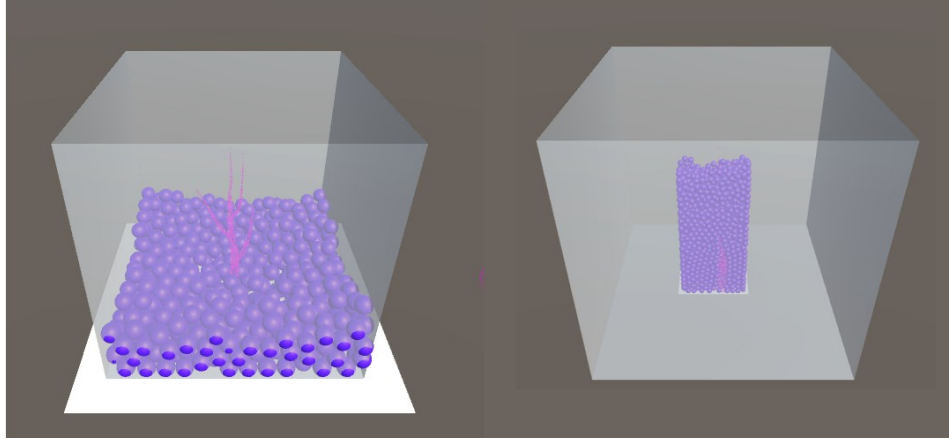
Figure 6-7. The VWD process for the artificial stem. Left: The artificial point cloud in the standard cube vessel (side length = 400) and VWMs (diameter=29.136); Right: The artificial point cloud in a special cuboid (bottom length=120, bottom width=60, height=300) and VWMs(diameter=10).
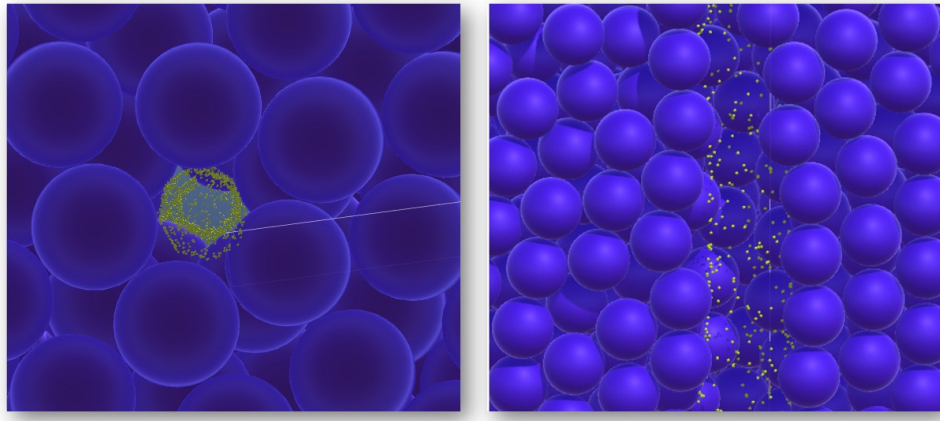
Figure 6-8. Scale effect of VWMs. Left: VWMs (diameter=29.136) collide with the artificial point cloud (bottom view); Right: VWMs (diameter=10) collide with the same point cloud (front view).

Table 6-1 is the experiment record. The standard deviation maintained a similar performance for VWMs filling comparing to fillings 4.1 and 4.2. From the "stem" point cloud, the empirical j value was 0.573. Then j was used to calibrate the volume for the "stem with branches" point cloud. The VWD volume was determined as 29,636 (overestimation at 6.0%), where the true volume is 27,946 and the QSM derived volume is

26,155 (Tab.2, mean value, repeated 11 times, underestimation at 6.4%).

Table 6-1. VWD estimation for artificial stems. Vessel refers to the vast vessel (bottom length=120, bottom width=60, height=300); stem refers to the resampled point cloud of the stem model; stem with branches refers to the resampled point cloud of the stem with branches model; R.1 to R.5 refers to the five repeated VWD processes; STDEV refers to the standard deviation; AVG refers to the average value of R.1 to R.5; DIFF refers to the replacement number of VWMs comparing with the actual filing number of vast vessel; True V refers to the mesh volume of tree models; VWD V refers to the volume derived from VWD process; adjusted VWD V refers to the final result of VWD measuring.

	R.1	R.2	R.3	R.4	R.5	STDEV	AVG	DIFF	VWD V	True V	Adjusted VWD V
Vessel	2294	2305	2294	2298	2295	4.66	2297				
Stem	2259	2256	2247	2250	2252	4.76	2253	44	41376	23709	
Stem with Branches	2244	2237	2247	2241	2243	3.71	2242	55	51720	27946	29636

6.1.1.4 Discussion

(i) The art of thinking

Human beings have been learning the law and experience from nature since ancient times and have known how to utilize physical rules to measure objects. The phenomenon of water displacement was discovered independently as Archimedes in Greek and in the story of Cao Chong weighing the elephant in China. Measuring methods connect certain features of the measuring target clearly with certain physical parameters. In a measuring method, no mathematical processes are employed to make predictions. Learned from the water displacement method in reality, the virtual water displacement method was developed successfully, which was aiming to directly measure the LiDAR point cloud for stem volume.

(ii) Computer performance and the VWD Feasibility in the future

As shown in this study, compared to processing data directly, the simulating of measuring instruments was complicated. The quantity of points for a real tree may vary from 100,000 to 10,000,000, which far exceeds current computer performance, both in software and hardware. In a VWD process, both VWMs and tree points consume the

resources of the rigid body. However, the quantity of the rigid body is limited by the physical engine, PhysX SDK 3.4. The maximum support of rigid bodies is 65,535 [166]. Compared to the regular quantity of points in a large tree point cloud. It could not have enough rigid bodies to replace the original points in a virtual space. Furthermore, compared to points in point clouds, VWMs consume much more rigid bodies in order to fill the vessel. Thus, the current physical engine cannot support a VWD process at a large tree level.

In addition to the limitation in software, physical simulation depends on computer hardware as well. It was useful to know how many rigid bodies could be supported by the desktop computer in this study. The quantity of VWMs had a negative relationship with the VWM diameter. For the consideration of computer performance, it was intended to use fewer VWMs. However, the VWM diameter was proved to relate to the accuracy positively. Therefore, it had to perform VDM processes using small VWMs.

In order to find a favorable compromise with this contradiction, frames per second (FPS) was used as the criterion to find the smallest VWMs. VWMs with different diameters was filled in VGEs. During those tests, if the FPS<1 in the current VWD process, the test stopped further attempts to seek a potential smaller diameter of VWMs. For the vast vessel (no tree points), the smallest VWM diameter was 21.416; for the vessel with tree points, the smallest VWM diameter was 29.136. The graphics card was NVIDIA GeForce GT 640 (2012), with a FP32 (float) performance of 693 GFLOPS. Comparing to this, the current high-end graphics card, NVIDIA GeForce RTX 2080Ti (2019), has a 13450 GFLOPS in FP32 (float) and is ~19 times faster. The maximal VWMs simultaneously existed in our VGE was 7227. It was assumed that there is a simple linear relationship with FP32 and the number of rigid body support. Then it could have ~130,000 (65535) rigid bodies to be allocated if the NVIDIA GeForce RTX 2080Ti was used. Compared with the date of manufacture of those two graphics cards, which are 2012 and 2019. It could roughly foresee that, the hardware would like to support VWMs and tree points at the quantity at 10,000,000 within the next ten years. Meanwhile, it is expecting the improvement of the PhysX SDK as well.

(iii) Scale effect for VWMs:

The scale effect was a virtual phenomenon that was discovered in the VWD processes when testing the VWD measuring with regular shape objects. The scale in the scale effect referred to a ratio between volumes of VWMs and volumes of measuring targets. Especially for trees, it is important to pinpoint that the volumes of VWMs should compare with volumes of stem disks (in Fig.5), not the volume of the whole tree. In general, a smaller scale related to higher accuracy of VWD measuring process. Therefore, it is recommended to use the VWMs with the smallest diameter to fill the vessel. Meanwhile, the diameter of VWMs depends on computer performance.

The scale effect is shown in Fig.6-6. The left figure in Fig.6-6 records VWD measures for three regular shape objects using VWMs with six different diameters. With the decreasing of VWMs diameters, from 40.891 to 29.136, the volumes from VWD measuring were closer to the true volume. An additional coefficient was used in the right figure in Fig.6-6 to indicate the difference between true volume and VWD volume. The value of 1 indicates that the VWD volumes would exactly equal to the true volume. Combing information of two graphs, for the tree regular objects, it was predicted that the diameter of VWMs at about 10 to 15 could let the additional coefficient close to 1. According to this knowledge, the smallest diameter of VWMs should be preferred as a priority.

Figure.6-9 shows the source of the scale effect. In a virtual space, each VWM is attracted by gravity. Moreover, the motion of a VWM is affected by its adjusting VWMs. Duo to the simulating of energy decay in PhysX, each VWM keeps motion for certain times. The green line in Fig.6-9 demonstrates the random motion of the green VWM. One consequence of this random motion is evaluating more VWMs out of the vessel. The volume of the green VWM is too close to the grey mearing target, each evaluated VWMs has a great influence on the final displaced volume. The effective way to reduce this influence is to shark the VWMs diameters, such as the red VWM shown in Fig.6-9. Similar to the green VWM, the red VWM also has a chance to evaluate VWMs out of the vessel. However, due to the significant volume difference between the red VWM and the measuring target. The unexpected evaluated VWMs have a minor influence on the overall volume.
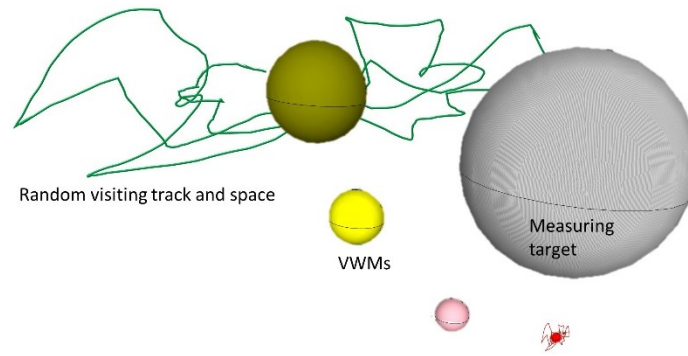
Figure 6-9. Demonstration graph for scale effect and random movement of VWMs in micrographic scale.

6.1.2 Results and discussion of stage two, displacement using few VWMs

6.1.2.1 Test for the flood area mechanism with regular shape objects

One VWM was released to test the flood area mechanism. In this test, the volume of the cube was measured. The parameters impacted the simulation process, i.e., the diameter of VWM and running time. As expected, no human inspection and intervention were required during this simulation. A simple termination condition, i.e., the running time of simulation, was applied, which was significantly different from conventional modeling methods. More interestingly, an absolute true volume of the cube, $V_{absolute}$, was generated even before the VWM was released. That was because the only variable in this physical scenario, i.e., the geolocation of the VWM, had no ability to break the completeness of the cube. What it could be affected was the efficiency of the simulation. V_{flood} was used to represent the instant volume flood area. With the flying of time, the difference between V_{flood} and $V_{absolute}$ diminished into an ultra-small scale. Figure.6-10 shows the sequence of VWM footprints shortly after the simulation started.
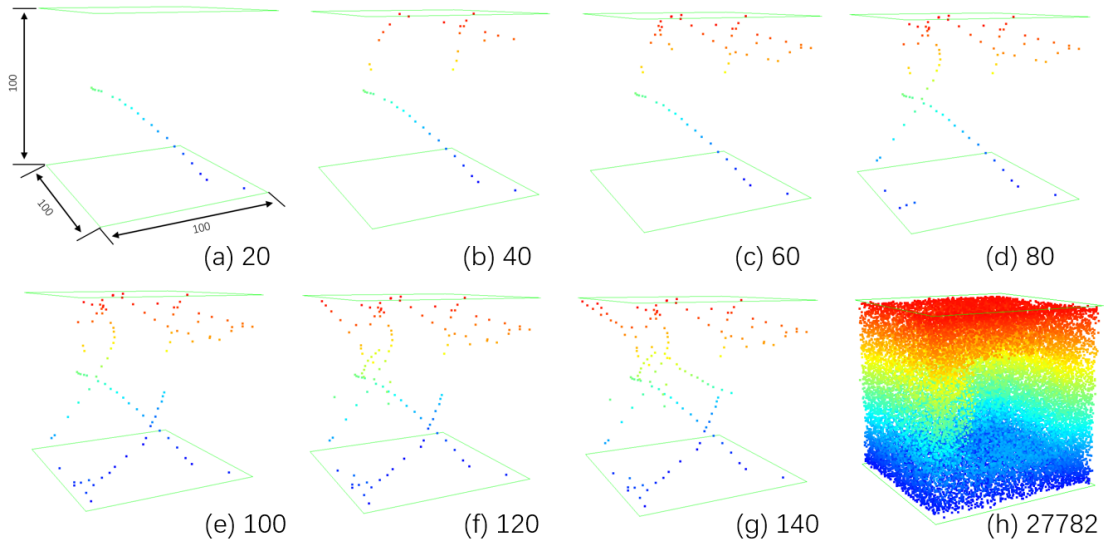
Figure 6-10. The footprint recording of a VWM; (a) to (h) are arranged ascending by the application running time; the number is the total generated footprints.

This simulation ended with 1,438,814 footprints generated. However, some of voxels were visited by the VWM many times, and others were not visited at all. There were 1,000,000 voxels in total, and 561,025 of them were visited in the end. The re-visiting rate, 2.56, was calculated by footprints divided by the number of visited voxels. This re-visiting rate indicated the efficiency of simulation and no ability to affect $V_{absolute}$ also. Due to the VWM was attracted by a random changing gravity field, re-visiting the same voxels would happen naturally and could not be avoided. Therefore, a compensatory strategy was employed. That was the buffering.

By applying buffering to raw footprints, there was no need to wait for a full visit of all voxels in the vessel. According to equation 5-11, an appropriate buffer would extend the flood area of each footprint significantly. Fig.6-11 shows the comparing of the measuring result of the cube using different buffering length. Without buffering, it could not visually distinguish the cube from the raw footprint, as shown in Fig.6-11(a). After applying buffering with 1 unit, as shown in Fig.6-11(b), the cube was extracted clearly from raw footprints. However, there were speckles on the wall area, indicating the un-visited voxels by the VWM even with buffer applied. From another perspective, compared to the inner areas, the wall areas of the vessel had less opportunity to be visited.

Figure 6-11(c) and (d) shows different approaches to further process the result in Fig.6-11(b). By applying an outliner filter, as shown in Fig.6-11(c), the redundant area of the cube was removed. Otherwise, this redundant area could be achieved by extending the buffering length from 1 to 2. However, as shown in Fig 6-11(d), over buffering would occupy the voxels belong to the measuring target and led to an underestimation of the cube volume.
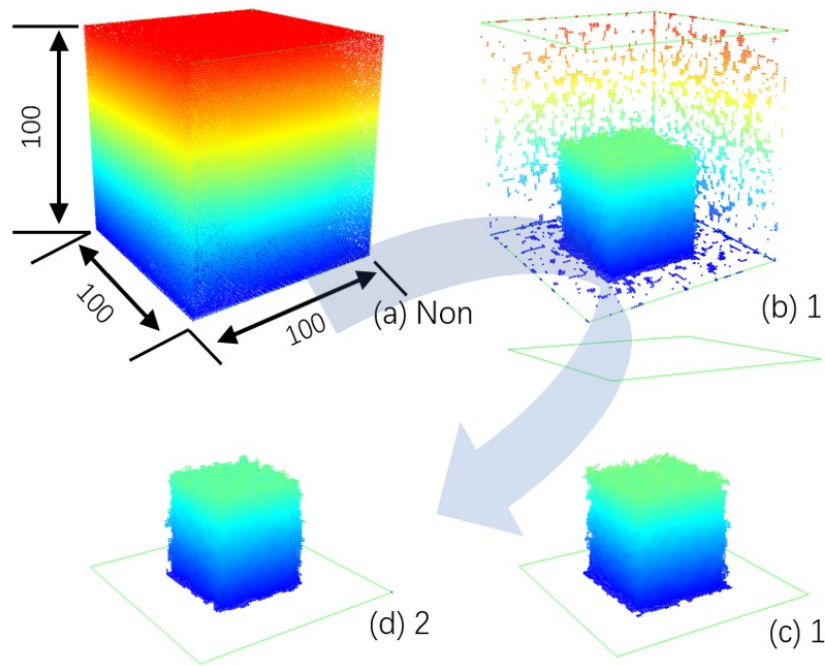
Figure 6-11. The comparing of the measuring result of the cube using different voxel buffering; (a) no buffering; (b) buffered with 1 unit; (c) buffered with 1 unit and outliners were removed; (d) buffered with 2 units.

In the development of stage one of VWD, it was observed that VWMs responded differently to the three regular shape objects. On the contrary, the flood area mechanism in this stage two showed insensitive to shapes. Table 6-2 shows the measuring results for the cube, sphere, and cylinder objects. Compared to Fig.6-6, the flood area was much more stable than the original VWD mechanism in stage one. The most likely reason was that the simulation of interaction among VWMs was canceled in this stage. Consequently, the source of error was limited.

Table 6-2. Results for the VWD process using flood area mechanism on three regular shaped objects.

Objects	True volume	VWD volume	Relative difference	Footprints	Buffering distance
Cube	125,000	132,845	+6.28%	246,540	1
Sphere	64,043	66,946	+4.53%	436,519	1
Cylinder	193,129	208,673	+8.05%	323,855	1

Mean: +6.29%

6.1.2.2 Artificial stems results

After the feasibility of the flood area mechanism was proved. The point clouds of artificial stems were able to be processed. Figure 6-12 shows the simulations result and the raw footprints of this simulation using the "stem" point cloud. This figure was organized using the form of Eq.5-11, i.e., the equation of the primary mechanism of flood area mechanism. In plain language, this mechanism was purring water into a swimming pool, with trees inside, until full of water.
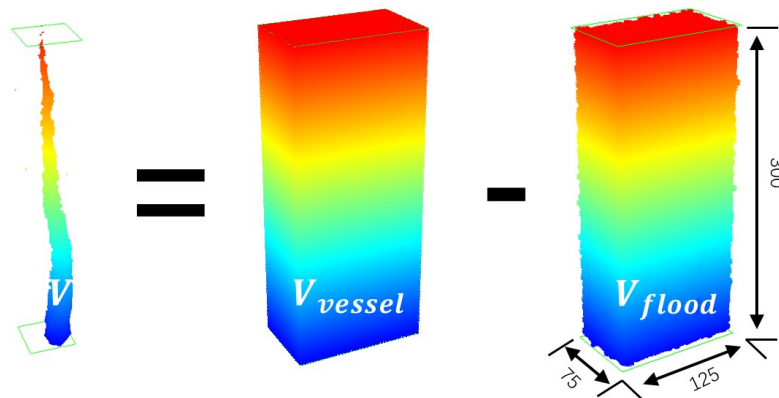
Figure 6-12. The visual demonstration of Eq.5-11 using the result of a VWD processing on the "stem" point cloud.

Figure 6-13 and Table 6-3 shows the stem volume measured using flood area mechanism for the "stem" point cloud and the "stem with branches" point cloud. Before the simulation began, the quantity of voxels in the virtual space (vessel) was determined as 2,812,500. In order to improve the measuring accuracy to the maximum degree, the simulations were processed as long as possible. As a result, the raw footprints recorded in both simulations were much greater than the quantity of voxels in the virtual space at a few times more.

(a)   (b)   (c)   (d)
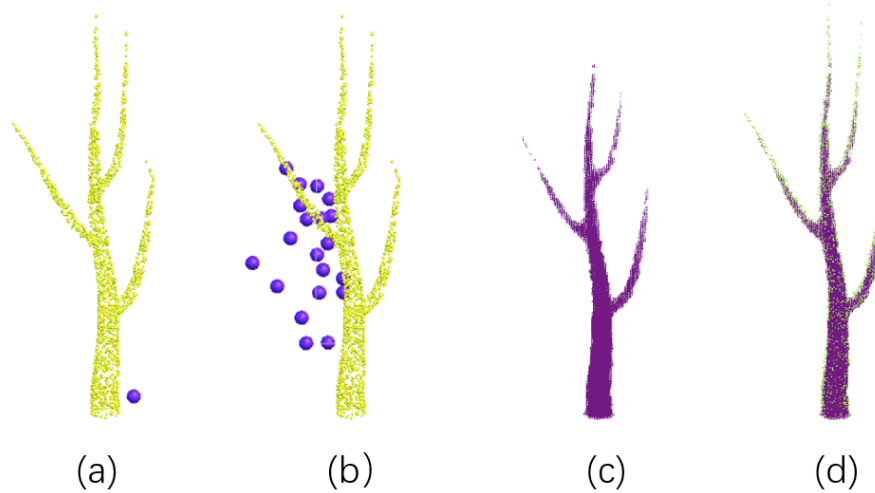
Figure 6-13. Measuring the "stem with branches" point cloud using flood area mechanism; (a) the measuring process using single VWM; (b) the measuring process using multiple VWMs; (c) the measuring result; (d) overlaying of VWD result and the original point cloud.

However, the visit of all voxels in the virtual space using VMWs was tough to be achieved. Instead of a full visit, buffering was also an approach to extend the ability to occupy voxels for VWMs. For example, a footprint could occupy a voxel under normal circumstances. After buffered with 3 units, for the "stem" point cloud, a raw footprint occupied the surrounding 343 voxels. In total, 2,428,355,965 voxels were marked as visited voxels. It was about 863 times greater than the quantity of voxels in the virtual space. A similar calculation for the "stem with branches" point cloud was also analyzed. After buffered with 2 units, each raw footprint occupied 125 voxels. In total, 1,1148,874,125 voxels were marked as visited voxels. It was about 408 times greater than the quantity of voxels in the virtual space. Compared to the results of regular shape objects, there were only 2.86% and 1.84% overestimation in those two point clouds, respectively. The high re-visiting rate was the reason for the improvement of accuracy.

Table 6-3. The result for VWD process on two artificial stems.

Objects	Ture Volume	VWD Volume	Relative Difference	Footprints	Buffering Distance
Stem	23,709	24,344	+2.68%	7,079,755	3
Branches	27,946	28,459	+1.84%	9,190,993	2

Mean: +2.26%

6.1.2.3 Discussion: approaching true values by the accumulation of time

The repeated measurement was a usual approach to enhance the accuracy in a conventional measuring process [27]. For example, the manual measurement errors in a DBH measuring process could be diminished using repeated measurements. Compared to the measuring process in reality, no repeated measurement was required in the CVM process. As previously stated (in 5.1.2.6), the absolute true value of the measuring target was generated at the moment, when the virtual space was established. Specifically, for this flood area mechanism, with the accumulated running time, the VWD instant volume V_{flood} was approaching to $V_{absolute}$. Therefore, the repeated measurement was not necessary to be applied. The improvement of accuracy was provided by increasing the simulation time.

The raw footprint record of the cube object (Fig.6-11) was analyzed. The increment of the unique voxels detected by VWMs is shown in Fig. 6-14 (left). It was observed that the increment decreased after the fast uprising in the initial stage. The differential increments of unique voxels for every 0.1% of the total generated frames are presented in Fig.6-14 (right). It was obvious that the differential increments of unique voxels always decreased with the accumulated time. This indicated that the VWMs had less possibility to detect new un-visited voxels with the accumulated time. Finally, the VWMs would achieve a full visit for every accessible area, if the running time was long enough.
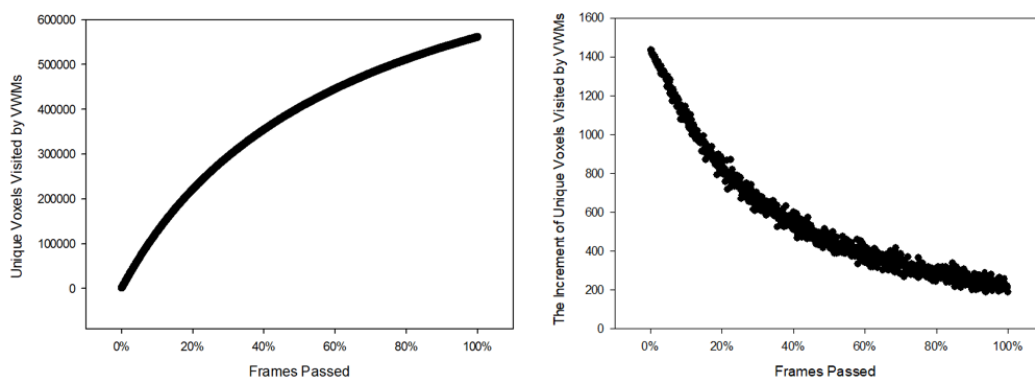
Figure 6-14. The unique voxels detected by VWMs with the increasing of running time for the cube object.

6.2 Results and discussion for sunlight analysis methods

6.2.1 Results and discussion of stage one, sunlight analysis for single tree in stand-alone condition

6.2.1.1 Single tree modeling

Figure.6-15 shows the TLS scanning and QSM modeling results. The impact on data quality concentrated on the QSM modeling process. As shown in Fig.6-15(a), there are a green tree and seven white trees in the sample plot. The original plan was to apply QSM modeling in all these eight trees. However, due to the obstacles and the lack of one scanning position, only one tree (the green tree) was successfully modeled. Fig.6-15(b) is a photo of the green tree. Fig.6-15(c) showed the point cloud after data pre-processing. Figure 3(d) showed the QSM model after manual correction. The measured tree parameters are as the following: the tree height is 12.81m; the DBH is 24.60 cm; the stem volume from the QSM model is 0.52 m^3. It is noticeable that manually modification for the obvious modeling error on the main stem part was applied using another 3D model tool, Blender [186]. Thus, the stem volume of the tree model, shown in Fig.3(d), has a minor difference with the original QSM model. The area of stem surface was re-calculated.
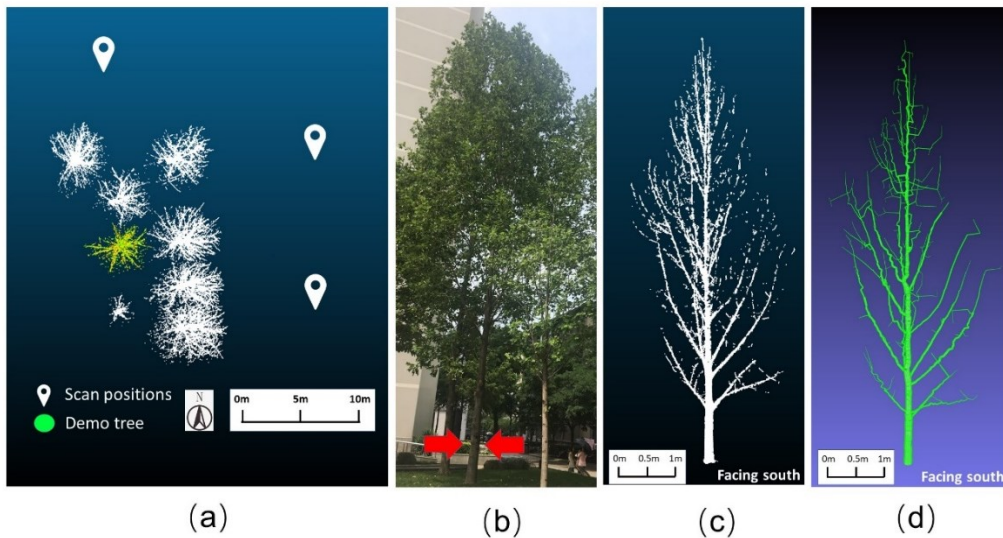
Figure 6-15. TLS scanning and QSM modeling; (a) layout of TLS scanning, the demo tree is in the center; (b) photo of the target tree (photograph taken by Prof. Baitian Wang in Beijing Forestry

University); (c) the point cloud of the demo tree; (d) The QSM model with manual correction on the main stem of the demo tree.

6.2.1.2 Single tree light condition

Figure 6-16 shows the results of sunlight analysis on the demo tree model. The result was outputted as a 3D mesh with an additional attribute, i.e., the color. Eight different colors are used to represent different daylight duration on the corresponding parts of the tree. The original tree model had 31706 faces (organized using triangles). For an original face, e.g., the generally cyan-blue face in Fig.4(f), it would have different exposure duration to the direct illustrated sunlight. Therefore, each original face would be divided into a few new faces, unless it could not receive virtual sunlight during the entire simulation (facing north). Specifically, for the demo tree in this study, the number of faces (triangles) increased from 31706 to 899346 after sunlight analysis. Figure 4(a-d) are the views of the result from different directions. Figure 4(e-f) are partially magnified views of the result on different scales.
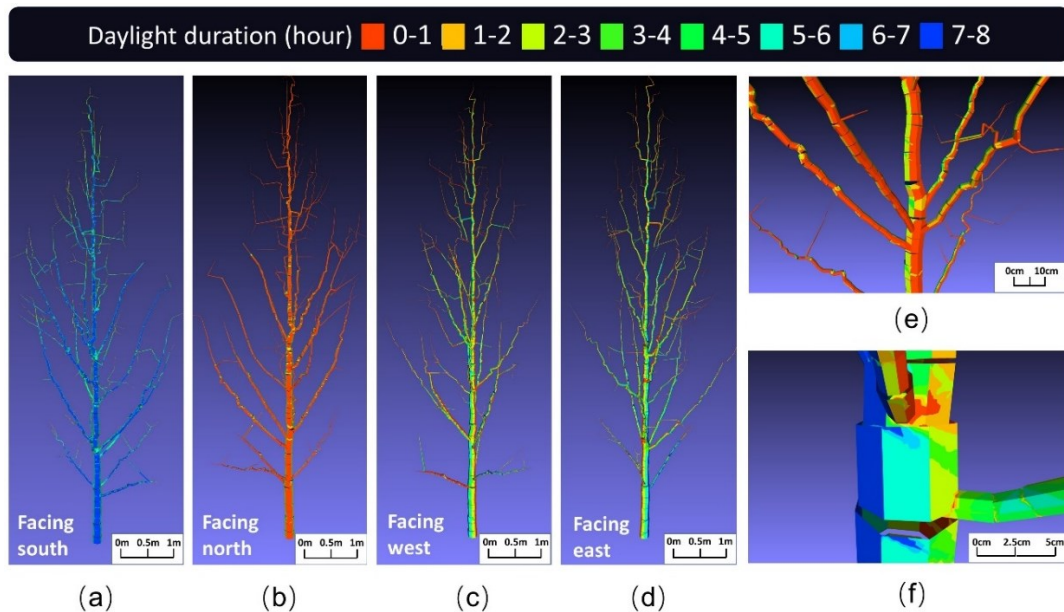
Figure 6-16. The results of sunlight analysis on the single tree QSM model; (a-d) views of the result from different directions; (e) partial magnified view of the result; (f) detailed view on the joint area of the tree model.

Sunshine_pro_2019 could not provide any statistical information. It only stored the

exposed duration information as the color attribute in obj file. An application using C# was developed to read information directly in obj file. After then, the information was imported into MATLAB for further statistical procedures. Figure.6-17 shows the statistical result of the sunlight analysis for the whole tree model.
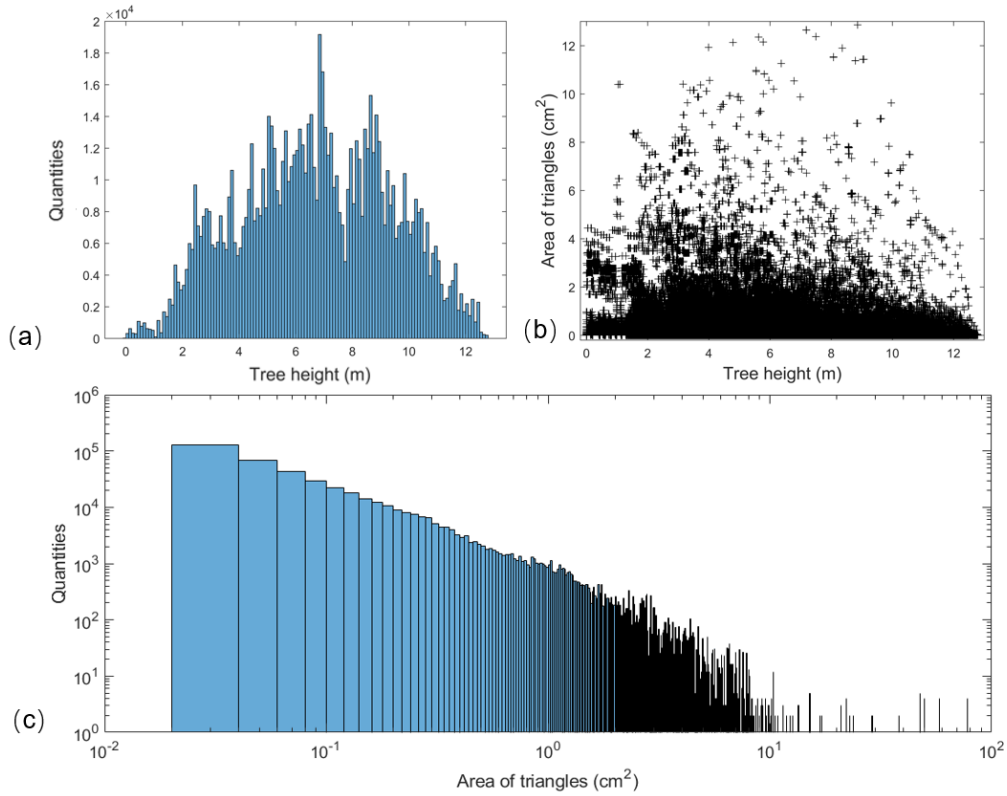
Figure 6-17. Statistical result of the sunlight analysis for the whole tree model; (a) the distribution of triangles' quantities in tree height; (b) the distribution of the area of triangles in tree height; (c) The distribution of triangles' quantities in triangles' area.

Figure.6-18 shows the distribution of the area of faces (triangles) in tree height classified by sunlight duration. Most importantly, Fig.6-18(i) shows that the locations of triangles concentrating in the lower position on the tree compared to other daylight groups (a-h). The relatively large percentage of large triangles in Fig.6-18(i) also indicates that those triangles are on the surface of main stems.
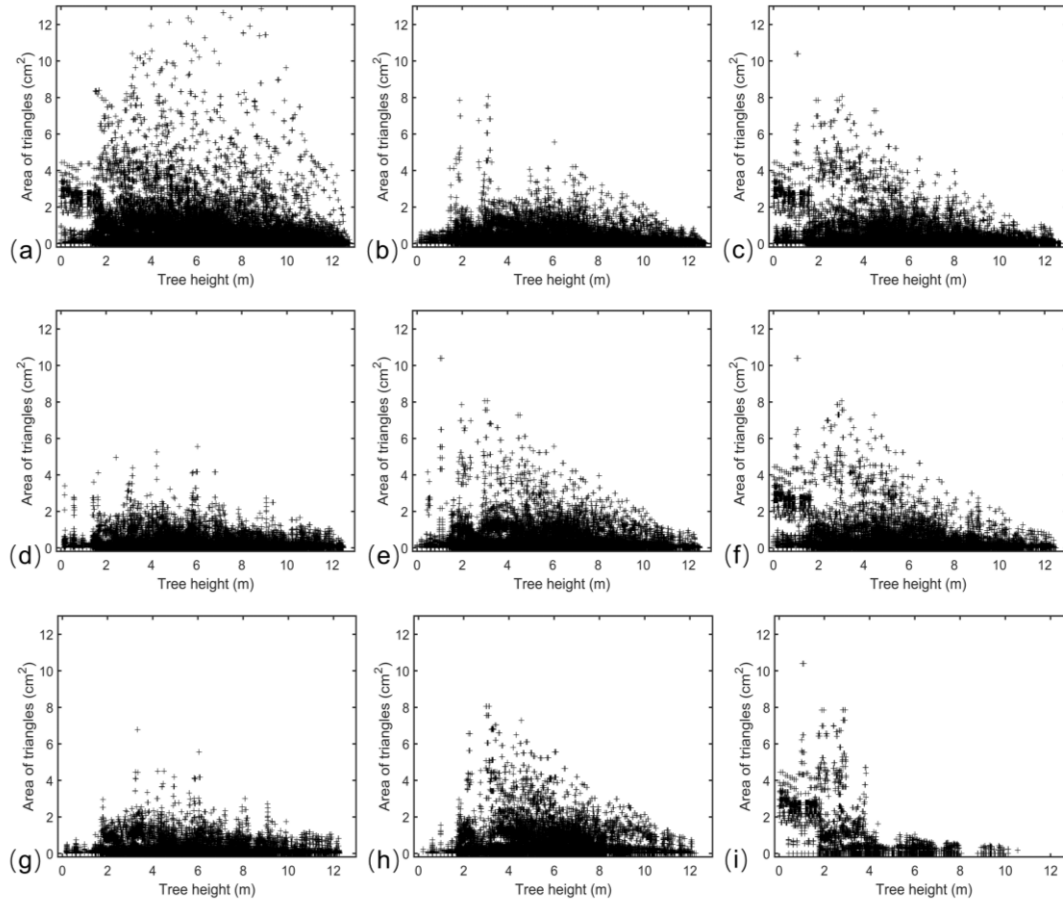
Figure 6-18. The distribution of the area of faces (triangles) in tree height classified by sunlight duration.

(a)-(h): daylight duration from 0-1 hour to 7-8 hours; (i) 8 hours, full expose under the sunlight.

Table.6-4 shows the final result obtained from this study. It shows the temporal and spatial distribution of solar energy (via direct irradiation) on a single tree in general. Compared to the 3D result mesh, detailed information on a specific face is lost. To sum up, sunlight analysis provides the result with two forms. The first one is the 3D result mesh, which contains full information. The second one is statistical results from the 3D result mesh, which is fitting to be cited in papers.

Table.6-4 shows that there are only 4.34% of the tree structure exposed in the sunlight during the whole day. The most interesting part is, there are 35.87% of the tree structures are covered with sunlight in less than one hour. It was assumed to apply a sunlight analysis on a regularly shaped object, e.g., a cube, which has five square faces (excluding the bottom), and one face heads to the geographical (true) north. For this cube, the sunlight

duration of less than one hour would be exactly at 20%, which differed to 35.87 % significantly. This difference indicates that the shading between tree structures have a significant influence on the duration of daylight.

Table 6-4. Statistical table of daylight duration classified by hours.

Duration of daylight (hour)	0-1	1-2	2-3	3-4	4-5	5-6	6-7	7-8	8	Total
Area (m²)	5.16	1.50	1.60	0.91	1.25	1.21	0.67	1.45	0.62	14.38
[1]Relative area of faces (triangles)	35.87%	10.46%	11.12%	6.34%	8.72%	8.41%	4.65%	10.09%	4.34% (α)	
[2]Relative quantities of faces (triangles)	22.46%	19.32%	17.47%	12.60%	11.01%	7.18%	5.41%	3.92%	0.63%	
Ratio of 1/2	1.60	0.54	0.64	0.50	0.79	1.17	0.86	2.57	6.89 (β)	

α and β are two potential indicators for the intensity of the competitive growth racing between different branches.

6.2.1.3 Discussion

(i) A new indicator for single tree light condition

It is proposed that the outputs of sunlight analysis as a potential indicator for single tree light conditions that can utilize in NFI. Because it is not site- and tree- specific. This indicator has two mathematic forms, i.e., absolute and relative values. As shown in Tab.6-4, the absolute indicator consists of the areas of the duration of daylight in each group. The relative indicator consists of the relative areas of the duration of daylight in each group. The relative indicator makes it easy to compare between different trees ignoring the differences in stem volume (tree scales).

(ii) Findings in the sunlight analysis

The exposed duration for tree surfaces depends both on the surface orientation and shades from obstacles. The effect of orientation and shades can be quantitatively determined by sunlight analysis. For the demo tree, the percentage of full lighting in the tree surfaces was virtually measured to be 4.34% (marked "α" in Tab.6-4). The distributions of the area of faces (triangles) in tree height are classified by sunlight duration in Fig. 6. The faces of full exposure are recorded in Fig.6-18(i), the data distribution is significantly different from the other graphs in Fig.6-18. Those faces in Fig.6-18(i) are concentrated in the lower height of the tree with a large face area. Considering the images in Fig.6-16(a-d),

it was noticed that the lower height of the tree model referred to the main stem with few branches. For the first time, two small branches are in the height about 1.6m, then three main branches are in the height about 2.8m. Increasing by height, more branches appear in the tree model, which project shades to other tree structures. Thus, an original face in the upper height of tree are much likely to be split into smaller faces (shown in Fig.6-16(f)). There is little chance for large area face of full exposure in the upper height of tree and little chance for a continuous distribution of faces with the same exposure duration.

The ratio between relative area of faces and relative quantities of faces calculated as "Ratio of 1/2" (R1/2) in Tab.6-4. The representative ratio of R1/2, i.e., β (marked "β" in Tab.2), indicates this ratio in the group of 8 hours exposure. Smaller the value of R1/2 is, larger the dispersion degrees for faces (triangles) in spatial distribution is. Compared to other ratios in different time groups, the high value in β indicates that the average area for faces in this time group is larger than others. Regarding the graphs in Fig. 6-18(i) and Fig.6-16, The R1/2 ratio demonstrated that these faces with large areas are more likely distributed on lower stems. The α and β values might associate with the intensity of the competitive growth racing between different branches. For each individual branch in the tree, obtaining more solar energy is the essential survival competence. Smaller α value or larger β value indicates more intense competition between branches. In other words, due to the intense competition, branches on the upper stem may not obtain long-time irradiation. Therefore, only lower stem can expose to the sunlight continuously.

An extreme case was assumed that each branch in the demo tree is shaded by other branches. No branches in this tree can be illuminated by the sunlight with the duration of a full day. Meanwhile, the sunlight irradiation remains the same on lower stems. In this case, the value of α will decrease slightly. The value of β will increase significantly. This is because the relative quantities of faces (triangles) for full daylight will decrease at a large scale. Thus, compared to α, the value of β is more sensitive to the shading conditions of tree branches.

Another interesting finding is that 35.87% of the tree structures are covered with

sunlight in less than one hour. This discovery helps us to quantify the areas under weak light conditions. As a matter of fact, it could be also imagined that this stem model as a preliminary leaves model. In this illustration, each leaf attached to a branch in this stem model. Therefore, leaves could be visualized as a covering film on stem surface. Based on these assumptions, the percentage of 35.87% might be considered to be associated to the quantity of unirradiated leaves, which cannot be directly reached by sunlight.

(iii) Technical issues on sunlight analysis

Sunlight analysis is the original application method under the computational virtual measurement. Due to this feature, it is worth noticing some technical issues which may affair the analyzing results. The fundamental data support is LiDAR scanning in the forest field. As stated in section 3.1, the data quality has a great influence on the tree model. There are two ways to improve the tree modeling process. One way is through comprehensive scanning for trees, which should be considered as a priority. If an additional scanning position could be installed, more trees would be available for QSM modeling. The second way is through predicting methods [187] and manual corrections. The predicting method in the tree modeling process can be applied, in case there is no possibility to enrich scanning in the forest field. However, the prediction of tree parts is not recommended due to that there is no reliable method to validate the predictions. Therefore, the manual correction of tree model with visual inspection is helpful.

During the sunlight analysis, one should also be cautious about scaling the original tree model because the smallest input for sample point spacing Sunshine_pro_2019 is 0.5m. Therefore, the tree model was magnified 30 times on each side length. Consequently, the smallest equivalent sample point spacing for the original tree model was 1.67 cm. In case of blank value, it is necessary to perform a visual inspection of the result. The acceptable requirement is that all visible parts of the tree model were granted a color attribute. Besides visual inspections, directly check the plain text in the 3D result mesh is another method to make a confirmation. Moreover, 2D flat should not exist in the tree model. Because Sunshine_pro_2019 was designed to analyze 3D building. A 2D flat might cause duplicate rendering.

6.2.2 Results and discussion of stage two, sunlight analysis for single tree in stand-alone condition

6.2.2.1 Virtual sample plot

Figure.6-19 shows the established VSP. This VSP consisted of eight tree models made using voxel approach. These eight tree models had 2460262 lines and 1813966 faces in total, which was a challenge for computer performance. In addition, T26 was able to be modeled using QSM approach, as shown on the left side of Fig.6-19. In one sunlight analysis process, it was allowed that only one model of T26 existed in the VSP. What needs to be noted here is that the perspective of Fig.6-19 is from north to south. This perspective can provide a clear view of T27 and T26. In this view, faces, which can be observed, could not be irradiated by virtual sunlight under any condition. Furthermore, as previously stated (in 5.2.3.2), T26 voxel model was replaced with T26 QSM model in order to compare the difference in results, which caused by the difference in modeling methods.
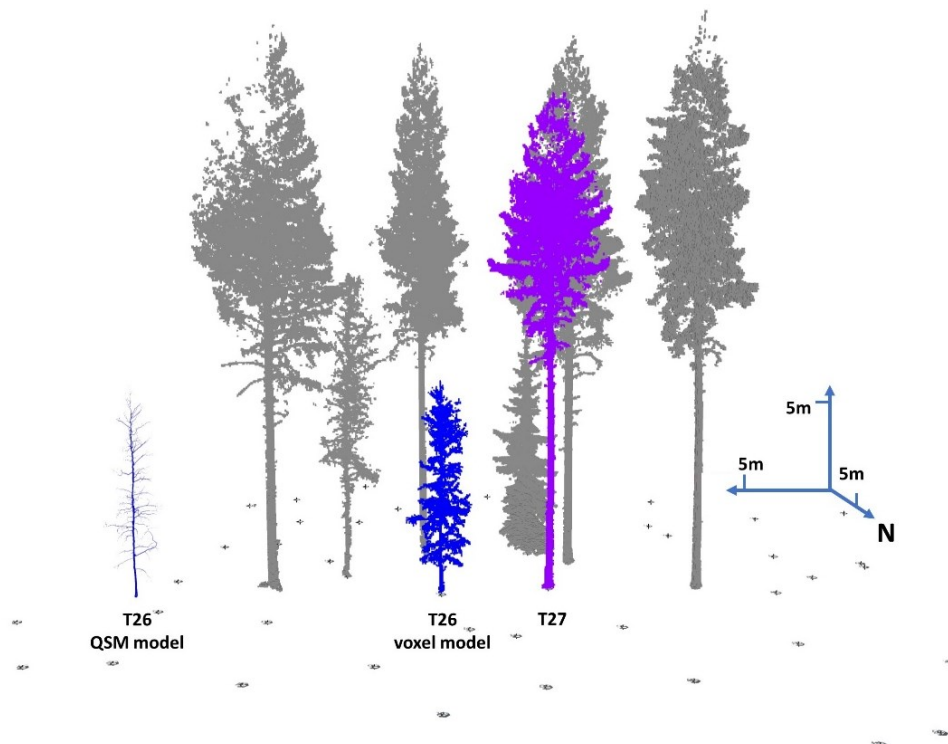
Figure 6-19. The established virtual sample plot.

6.2.2.2 Sunlight analysis in six scenarios

For each scenario (in 5.2.3.3), the light condition was virtually measured. Table 6-5 shows statistical information after the sunlight analysis in six scenarios. The same statistical processing in stage one of sunlight analysis applied. The areas of tree face (triangles in 3D result mesh) were added together, which had the same irradiation durations. The difference between voxel modeling and QSM modeling can be clearly observed in the 0-1 group. In scenario a, b, d, and e, T26 was made using voxel approach. A voxel had six faces in six directions. However, lots of faces located in T26 inside. Consequently, they were not the surface of trees and were unable to be irradiated at all times. Therefore, the area values in the 0-1 group were unusually large compared to the QSM model in scenario c and f. Thus, area values in the 0-1h group, for T26 voxel model, did not relate to its literal meaning, i.e., sunlight exposure during on tree surface. However, this technical drawback did not affect the study's aims. The following mathematical processing of difference would make compensations for this problem.

Table 6-5. Result of sunlight analysis on six scenes in the virtual sample plot.

| Scenes | Surface aera classified by irradiation duration (m²) | | | | | | | | | Triangles |
	0-1h	1-2h	2-3h	3-4h	4-5h	5-6h	6-7h	7-8h	8h	in mesh
a	501.91	20.99	16.14	21.07	6.78	4.66	3.35	3.50	1.68	2081198
b	77.63	6.15	5.33	7.36	2.60	1.87	1.52	1.57	0.97	758991
c	1.09	0.27	0.34	0.19	0.28	0.14	0.10	0.21	0.04	560072
d	527.98	22.70	15.75	8.59	2.46	1.10	1.08	0.35	0.08	1440302
e	83.60	8.59	6.48	2.78	1.54	1.16	0.82	0.01	0.00	537462
f	1.35	0.45	0.29	0.25	0.14	0.15	0.05	0.00	0.00	368727

Theoretically, there should be no changes in the area of tree surfaces. The changes should happen area of tree surfaces of specific exposure duration. By adding exposure duration in each group in each scenario in Fig.6-5, the overall changes in the area were 0 and 0.01m². It demonstrated the stability of the sunlight analysis method.

6.2.2.3 How neighborhood shadings affect light conditions of single trees

Table 6-6 shows decrements of light conditions for T27 and T26 due to shades caused by neighboring trees. These decrements were determined using the difference between the

light condition for a single tree in stand-alone condition and the light condition for a single tree in the VSP. In this way, the quantitative investigation of how much a single tree was influenced by the neighboring trees could be determined.

From the results, both T27 (scenario d-a) and T26 (scenarios e-d, f-c) had a significant loss of triangles in their 3D result mesh at ~30%. According to knowledge from stage one of sunlight analysis, the loss of triangles indicated that the virtual sunlight had more opportunities to be received by a large area on tree surfaces. That was because, a large area consumed few triangles in the mesh compared to scattered smaller areas. In addition, the larger areas intend to be located in the bottom area of trees. The loss of the overall quantity of triangles indicated the loss of solar energy approximately.

Tab.6-6 also shows detailed changes in T27 and T26 in each exposure duration group. Affected by shades from neighboring trees, both T27 and T26 had great losses on long exposure groups. The lost area in the long exposure group was added to the short exposure group. The magnitude of change can be observed clearly.

Table 6-6. The difference of light conditions for stand-alone condition and the full VSP.

Scenes	Surface aera classified by irradiation duration (㎡)									Loss of triangles
	0-1h	1-2h	2-3h	3-4h	4-5h	5-6h	6-7h	7-8h	8h	
d - a	26.07	1.71	-0.38	-12.49	-4.32	-3.56	-2.27	-3.15	-1.60	30.79%
e - d	5.98	2.44	1.14	-4.57	-1.05	-0.71	-0.69	-1.57	-0.97	29.19%
f - c	0.26	0.18	-0.06	0.06	-0.14	0.00	-0.04	-0.21	-0.04	34.16%

Table 6-7 is a mathematical transform of Tab.6-6. The absolute values in Tab.6-6 were translated to relative values for better readability. Figure.6-20 is the visualization of Tab.6-7. The reallocation of solar energy was clearly shown in this figure. The overall study aims in this thesis was to provide a novel forest measuring instrument. Therefore, the deeper meaning of these changes in ecology was not in the scope of this study. In other words, it provided an example of analyzing forest ecology form NFI data source.

Table 6-7. Area transferring between sunlight analysis on single trees and in full VSP; 100% refers to the total areas where the solar energy was changed; percentage (no sign) refers to receive area from other exposure groups; percentage (negative sign) refers to area loss.

Tree	Surface area classified by irradiation duration								
	0–1h	1–2h	2–3h	3–4h	4–5h	5–6h	6–7h	7–8h	8h
T27	93.86%	6.16%	-1.37%	-44.97%	-15.55%	-12.82%	-8.17%	-11.34%	-5.76%
T26 voxel	62.55%	25.52%	11.92%	-47.80%	-10.98%	-7.43%	-7.22%	-16.42%	-10.15%
T26 QSM	52.53%	36.36%	-12.12%	12.12%	-28.28%	0.00%	-8.08%	-42.42%	-8.08%
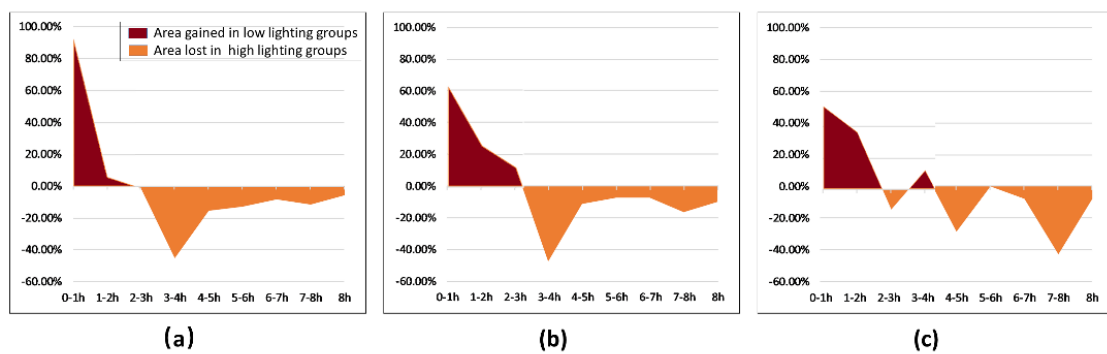
Figure 6-20. Area transferring between sunlight analysis on single tree and in full VSP; (a) T27 voxel model; (b) T26 voxel model; (c) T27 QSM model

6.2.2.4 Discussion: a linking with the conventional physical quantity, the power

The quantitively assessment of shading effect was expected to be beneficial to ecology studies. In ecology studies, thermophysical quantity is widely used. Therefore, in this section, it was tried to convert the standard output of sunlight analysis into classical thermophysical quantity.

In the above section, Tab.6-7 and Fig.6-20 shows us how the shift happened on tree surfaces because of shades. Meanwhile, the output of sunlight analysis provided temporal information as well as spatial information. Combined that information together, it was possible to calculate the exact energy loss for a single tree, due to the neighboring shades. Table.6-8 shows the exact energy loss for T27 and T26. The average power of direct radiation varied each day. In Tab.6-6, 0.11 kW/m² (61 N, 20 January) was applied as a

demonstration value. It was notable that, due to the problem of the voxel model, all information in the 0-1 group for each tree was excluded. All information for each tree in group 0-1 was excluded in determining the total radiant energy for a whole day. In addition, there were some limitations due to the processing software. Therefore, this conversion to the conventional physical quantity acted as proof of feasibility only.

Table 6-8. Assessment of the energy loss for single trees due to the neighborhood shading.

Trees		T27	T26 voxel	T26 QSM
Surface aera classified by irradiation duration (kWh)	0-1h	1.434	0.329	0.014
	1-2h	0.282	0.403	0.030
	2-3h	−0.105	0.314	−0.017
	3-4h	−4.809	−1.759	0.023
	4-5h	−2.138	−0.520	−0.069
	5-6h	−2.154	−0.430	0.000
	6-7h	−1.623	−0.493	−0.029
	7-8h	−2.599	−1.295	−0.173
	8h	−1.408	−0.854	−0.035
Loss of energy (kWh)		−13.12	−4.31	−0.26
Original energy (kWh)		28.95	10.97	0.71
Loss rate		45.32%	39.26%	35.80%

6.3 Conclusion of results and discussion

The format of results in two CVM implementations exhibited significant differences. The output of VWD method was a simple physical quantity, i.e., volume. This output achieved the consistency of stem volume in form, which is regularly collected by NFI field crews. Meanwhile, a fully developed VWD method could be regarded as a virtual measuring instrument in the future. Currently, the original VWD mechanism (stage one) was limited by computer performance. This technical limitation forced the employment of empirical processes. Fortunately, the flood area mechanism of VWD (stage two) solved this problem and proved the initial assumption of VWD and CVM. Therefore, it could be expected the potential performance of VWD when the technical limitation is released.

The output of sunlight analysis was not conventional indicators currently collected by NFI. The output was a spatial distribution of solar energy on tree surfaces. Compared to conventional ecological studies, some factors, e.g., foliage, were not included in sunlight analysis. That was because the full workflow of sunlight analysis should compound the general methodology of CVM. As stated already, there was no effective method to validate leaf models using raw point clouds. What needed to be emphasized was that CVM was a measuring procedure fundamentally. At least, modeling steps in a CVM procedure should be validated themselves without additional data sources. By this means, a CVM implementation can be regarded literately as a virtual meeting instrument without adding additional workloads. Subsequently, it can contribute to NFI by providing a standard protocol.

Chapter Seven

Conclusion and Outlook

7.1 CVM implementations

The successful development of these two CVM implementations, i.e., VWD and sunlight analysis, confirmed the overall concept and the feasibility of CVM. Each of these implementations was developed to measure a specific tree parameter using physical simulation in virtual space.

The first implementation was the VWD method, which aimed at measuring LiDAR point clouds for stem volume. The development of stage one was the fundamental work not only for VWD methods but also for verification. In this stage, how to design and implement a specific physical simulation scenario was demonstrated. In the absence of references, Unity and PhysX were successfully employed to establish the physical simulation scenario of water displacement in virtual space. It provided answers to the first research question by demonstrating the feasibility of physical simulations. The result showed that, compared to the true volume, the VWD measuring result had 6.0% overestimation rate. Meanwhile the QSM modeling method result was 6.4% underestimation. However, due to the restrictions from hardware performance and the physical engine, the VWD method had to employ empirical processes at the first stage.

The development of stage two successfully modified the original VWD method in order to exclude any empirical procedure at stage one. One of the significant changes was that the consumption of VWMs deduced from a few thousand to several. This decreasing consumption of VWMs exhibited two advantages. The first advantage was the great release of computer power. The second advantage was the exclusion of the simulation of the VWMs' interaction. Consequently, this new physical scenario eliminated the empirical processes in stage one. Meanwhile, the VWD method was a fully automatic method to measure LiDAR point clouds in the final. Compared to conventional modeling methods, there was no need to know the true volume using additional methods anymore.

The second implementation of CVM was sunlight analysis. Different from the VWD method, the sunlight analysis set tree models as the measuring target instead of point clouds. Therefore, it simulated the physical scenarios of the solar illumination to investigate light

conditions for trees during the daylight. The development of stage one provided a facile approach using architecture software to analyze light conditions for trees. Different from the VWD, stage one of sunlight analysis demonstrated another solution to simulate physical scenarios. Different applications were integrated without the need for coding. The results for the demonstrational target tree showed that there was only 3.34% (0.62 m^2) of the tree surface exposed in the sunlight during the whole day (8 hours of simulation). Meanwhile, 35.87% (5.16 m^2) of the tree surface was illuminated by the sun for less than one hour. The technical feature of sunlight analysis was the flexibility on the date, geo-positions, simulation duration, and free of weather conditions. Those features provided wide applicability for NFI sample plots regardless of different site conditions.

In stage two of sunlight analysis, a VSP was established instead of a single tree. By applying the same methods in different scenes, the shading effect of neighboring trees was quantitatively determined. Due to the restriction of current measuring technologies, it is unable to duplicate the same physical scenarios in reality. It provided the power of physical simulation. Both stages of sunlight analysis provided the answer for the second research question, i.e., how many tree or forest parameters can be extracted using the potential new methods.

7.2 Computational virtual measurement (CVM)

The development of two implementations verified the overall concept of CVM, i.e., measuring trees by simulating physical scenarios of real measuring instruments. As virtual measuring tools, no additional reference was required due to the algorithm logic. In CVM processes, the lack of mathematic predictions led to the no need for validation. Figure.7-1 summarized these two implementations, along with the essential concept of CVM. CVM method used 1st measurement in the real world to collect spatial information of trees. Afterward, it applied the 2nd measurement in virtual spaces to convert collected information to tree parameters.
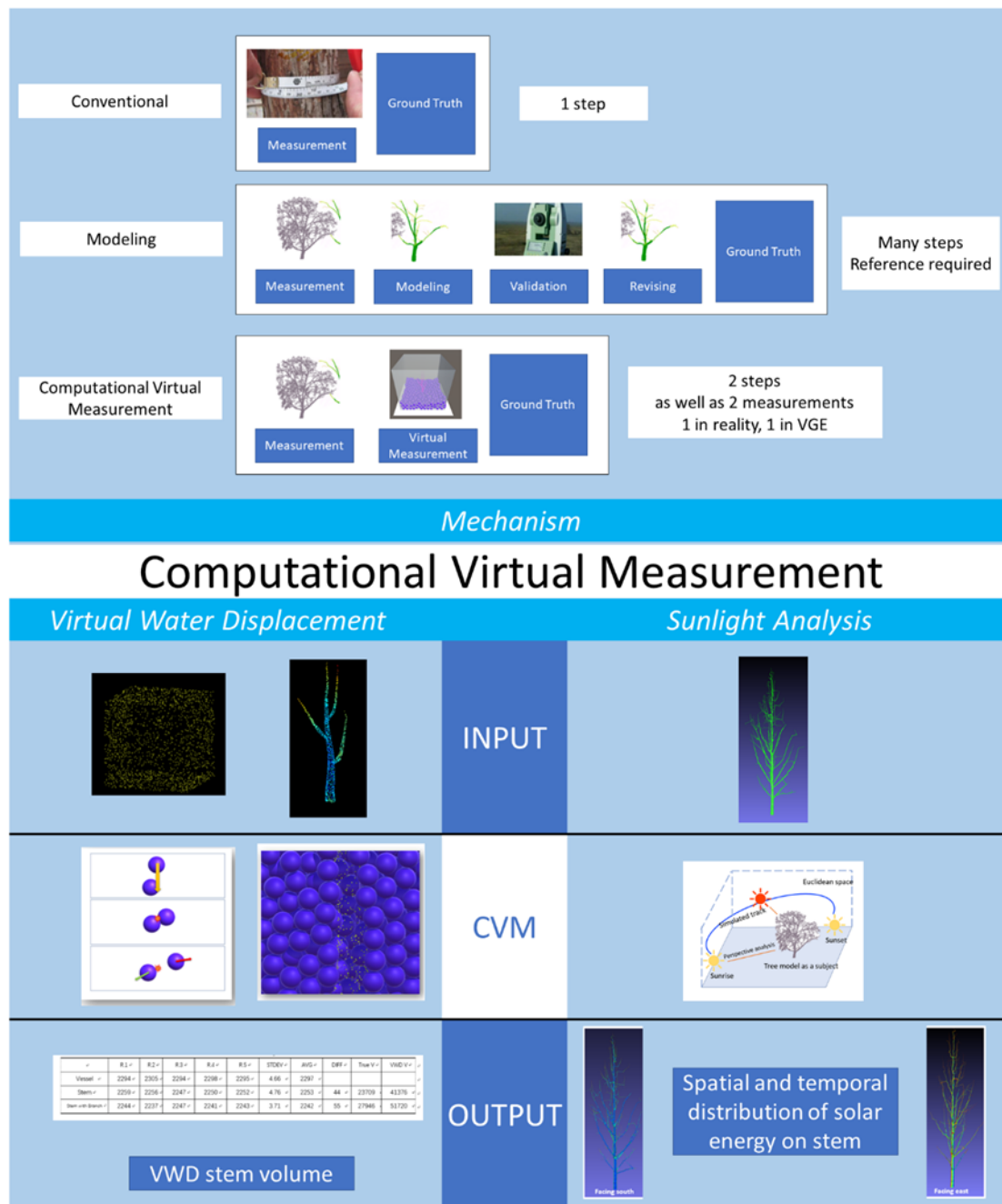
Figure.7-1. Graphical conclusion of CVM.

In contrast to one-step measurement using conventional measuring instruments, CVM separated one-step measurement into two consecutive steps in different realities. It seemed that the workload was doubled. However, two measuring processes of conventional measuring instruments were actually distributed into two CVM measurements as well. In other words, this separation of measurements did not increase the total number of measuring processes. Consequently, the increasing of source of error was limited.

The first measuring process of real instruments was to determine the spatial information of themselves in forest sites. Accordingly, the spatial information of their targets, i.e., trees, can be determined. The second measuring process of real instruments was to measure trees using their specific physical scenarios. Corresponding to these measuring processes, CVM collect spatial information of trees only in the first measurement. Then, in the second measurement, CVM measures the collected spatial information of trees by the simulation of physical scenarios of real measuring instruments. That was why no additional processes are added in CVM compared to conventional measurements in forest sites. Figure.7-2 shows the conclusion of processes in CVM.
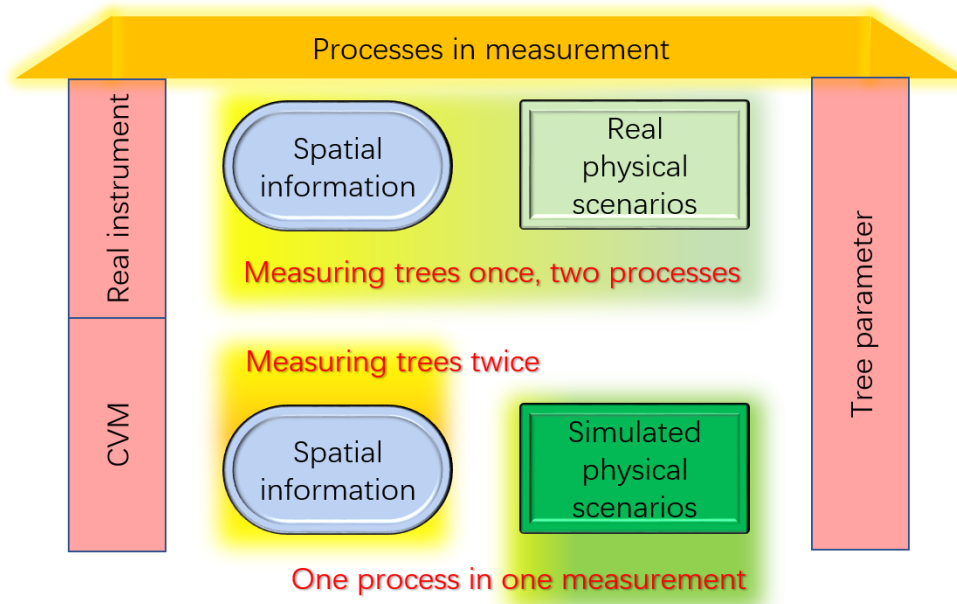
Figure 7-2. The conclusion of measuring processes in CVM and conventional measurements. The hall of CVM.

By counting the quantity of measuring processes, conventional measurements using real instruments were literally equivalent to CVM, as shown in Fig.7-2. The first process of the two methods was the collection of spatial information in forests. In this process, both methods collected data using real measuring instruments. Due to the employment of novel technologies, e.g., LiDAR scanner in this study, it was expected to acquire improvements in the collection of spatial information. However, physical scenarios of conventional instruments were hard to be reproduced by novel instruments. At this moment, CVM took over the workflow. Instead of modeling, CVM restricted the scope of work still in the

measurement literally.

In the second process, the experience in two CVM implementations showed that the simulation of physical scenarios consisted of the simulation of basic physical laws. Meanwhile, these simulations were derived by third-party applications. The simulation of basic physical laws was reported to be high arcuate. To sum up, from the perspective of the quantity of measuring processes, CVM could be equivalent to a real measuring instrument.

Compared to conventional modeling methods, CVM is considered higher than them at the algorithm level by making no models. That is because, the result of a modeling method is a model. Fundamentally, a model itself is an abstract of information. On the contrary, CVM does not have the process of abstracting. The following Eq.7-1,2 and 3 describe the difference between CVM and conventional modeling methods. Where P_n refers to the natural information of trees; P_m refers to the ideal model abstracted from natural information; P_{mp} refers to the model which can be actually produced by modeling methods; P_{cvm} refers to information derived by CVM from natural information; δ_{1cvm}, δ_{1m}, and δ_{2m} refer to the loss of information.

$$\lim(P_n - P_m) = \delta_{1m} \tag{7-1}$$

$$lim(P_m - P_{mp}) = \delta_{2mp} \tag{7-2}$$

$$lim(P_n - P_{cvm}) = \delta_{1cvm} \tag{7-3}$$

In the above equations, P_n represents the true value of a tree parameter that existed in nature. It is well known that it cannot be known exactly by any method. The difference between true value and values derived by methods is marked using δ. In the situation of the use of the same data source, e.g., LiDAR point clouds, the source of error between CVM and conventional methods is equal. Therefore, this source of error is not to be discussed. Then, in modeling methods, the first loss of information against the true value happens on the assumption of the ideal model. This loss is marked using δ_{1m}. At the same

time, the first loss for CVM happens in the simulation of physical scenarios of real measuring instruments. This loss is marked using δ_{1cvm}. According to experience in virtual ruler and VWD method, it can be concluded that for a specific CVM implementation, δ_{1cvm} can be far less than δ_{1m}. That is because, there is no prior knowledge is needed in CVM. It reduces the source of error accordingly. More than this, CVM does not possess another systematic error in conventional modeling methods, e.g., δ_{2mp}.

More than the discussion in the regime of information loss, CVM even had the ability to increase the absolute amount of raw data. Technically, CVM created a physical behavior layer based on the raw layer, which recorded spatial information. Accordingly, tree parameters were divided from so-called artificial multiple data sources (AMDS) or single-multiple data sources (SDMS) defined by this study. Compared to conventional modeling methods that processed the raw spatial layer, the significance of AMDS (or SDMS) could be learned from experiences in related studies, e.g., remote sensing [188-190].

7.3 Outlook: potential fully-automatic NFI sample plot measurements

For decades, the integration of different measurement technologies, e.g., the fusion of multiple data sources, acts as the primary research tool in forest measurements [189,191]. In those studies, only one or a few tree parameters could be determined using complicated workflows. On the contrary, LiDAR technology was facile on the determination of multiple tree parameters using a single measuring mechanism [11,48,74]. This feature made LiDAR as a possibility to replace all the conventional measurement methods in NFI sample plot measurements.

As shown in Fig.7-3(left), the current NFI field measurements applied a loop workflow. Field crews measured tree parameters one tree by one tree. In sample plots, different measuring instruments, i.e., fabric tape for DBH and angle gauge for tree height, were utilized. The diversity of measuring instruments can lead to various sources of errors. If these conventional measuring procedures can be replaced with a LiDAR scanning, it would be beneficial in two aspects: simplifying the measuring mechanism and the reduction of human error [11,65,192]. Furthermore, LiDAR can be alternatives for destructive

methods [193,194]. As previously stated (in 2.2.3), all tree parameters collected by NFI using conventional measuring instruments have LiDAR methods alternatively. However, the long chain of validation prevents the implementation of those methods using in NFI. It is a widely held view that NFI is an information collection system that utilizes well-developed methods and has no interest in testing new methods.
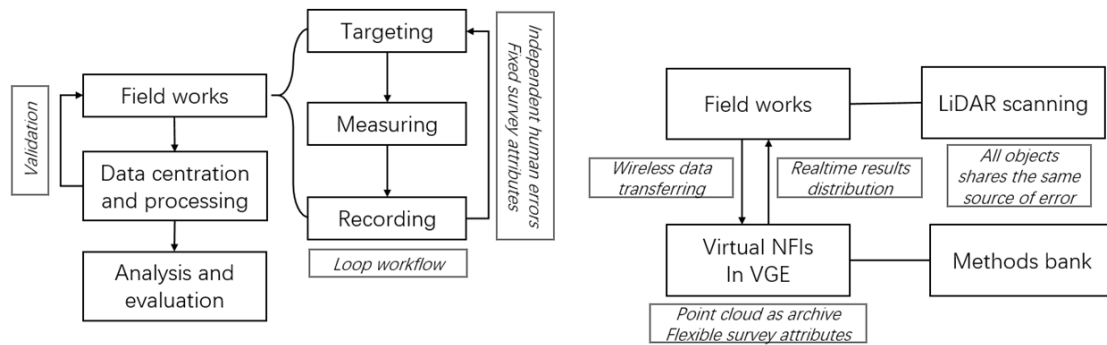
Figure 7-3. Current (left) and virtual NFIs workflow (right) for sample plot measurement and data process.

The CVM methods presented in this thesis demonstrated the possibility to extract tree parameters from raw LiDAR point clouds without additional reference data. It measured several tree parameters, which can only be estimated using modeling methods on pint clouds. CVM was a measuring instrument. Based on those features, in the future, the field crew will be only responsible for applying LiDAR scanning in sample plots during this fully automatic NFI sample plot measurements. Meanwhile, the field crew is not responsible for making decisions on the measuring procedure, i.e., to determine where is the highest point of a tree. In this procedure, the required tree parameters will be accomplished in the data center. Thus, errors from human decisions will be excluded in the sample plot measurement systematically. The advantages are: (i) reduction of human errors; (ii) LiDAR point cloud acts as raw data, which adopts the future upgrades of data processing algorithms. With this, it can be foreseen that with the development of automatic LiDAR scanning by UAV and related approaches, the work burden for the field crew will be obviously reduced in the near future. This new form of NFI was named as virtual NFI(VNFI). There are two steps: (i) LiDAR scanning in sample plots; and (ii) CVM in

virtual spaces.

A comparison of workflows between the NFI and virtual NFI is shown in Fig. 7-3. For the physical measurement in NFI, the key advantage of LiDAR sampling is that it has the determined and universal sources of error. On the contrary, the loop measurement of trees is an independent process and relying on human cognition. For the data process, the virtual NFI separates the physical measurement and the other workflows completely. The key change locates in the form of metadata, which is the collected point clouds. Compared to the current form of metadata, i.e., values refereed to tree parameters, the advantages of the point clouds as the metadata are: (i) it depicts the sample plot more nature than the literal parameters; (ii) the source of error is determined; and (iii) it is ready for data re-processing and adoptive for future methods.

The theory of CVM acts as a theoretical preparation for the virtual NFI. Many predictable and unpredictable difficulties exist in the path of the future. As a proverb put it, *"A journey of a thousand miles begins with a single step"*.

(the end)

Reference

1. Trumbore, S.; Brando, P.; Hartmann, H. Forest health and global change. *Science* **2015**, *349*, 814.

2. Giam, X. Global biodiversity loss from tropical deforestation. *Proceedings of the National Academy of Sciences* **2017**, *114*, 5775-5777.

3. Chazdon, R.L. Tropical forest recovery: Legacies of human impact and natural disturbances. *Perspectives in Plant Ecology, Evolution and Systematics* **2003**, *6*, 51-71.

4. Keenan, R.J.; Reams, G.A.; Achard, F.; de Freitas, J.V.; Grainger, A.; Lindquist, E. Dynamics of global forest area: Results from the fao global forest resources assessment 2015. *Forest Ecol Manag* **2015**, *352*, 9-20.

5. Bala, G.; Caldeira, K.; Wickett, M.; Phillips, T.J.; Lobell, D.B.; Delire, C.; Mirin, A. Combined climate and carbon-cycle effects of large-scale deforestation. *Proceedings of the National Academy of Sciences* **2007**, *104*, 6550-6555.

6. MacDicken, K.G. Global forest resources assessment 2015: What, why and how? *Forest Ecol Manag* **2015**, *352*, 3-8.

7. Duinker, P.N. Criteria and indicators of sustainable forest management in canada: Progress and problems in integrating science and politics at the local level. *Criteria and Indicators for Sustainable Forest Management at the Forest Management Unit Level, Proceedings of the European Forest Institute* **2001**, 7-27.

8. MacDicken, K.G.; Sola, P.; Hall, J.E.; Sabogal, C.; Tadoum, M.; de Wasseige, C. Global progress toward sustainable forest management. *Forest Ecol Manag* **2015**, *352*, 47-56.

9. Chen, J.; Chen, J.; Liao, A.; Cao, X.; Chen, L.; Chen, X.; He, C.; Han, G.; Peng, S.; Lu, M.*, et al.* Global land cover mapping at 30m resolution: A pok-based operational approach. *Isprs J Photogramm* **2015**, *103*, 7-27.

10. Gillis, M.D.; Omule, A.Y.; Brierley, T. Monitoring canada's forests: The national forest inventory. https://nfi.nfis.org/resources/Monitoring_NFI_2005.pdf

11. Liang, X.; Kankare, V.; Hyyppä, J.; Wang, Y.; Kukko, A.; Haggrén, H.; Yu, X.; Kaartinen, H.; Jaakkola, A.; Guan, F. Terrestrial laser scanning in forest inventories. *Isprs J Photogramm* **2016**, *115*, 63-77.

12. Bower, D.R.; Blocker, W.W. Notes and observations: Accuracy of bands and tape for measuring diameter increments. *J Forest* **1966**, *64*, 21-22.

13. Segura, M.; Kanninen, M. Allometric models for tree volume and total aboveground biomass in a tropical humid forest in costa rica 1. *Biotropica: The Journal of Biology and Conservation* **2005**, *37*, 2-8.

14. Wang, C. Biomass allometric equations for 10 co-occurring tree species in chinese temperate forests. *Forest Ecol Manag* **2006**, *222*, 9-16.

15. Muukkonen, P. Generalized allometric volume and biomass equations for some tree species in europe. *Eur J Forest Res* **2007**, *126*, 157-166.

16. Henry, M.; Bombelli, A.; Trotta, C.; Alessandrini, A.; Birigazzi, L.; Sola, G.; Vieilledent, G.; Santenoise, P.; Longuetaud, F.; Valentini, R. Globallometree: International platform for tree allometric equations to support volume, biomass and carbon assessment. *Iforest* **2013**, *6*, 326-330.

17. Liang, X.; Litkey, P.; Hyyppa, J.; Kaartinen, H.; Vastaranta, M.; Holopainen, M. Automatic stem mapping using single-scan terrestrial laser scanning. *Ieee T Geosci Remote* **2012**, *50*, 661-670.

18. Liang, X.; Hyyppä, J.; Kaartinen, H.; Lehtomäki, M.; Pyörälä, J.; Pfeifer, N.; Holopainen, M.; Brolly, G.; Francesco, P.; Hackenberg, J*., et al.* International benchmarking of terrestrial laser scanning approaches for forest inventories. *Isprs J Photogramm* **2018**, *144*, 137-179.

19. Huang, H.; Li, Z.; Gong, P.; Cheng, X.; Clinton, N.; Cao, C.; Ni, W.; Wang, L. Automated methods for measuring dbh and tree heights with a commercial scanning lidar. *Photogrammetric Engineering & Remote Sensing* **2011**, *77*, 219-227.

20. Liang, X.; Wang, Y.; Pyörälä, J.; Lehtomäki, M.; Yu, X.; Kaartinen, H.; Kukko, A.; Honkavaara, E.; Issaoui, A.E.I.; Nevalainen, O*., et al.* Forest in situ observations using unmanned aerial vehicle as an alternative of terrestrial measurements. *For. Ecosyst.* **2019**, *6*, 20.

21. Thiel, C.; Schmullius, C. Comparison of uav photograph-based and airborne lidar-based point clouds over forest from a forestry application perspective. *Int J Remote Sens* **2017**, *38*, 2411-2426.

22. Ene, L.T.; Naesset, E.; Gobakken, T.; Gregoire, T.G.; Stahl, G.; Holm, S. A simulation approach for accuracy assessment of two-phase post-stratified estimation in large-area lidar biomass surveys. *Remote Sens Environ* **2013**, *133*, 210-224.

23. He, Q.S.; Chen, E.X.; An, R.; Li, Y. Above-ground biomass and biomass components estimation using lidar data in a coniferous forest. *Forests* **2013**, *4*, 984-1002.

24. Hosoi, F.; Nakai, Y.; Omasa, K. 3-d voxel-based solid modeling of a broad-leaved tree for accurate volume estimation using portable scanning lidar. *Isprs J Photogramm* **2013**, *82*, 41-48.

25. Raumonen, P.; Kaasalainen, M.; Åkerblom, M.; Kaasalainen, S.; Kaartinen, H.; Vastaranta, M.; Holopainen, M.; Disney, M.; Lewis, P. Fast automatic precision tree models from terrestrial laser scanner data. *Remote Sens-Basel* **2013**, *5*, 491-520.

26. Hackenberg, J.; Morhart, C.; Sheppard, J.; Spiecker, H.; Disney, M. Highly

accurate tree models derived from terrestrial laser scan data: A method description. *Forests* **2014**, *5*, 1069.

27.   Åkerblom, M.; Raumonen, P.; Casella, E.; Disney, M.I.; Danson, F.M.; Gaulton, R.; Schofield, L.A.; Kaasalainen, M. Non-intersecting leaf insertion algorithm for tree structure models. *Interface Focus* **2018**, *8*, 20170045.

28.   Tomppo, E.; Haakana, M.; Katila, M.; Mäkisara, K.; Peräsaari, J. The multi-source national forest inventory

of   finland   –   methods   and   results   2005. http://www.metla.fi/julkaisut/workingpapers/2009/mwp111.pdf

29.   USDA.   Phase   2   and   phase   3:   Ground   measurements. https://www.fia.fs.fed.us/library/fact-sheets/data-collections/Phase2_3.pdf

30.   (Metla), t.F.F.R.I.   Previous   nfis.   http://www.metla.fi/ohjelma/vmi/vmi-historia-en.htm

31.   Metla.   Reliable   information   on   forest   resources   since   1920. http://www.metla.fi/ohjelma/vmi/info-en.htm

32.   CFA.   National   forest   inventory   technical   regulations. http://211.167.243.162:8085/8/adminf/ueditor/jsp/upload/20140520/663314005540 61640.pdf

33.   Bundeswaldinventur.   Surveying   the   forest. https://www.bundeswaldinventur.de/index.php?id=684&L=3#c1685

34.   Hiley, W. The forests of suomi (finland). Results of the general survey of the forests of the country carried out during the years 1921-1924. JSTOR: 1927.

35.   Bienert, A.; Hess, C.; Maas, H.-G.; Oheimb, G.v. In *A voxel-based technique to estimate the volume of trees from terrestrial laser scanner data*, 2014.

36.   Dassot, M.; Colin, A.; Santenoise, P.; Fournier, M.; Constant, T. Terrestrial laser scanning for measuring the solid wood volume, including branches, of adult standing trees in the forest environment. *Comput Electron Agr* **2012**, *89*, 86-93.

37.   Hackenberg, J.; Wassenberg, M.; Spiecker, H.; Sun, D. Non destructive method for biomass prediction combining tls derived tree volume and wood density. *Forests* **2015**, *6*, 1274.

38.   Heinrich,   J.   Measuring   the   forests. https://www.thuenen.de/en/topics/biological-diversity/waelder-divers-und-bio/den-wald-vermessen/ (10.31.2019),

39.   NFIS. Canada's national forest inventory national standard for photo plots https://nfi.nfis.org/resources/photoplot/Pp_data_dictionary_4.2.4.pdf

40.   Qin, Y.; Xiao, X.; Dong, J.; Zhang, G.; Shimada, M.; Liu, J.; Li, C.; Kou, W.; Moore, B. Forest cover maps of china in 2010 from multiple approaches and data

sources: Palsar, landsat, modis, fra, and nfi. *Isprs J Photogramm* **2015**, *109*, 1-16.

41.   Iverson, L.; Cook, E.; Graham, R. A technique for extrapolating and validating forest cover across large regions calibrating avhrr data with tm data. *Int J Remote Sens* **1989**, *10*, 1805-1812.

42.   Hansen, M.C.; Shimabukuro, Y.E.; Potapov, P.; Pittman, K. Comparing annual modis and prodes forest cover change data for advancing monitoring of brazilian forest cover. *Remote Sens Environ* **2008**, *112*, 3784-3793.

43.   Wagner, W.; Luckman, A.; Vietmeier, J.; Tansey, K.; Balzter, H.; Schmullius, C.; Davidson, M.; Gaveau, D.; Gluck, M.; Le Toan, T. Large-scale mapping of boreal forest in siberia using ers tandem coherence and jers backscatter data. *Remote Sens Environ* **2003**, *85*, 125-144.

44.   Lesiv, M.; Moltchanova, E.; Schepaschenko, D.; See, L.; Shvidenko, A.; Comber, A.; Fritz, S. Comparison of data fusion methods using crowdsourced data in creating a hybrid forest cover map. *Remote Sens-Basel* **2016**, *8*, 261.

45.   Baltsavias, E.P. Airborne laser scanning: Basic relations and formulas. *Isprs J Photogramm* **1999**, *54*, 199-214.

46.   Nie, S.; Wang, C.; Xi, X.; Luo, S.; Li, S.; Tian, J. Estimating the height of wetland vegetation using airborne discrete-return lidar data. *Optik - International Journal for Light and Electron Optics* **2018**, *154*, 267-274.

47.   Lim, K.; Treitz, P.; Wulder, M.; St-Onge, B.; Flood, M. Lidar remote sensing of forest structure. *Progress in Physical Geography: Earth and Environment* **2003**, *27*, 88-106.

48.   Wulder, M.A.; White, J.C.; Nelson, R.F.; Næsset, E.; Ørka, H.O.; Coops, N.C.; Hilker, T.; Bater, C.W.; Gobakken, T. Lidar sampling for large-area forest characterization: A review. *Remote Sens Environ* **2012**, *121*, 196-209.

49.   Nelson, R. Model effects on glas-based regional estimates of forest biomass and carbon. *Int J Remote Sens* **2010**, *31*, 1359-1372.

50.   Xie, J.; Tang, X.; Mo, F.; Li, G.; Zhu, G.; Wang, Z.; Fu, X.; Gao, X.; Dou, X. Zy3-02 laser altimeter footprint geolocation prediction. *Sensors-Basel* **2017**, *17*, 2165.

51.   Réjou-Méchain, M.; Tymen, B.; Blanc, L.; Fauset, S.; Feldpausch, T.R.; Monteagudo, A.; Phillips, O.L.; Richard, H.; Chave, J. Using repeated small-footprint lidar acquisitions to infer spatial and temporal variations of a high-biomass neotropical forest. *Remote Sens Environ* **2015**, *169*, 93-101.

52.   Brede, B.; Lau, A.; Bartholomeus, H.M.; Kooistra, L. Comparing riegl ricopter uav lidar derived canopy height and dbh with terrestrial lidar. *Sensors-Basel* **2017**, *17*, 2371.

53.   Wallace, L.; Lucieer, A.; Malenovský, Z.; Turner, D.; Vopěnka, P. Assessment of forest structure using two uav techniques: A comparison of airborne laser scanning

and structure from motion (sfm) point clouds. *Forests* **2016**, *7*, 62.

54.   Saarinen, N.; Kankare, V.; Vastaranta, M.; Luoma, V.; Pyörälä, J.; Tanhuanpää, T.; Liang, X.; Kaartinen, H.; Kukko, A.; Jaakkola, A*., et al.* Feasibility of terrestrial laser scanning for collecting stem volume information from single trees. *Isprs J Photogramm* **2017**, *123*, 140-158.

55.   Raumonen, P.; Kaasalainen, M.; Akerblom, M.; Kaasalainen, S.; Kaartinen, H.; Vastaranta, M.; Holopainen, M.; Disney, M.; Lewis, P. Fast automatic precision tree models from terrestrial laser scanner data. *Remote Sens-Basel* **2013**, *5*, 491-520.

56.   Guoyuan, L.; Xinming, T. Analysis and validation of zy-3 02 satellite laser altimetry data. *Acta Geodaetica et Cartographica Sinica* **2017**, *46*, 1939-1949.

57.   Wehr, A.; Lohr, U. Airborne laser scanning—an introduction and overview. *Isprs J Photogramm* **1999**, *54*, 68-82.

58.   Cao, L.; Coops, N.C.; Innes, J.L.; Dai, J.; Ruan, H.; She, G. Tree species classification in subtropical forests using small-footprint full-waveform lidar data. *Int J Appl Earth Obs* **2016**, *49*, 39-51.

59.   Gupta, S.G.; Ghonge, M.M.; Jawandhiya, P. Review of unmanned aircraft system (uas). *International Journal of Advanced Research in Computer Engineering & Technology (IJARCET)* **2013**, *2*, pp: 1646-1658.

60.   Wallace, L.; Lucieer, A.; Watson, C.; Turner, D. Development of a uav-lidar system with application to forest inventory. *Remote Sens-Basel* **2012**, *4*, 1519.

61.   Westoby, M.; Brasington, J.; Glasser, N.; Hambrey, M.; Reynolds, J. 'Structure-from-motion'photogrammetry: A low-cost, effective tool for geoscience applications. *Geomorphology* **2012**, *179*, 300-314.

62.   Odipo, V.O.; Nickless, A.; Berger, C.; Baade, J.; Urbazaev, M.; Walther, C.; Schmullius, C. Assessment of aboveground woody biomass dynamics using terrestrial laser scanner and l-band alos palsar data in south african savanna. *Forests* **2016**, *7*, 294.

63.   Dassot, M.; Constant, T.; Fournier, M. The use of terrestrial lidar technology in forest science: Application fields, benefits and challenges. *Ann Forest Sci* **2011**, *68*, 959-974.

64.   Zhang, C.; Chen, M.; Li, R.; Fang, C.; Lin, H. What's going on about geo-process modeling in virtual geographic environments (vges). *Ecol Model* **2016**, *319*, 147-154.

65.   Maas, H.G.; Bienert, A.; Scheller, S.; Keane, E. Automatic forest inventory parameter determination from terrestrial laser scanner data. *Int J Remote Sens* **2008**, *29*, 1579-1593.

66.   Thies *, M.; Pfeifer, N.; Winterhalder, D.; Gorte, B.G.H. Three-dimensional reconstruction of stems for assessment of taper, sweep and lean based on laser

scanning of standing trees. *Scand J Forest Res* **2004**, *19*, 571-581.

67.   Chen, M.; Wan, Y.; Wang, M.; Xu, J. Automatic stem detection in terrestrial laser scanning data with distance-adaptive search radius. *Ieee T Geosci Remote* **2018**, *56*, 2968-2979.

68.   Liang, X.; Hyyppä, J. Automatic stem mapping by merging several terrestrial laser scans at the feature and decision levels. *Sensors-Basel* **2013**, *13*, 1614.

69.   Heinzel, J.; Huber, M. Detecting tree stems from volumetric tls data in forest environments with rich understory. *Remote Sens-Basel* **2017**, *9*, 9.

70.   Olofsson, K.; Holmgren, J.; Olsson, H. Tree stem and height measurements using terrestrial laser scanning and the ransac algorithm. *Remote Sens-Basel* **2014**, *6*, 4323.

71.   Wieser, M.; Mandlburger, G.; Hollaus, M.; Otepka, J.; Glira, P.; Pfeifer, N. A case study of uas borne laser scanning for measurement of tree stem diameter. *Remote Sens-Basel* **2017**, *9*, 1154.

72.   Moskal, L.M.; Zheng, G. Retrieving forest inventory variables with terrestrial laser scanning (tls) in urban heterogeneous forest. *Remote Sens-Basel* **2011**, *4*, 1-20.

73.   Lohani, B.; Ghosh, S. Airborne lidar technology: A review of data collection and processing systems. *Proceedings of the National Academy of Sciences, India Section A: Physical Sciences* **2017**, *87*, 567-579.

74.   Torresan, C.; Berton, A.; Carotenuto, F.; Di Gennaro, S.F.; Gioli, B.; Matese, A.; Miglietta, F.; Vagnoli, C.; Zaldei, A.; Wallace, L. Forestry applications of uavs in europe: A review. *Int J Remote Sens* **2017**, *38*, 2427-2447.

75.   Komiyama, A.; Ong, J.E.; Poungparn, S. Allometry, biomass, and productivity of mangrove forests: A review. *Aquat Bot* **2008**, *89*, 128-137.

76.   Martin, A.J. Testing volume equation accuracy with water displacement techniques. *Forest Sci* **1984**, *30*, 41-50.

77.   Unger, D.R.; Hung, I.K.; Brooks, R.; Williams, H. Estimating number of trees, tree height and crown width using lidar data. *Gisci Remote Sens* **2014**, *51*, 227-238.

78.   Bragg, D.C. A local basal area adjustment for crown width prediction. *North J Appl For* **2001**, *18*, 22-28.

79.   Jung, S.-E.; Kwak, D.-A.; Park, T.; Lee, W.-K.; Yoo, S. Estimating crown variables of individual trees using airborne and terrestrial laser scanners. *Remote Sens-Basel* **2011**, *3*, 2346.

80.   Oberbauer, S.F.; Strain, B.R. Photosynthesis and successional status of costa rican rain forest trees. *Photosynthesis Research* **1984**, *5*, 227-232.

81.   Green, S.R. Radiation balance, transpiration and photosynthesis of an isolated tree. *Agr Forest Meteorol* **1993**, *64*, 201-221.

82.   Iwasa, Y.; Cohen, D.; Leon, J.A. Tree height and crown shape, as results of competitive games. *J Theor Biol* **1985**, *112*, 279-297.

83.   Kozlowski, T.T. Light and water in relation to growth and competition of piedmont forest tree species. *Ecol Monogr* **1949**, *19*, 207-231.

84.   Gravel, D.; Canham, C.D.; Beaudet, M.; Messier, C. Shade tolerance, canopy gaps and mechanisms of coexistence of forest trees. *Oikos* **2010**, *119*, 475-484.

85.   Gendron, F.; Messier, C.; Comeau, P.G. Comparison of various methods for estimating the mean growing season percent photosynthetic photon flux density in forests. *Agr Forest Meteorol* **1998**, *92*, 55-70.

86.   Kato, S.; Komiyama, A. Spatial and seasonal heterogeneity in understory light conditions caused by differential leaf flushing of deciduous overstory trees. *Ecol Res* **2002**, *17*, 687-693.

87.   Parent, S.; Messier, C. A simple and efficient method to estimate microsite light availability under a forest canopy. *Can J Forest Res* **1996**, *26*, 151-154.

88.   Bunce, J.A. Effects of weather during leaf development on photosynthetic characteristics of soybean leaves. *Photosynthesis research* **1985**, *6*, 215-220.

89.   Pretzsch, H. Canopy space filling and tree crown morphology in mixed-species stands compared with monocultures. *Forest Ecol Manag* **2014**, *327*, 251-264.

90.   Deleuze, C.; Hervé, J.-C.; Colin, F.; Ribeyrolles, L. Modelling crown shape of piceaabies: Spacing effects. *Can J Forest Res* **1996**, *26*, 1957-1966.

91.   Pretzsch, H. Re-evaluation of allometry: State-of-the-art and perspective regarding individuals and stands of woody plants. In *Progress in botany 71*, Springer: 2010; pp 339-369.

92.   Peper, P.J.; McPherson, E.G.; Mori, S.M. Equations for predicting diameter, height, crown width, and leaf area of san joaquin valley street trees. *journal of Arboriculture* **2001**, *27*, 306-317.

93.   Bechtold, W.A. Largest-crown-width prediction models for 53 species in the western united states. *West J Appl For* **2004**, *19*, 245-251.

94.   Ferraz, A.; Saatchi, S.; Mallet, C.; Meyer, V. Lidar detection of individual tree size in tropical forests. *Remote Sens Environ* **2016**, *183*, 318-333.

95.   Whitmore, T. Canopy gaps and the two major groups of forest trees. *Ecology* **1989**, *70*, 536-538.

96.   Bagaram, M.; Giuliarelli, D.; Chirici, G.; Giannetti, F.; Barbati, A. Uav remote sensing for biodiversity monitoring: Are forest canopy gaps good covariates? *Remote Sens-Basel* **2018**, *10*, 1397.

97.   Bréda, N.J. Ground-based measurements of leaf area index: A review of methods, instruments and current controversies. *Journal of experimental botany*

2003, *54*, 2403-2417.

98.   Weiss, M.; Baret, F.; Smith, G.; Jonckheere, I.; Coppin, P. Review of methods for in situ leaf area index (lai) determination: Part ii. Estimation of lai, errors and sampling. *Agr Forest Meteorol* **2004**, *121*, 37-53.

99.   Kitao, M.; Hida, T.; Eguchi, N.; Tobita, H.; Utsugi, H.; Uemura, A.; Kitaoka, S.; Koike, T. Light compensation points in shade-grown seedlings of deciduous broadleaf tree species with different successional traits raised under elevated co2. *Plant Biol.* **2016**, *18*, 22-27.

100. Song, Q.; Xiao, H.; Xiao, X.; Zhu, X.-G. A new canopy photosynthesis and transpiration measurement system (capts) for canopy gas exchange research. *Agr Forest Meteorol* **2016**, *217*, 101-107.

101. Hu, Y.; Zhao, P.; Niu, J.; Sun, Z.; Zhu, L.; Ni, G. Canopy stomatal uptake of nox, so2 and o3 by mature urban plantations based on sap flow measurement. *Atmos Environ* **2016**, *125*, 165-177.

102. Batty, M. Virtual geography. *Futures* **1997**, *29*, 337-352.

103. Lin, H.; Gong, J. Exploring virtual geographic environments. *Geographic Information Sciences* **2001**, *7*, 1-7.

104. Chen, M.; Lin, H.; Lu, G. Virtual geographic environments. *International Encyclopedia of Geography: People, the Earth, Environment and Technology: People, the Earth, Environment and Technology* **2016**, 1-11.

105. Lin, H.; Chen, M.; Lu, G.; Zhu, Q.; Gong, J.; You, X.; Wen, Y.; Xu, B.; Hu, M. Virtual geographic environments (vges): A new generation of geographic analysis tool. *Earth-Science Reviews* **2013**, *126*, 74-84.

106. Mekni, M. *Automated generation of geometrically-precise and semantically-informed virtual geographic environments populated with spatially-reasoning agents*. Universal-Publishers: 2010.

107. Liang, J.; Gong, J.; Li, Y. Realistic rendering for physically based shallow water simulation in virtual geographic environments (vges). *Annals of GIS* **2015**, *21*, 301-312.

108. Xu, B.; Lin, H.; Chiu, L.; Hu, Y.; Zhu, J.; Hu, M.; Cui, W. Collaborative virtual geographic environments: A case study of air pollution simulation. *Information Sciences* **2011**, *181*, 2231-2246.

109. Chen, M.; Lin, H.; Hu, M.; He, L.; Zhang, C. Real-geographic-scenario-based virtual social environments: Integrating geography with social research. *Environment and Planning B: Planning and Design* **2013**, *40*, 1103-1121.

110. Song, Y.; Gong, J.; Li, Y.; Cui, T.; Fang, L.; Cao, W. Crowd evacuation simulation for bioterrorism in micro-spatial environments based on virtual geographic environments. *Safety science* **2013**, *53*, 105-113.

111. Lv, Z.; Li, X.; Hu, J.; Yin, L.; Zhang, B.; Feng, S. In *Virtual geographic environment based coach passenger flow forecasting*, 2015 IEEE International Conference on Computational Intelligence and Virtual Environments for Measurement Systems and Applications (CIVEMSA), 12-14 June 2015, 2015; pp 1-6.

112. Lü, G. Geographic analysis-oriented virtual geographic environment: Framework, structure and functions. *Science China Earth Sciences* **2011**, *54*, 733-743.

113. Haklay, M.; Singleton, A.; Parker, C. Web mapping 2.0: The neogeography of the geoweb. *Geography Compass* **2008**, *2*, 2011-2039.

114. Zhu, J.; Yin, L.; Wang, J.; Zhang, H.; Hu, Y.; Liu, Z. Dam-break flood routing simulation and scale effect analysis based on virtual geographic environment. *Ieee J-Stars* **2014**, *8*, 105-113.

115. Burns, D.; Osfield, R. In *Tutorial: Open scene graph a: Introduction tutorial: Open scene graph b: Examples and applications*, IEEE Virtual Reality 2004, 2004; IEEE: pp 265-265.

116. Zhu, J.; Wang, J.H. In *Interactive virtual globe service system based on osgearth*, Applied Mechanics and Materials, 2013; Trans Tech Publ: pp 680-684.

117. Moore, A.B.; Bricker, M. 'Mountains of work': Spatialization of work projects in a virtual geographic environment. *Annals of GIS* **2015**, *21*, 313-323.

118. Zhang, C.; Chen, M.; Li, R.; Ding, Y.; Lin, H. A virtual geographic environment system for multiscale air quality analysis and decision making: A case study of so2 concentration simulation. *Appl Geogr* **2015**, *63*, 326-336.

119. Yin, L.; Zhu, J.; Li, Y.; Zeng, C.; Zhu, Q.; Qi, H.; Liu, M.; Li, W.; Cao, Z.; Yang, W*., et al.* A virtual geographic environment for debris flow risk analysis in residential areas. *Isprs Int Geo-Inf* **2017**, *6*, 377.

120. Schelling, P.K.; Phillpot, S.R.; Keblinski, P. Comparison of atomic-level simulation methods for computing thermal conductivity. *Physical Review B* **2002**, *65*, 144306.

121. Ebel, B.A.; Loague, K. Physics-based hydrologic-response simulation: Seeing through the fog of equifinality. *Hydrological Processes* **2006**, *20*, 2887-2900.

122. Olsen, K.; Madariaga, R.; Archuleta, R.J. Three-dimensional dynamic simulation of the 1992 landers earthquake. *Science* **1997**, *278*, 834-838.

123. Newton, I.; Streater, J.; Royal, S. *Philosophia naturalis principia mathematica.* 1687.

124. Oberkampf, W.L.; Trucano, T.G. Verification and validation in computational fluid dynamics. *Prog Aerosp Sci* **2002**, *38*, 209-272.

125. Millington, I. *Game physics engine development.* CRC Press: 2007.

126. Bourg, D.M.; Bywalec, B. *Physics for game developers: Science, math, and*

code for realistic effects. " O'Reilly Media, Inc.": 2013.

127. Corporation, N. Physx sdk. https://developer.nvidia.com/physx-sdk

128. Colinvella. Collision response. https://en.wikipedia.org/wiki/Collision_response

129. Boeing, A.; Bräunl, T. In *Evaluation of real-time physics simulation systems*, Graphite, 2007; pp 281-288.

130. Erez, T.; Tassa, Y.; Todorov, E. In *Simulation tools for model-based robotics: Comparison of bullet, havok, mujoco, ode and physx*, 2015 IEEE international conference on robotics and automation (ICRA), 2015; IEEE: pp 4397-4404.

131. Norton, T. *Learning c# by developing games with unity 3d.* Packt Publishing Ltd: 2013.

132. Maciel, A.; Halic, T.; Lu, Z.; Nedel, L.P.; De, S. Using the physx engine for physics-based virtual surgery with force feedback. *The International Journal of Medical Robotics and Computer Assisted Surgery* **2009**, *5*, 341-353.

133. Zhonghua, L.; Sankaranarayanan, G.; Deo, D.; Dingfang, C.; De, S. In *Towards physics-based interactive simulation of electrocautery procedures using physx*, 2010 IEEE Haptics Symposium, 25-26 March 2010, 2010; pp 515-518.

134. Wang, D.; Zhang, L.; Wang, M.; Xiao, T.; Hou, Z.; Zou, F. A simulation system based on ogre and physx for flexible aircraft assembly. In *Proceedings of the 2012 ACM/IEEE/SCS 26th Workshop on Principles of Advanced and Distributed Simulation*, IEEE Computer Society: 2012; pp 171-173.

135. Mart, J.C.; #237; nez-Franco; David; #193; lvarez-Mart; #237; nez. Physx as a middleware for dynamic simulations in the container loading problem. In *Proceedings of the 2018 Winter Simulation Conference*, IEEE Press: Gothenburg, Sweden, 2018; pp 2933-2940.

136. Robertson, P.A. Factors affecting tree growth on three lowland sites in southern illinois. *Am Midl Nat* **1992**, 218-236.

137. Stage, A.R. An expression for the effect of aspect, slope, and habitat type on tree growth. *Forest Sci* **1976**, *22*, 457-460.

138. Kaufmann, M.R.; Ryan, M.G. Physiographic, stand, and environmental effects on individual tree growth and growth efficiency in subalpine forests. *Tree Physiol* **1986**, *2*, 47-59.

139. Chapman, H.H. *Forest mensuration.* J. Wiley & sons, Incorporated: 1924.

140. Tonge, R. Collision detection in physx. *Recent Advances in Real-Time Collision and Proximity Computations for Games and Simulations. SIGGRAPH* **2010**.

141. Corporation, N. Rigid body dynamics. https://docs.nvidia.com/gameworks/content/gameworkslibrary/physx/guide/Manual

/RigidBodyDynamics.html#applying-forces-and-torques

142. Guarnieri, A.; Vettore, A.; Pirotti, F.; Menenti, M.; Marani, M. Retrieval of small-relief marsh morphology from terrestrial laser scanner, optimal spatial filtering, and laser return intensity. *Geomorphology* **2009**, *113*, 12-20.

143. Olofsson, K.; Holmgren, J.; Olsson, H. Tree stem and height measurements using terrestrial laser scanning and the ransac algorithm. *Remote Sens-Basel* **2014**, *6*, 4323-4344.

144. Yao, T.; Yang, X.; Zhao, F.; Wang, Z.; Zhang, Q.; Jupp, D.; Lovell, J.; Culvenor, D.; Newnham, G.; Ni-Meister, W. Measuring forest structure and biomass in new england forest stands using echidna ground-based lidar. *Remote Sens Environ* **2011**, *115*, 2965-2974.

145. Technologies, U. Unity user manual (2018.2). https://docs.unity3d.com/Manual/UnityManual.html

146. Technologies, U. Scenes. https://docs.unity3d.com/Manual/CreatingScenes.html

147. Zhang, C.; Chen, T. In *Efficient feature extraction for 2d/3d objects in mesh representation*, Proceedings 2001 International Conference on Image Processing (Cat. No. 01CH37205), 2001; IEEE: pp 935-938.

148. Åkerblom, M. Quantitative tree modeling from laser scanning data. **2012**.

149. Technologies, U. Tree editor. https://docs.unity3d.com/Manual/class-Tree.html

150. Rusu, R.B.; Cousins, S. In *Point cloud library (pcl)*, 2011 IEEE International Conference on Robotics and Automation, 2011; pp 1-4.

151. Schroeder, W.J.; Martin, K.M.; Lorensen, W.E. In *The design and implementation of an object-oriented toolkit for 3d graphics and visualization*, Proceedings of Seventh Annual IEEE Visualization'96, 1996; IEEE: pp 93-100.

152. Hackenberg, J.; Spiecker, H.; Calders, K.; Disney, M.; Raumonen, P. Simpletree-an efficient open source tool to build tree models from tls clouds. *Forests* **2015**, *6*, 4245-4294.

153. MACHADO, S.d.A.; Nadolny, M. In *Comparação de métodos de cubagem de árvores e de diversos comprimentos de seção*, Anais do III Congresso Florestal e do Meio Ambiente do Paraná, 1991; Associaçáo Parananense de Engenheiros Florestais Curitiba,, Brazil: pp 89-104.

154. Mestre, S.; Veye, F.; Perez-Martin, A.; Behar, T.; Triboulet, J.; Berron, N.; Demattei, C.; Quéré, I. Validation of lower limb segmental volumetry with hand-held, self-positioning three-dimensional laser scanner against water displacement. *Journal of Vascular Surgery: Venous and Lymphatic Disorders* **2014**, *2*, 39-45.

155. Damstra, R.J.; Glazenburg, E.J.; Hop, W.C.J. Validation of the inverse water volumetry method: A new gold standard for arm volume measurements. *Breast Cancer Research and Treatment* **2006**, *99*, 267.

156. Maniatis, D.; Saint André, L.; Temmerman, M.; Malhi, Y.; Beeckman, H. The potential of using xylarium wood samples for wood density calculations: A comparison of approaches for volume measurement. *Iforest* **2011**, *4*, 150.

157. Hifi, M.; M'hallah, R. A literature review on circle and sphere packing problems: Models and methodologies. *Advances in Operations Research* **2009**, *2009*.

158. Archer, T.; Whitechapel, A. *Inside c#*. Microsoft Press Redmond, MA: 2002; Vol. 1.

159. Scherzer, D.; Bagar, F.; Mattausch, O. Volumetric real-time water and foam rendering. *GPU Pro 360 Guide to Rendering* **2018**, 189.

160. Horvath, C.J. In *Empirical directional wave spectra for computer graphics*, Proceedings of the 2015 Symposium on Digital Production, 2015; ACM: pp 29-39.

161. Bridson, R. *Fluid simulation for computer graphics*. AK Peters/CRC Press: 2015.

162. Dullweber, A.; Leimkuhler, B.; McLachlan, R. Symplectic splitting methods for rigid body molecular dynamics. *The Journal of chemical physics* **1997**, *107*, 5840-5851.

163. Technologies, U. Physics.

164. Goldstein, H.; Poole, C.; Safko, J. Classical mechanics. American Association of Physics Teachers: 2002.

165. Technologies, U. Rigidbody.

166. Corporation, N. Rigid body collision. https://docs.nvidia.com/gameworks/content/gameworkslibrary/physx/guide/Manual/RigidBodyCollision.html#broad-phase-algorithms

167. Corporation, N. Geometry queries. https://docs.nvidia.com/gameworks/content/gameworkslibrary/physx/guide/Manual/GeometryQueries.html

168. Technologies, U. Mesh collider. https://docs.unity3d.com/Manual/class-MeshCollider.html

169. Huang, W.; Yu, L. Serial symmetrical relocation algorithm for the equal sphere packing problem. *arXiv preprint arXiv:1202.4149* **2012**.

170. Latifi, H.; Fassnacht, F.E.; Müller, J.; Tharani, A.; Dech, S.; Heurich, M. Forest inventories by lidar data: A comparison of single tree segmentation and metric-based methods for inventories of a heterogeneous temperate forest. *Int J Appl Earth Obs* **2015**, *42*, 162-174.

171. Chopra, A.; Town, L.; Pichereau, C. *Introduction to google sketchup*. John Wiley & Sons: 2012.

172. Wong, L. A review of daylighting design and implementation in buildings. *Renewable and Sustainable Energy Reviews* **2017**, *74*, 959-968.

173. Konstantoglou, M.; Tsangrassoulis, A. Dynamic operation of daylighting and shading systems: A literature review. *Renewable and Sustainable Energy Reviews* **2016**, *60*, 268-283.

174. Wang, S. Revit RiZhaoDaShi. http://arcdot.com/

175. Girardeau-Montaut, D. Cloudcompare-open source project. *OpenSource Project* **2011**.

176. Rusu, R.B.; Marton, Z.C.; Blodow, N.; Dolha, M.; Beetz, M. Towards 3d point cloud based object maps for household environments. *Robot Auton Syst* **2008**, *56*, 927-941.

177. Disney, M.; Raumonen, P.; Lewis, P. In *Testing a new vegetation structure retrieval algorithm from terrestrial lidar scanner data using 3d models*, 2012.

178. Wang, S.; Hong, B. Optimum design of tilt angle and horizontal direction of solar collectors under obstacle's shadow for building applications. *Journal of Building Construction and Planning Research* **2015**, *3*, 60.

179. Runkle, J.R. Gap regeneration in some old-growth forests of the eastern united states. *Ecology* **1981**, *62*, 1041-1051.

180. Nicotra, A.B.; Chazdon, R.L.; Iriarte, S.V. Spatial heterogeneity of light and woody seedling regeneration in tropical wet forests. *Ecology* **1999**, *80*, 1908-1926.

181. Giday, K.; Aerts, R.; Muys, B.; Troyo-Dieguez, E.; Azadi, H. The effect of shade levels on the survival and growth of planted trees in dry afromontane forest: Implications for restoration success. *J Arid Environ* **2019**, *170*, 7.

182. Vanhove, W.; Vanhoudt, N.; Van Damme, P. Effect of shade tree planting and soil management on rehabilitation success of a 22-year-old degraded cocoa (theobroma cacao l.) plantation. *Agr Ecosyst Environ* **2016**, *219*, 14-25.

183. Ashton, M.S.; GUNATILLEKE, C.S.; GUNATILLEKE, I.N.; Griscom, H.P.; Ashton, P.S.; Singhakumara, B.M. The effect of shade on leaf structure and physiology of tree seedlings from a mixed dipterocarp forest. *Botanical Journal of the Linnean Society* **2011**, *167*, 332-343.

184. Zeng, W.; Tomppo, E.; Healey, S.P.; Gadow, K.V. The national forest inventory in china: History-results-international context. *For. Ecosyst.* **2015**, *2*, 23.

185. Bienert, A.; Hess, C.; Maas, H.-G.; Von Oheimb, G. A voxel-based technique to estimate the volume of trees from terrestrial laser scanner data. *International Archives of the Photogrammetry, Remote Sensing & Spatial Information Sciences*

2014, *45*.

186. Blain, J.M. *The complete guide to blender graphics: Computer modeling & animation*. AK Peters/CRC Press: 2016.

187. Krooks, A.; Kaasalainen, S.; Kankare, V.; Joensuu, M.; Raumonen, P.; Kaasalainen, M. Predicting tree structure from tree height using terrestrial laser scanning and quantitative structure models. *Silva Fenn* **2014**, *48*.

188. Santoro, M.; Beer, C.; Cartus, O.; Schmullius, C.; Shvidenko, A.; McCallum, I.; Wegmüller, U.; Wiesmann, A. Retrieval of growing stock volume in boreal forest using hyper-temporal series of envisat asar scansar backscatter measurements. *Remote Sens Environ* **2011**, *115*, 490-507.

189. Eberle, J.; Clausnitzer, S.; Hüttich, C.; Schmullius, C. Multi-source data processing middleware for land monitoring within a web-based spatial data infrastructure for siberia. *Isprs Int Geo-Inf* **2013**, *2*, 553.

190. Stelmaszczuk-Górska, M.; Thiel, C.; Schmullius, C. Remote sensing for aboveground biomass estimation in boreal forests. *Earth Observation for Land and Emergency Monitoring* **2017**, 33-55.

191. Gao, T.; Zhu, J.; Deng, S.; Zheng, X.; Zhang, J.; Shang, G.; Huang, L. Timber production assessment of a plantation forest: An integrated framework with field-based inventory, multi-source remote sensing data and forest management history. *Int J Appl Earth Obs* **2016**, *52*, 155-165.

192. Roşca, S.; Suomalainen, J.; Bartholomeus, H.; Herold, M. Comparing terrestrial laser scanning and unmanned aerial vehicle structure from motion to assess top of canopy structure in tropical forests. *Interface Focus* **2018**, *8*, 20170038.

193. Zhao, F.; Guo, Q.H.; Kelly, M. Allometric equation choice impacts lidar-based forest biomass estimates: A case study from the sierra national forest, ca. *Agr Forest Meteorol* **2012**, *165*, 64-72.

194. Fortier, J.; Truax, B.; Gagnon, D.; Lambert, F. Allometric equations for estimating compartment biomass and stem volume in mature hybrid poplars: General or site-specific? *Forests* **2017**, *8*, 23.

Curriculum Vitae

Personal information:

Name: Zhichao Wang	**M/F:** Male
Date of Birth: 16/03/1987	**Nationality:** Chinese

Education:

Jan 2014 - Now	Ph.D. Candidate	Lehrstuhl Fernerkundung, Institut für Geographie, Friedrich-Schiller-Universität Jena	Jena, Germany
Sep 2010 - Jul 2013	M.Sc. in Geography	School of Forestry, Beijing Forestry University	Beijing, China
Sep 2005 - Jul 2009	B.Sc. in GIS	School of Information Engineering, China University of Geoscience (Beijing)	Beijing, China

Theoretical discovery:

Computational Virtual Measurement For Trees

Manuscripts in preparation:

From Single Vector Information to Virtual Geographic Environments (VGEs), the Potential of Applying LiDAR as the Exclusive Data Source for National Forest Inventories
Zhichao Wang and Christiane Schmullius

Computational Virtual Measurement I: An Exploratoryy Virtual Water Displacement Method for Single Tree Stem Volume Estimation
Zhichao Wang, Yan-Jun Shen, Xiaoyuan Zhang and Christiane Schmullius

The Improvement for Virtual Water Displacement Method Using Single Virtual Water Molecule
Zhichao Wang and Christiane Schmullius

Computational Virtual Measurement for Light Condition of Single Tree
Zhichao Wang, Xiaoyuan Zhang, Jun Zheng, Jia Wang and Christiane Schmullius

Publications (in Chinese with English abstract)

Study on Stem Form Index Based on Non-destructive Precision Measurement through Electronic Theodolite
Gao Xiang,Feng Zhongke,**Wang Zhichao**,Xu Weiheng,Cao Zhong,He Tengfei
Transactions of the Chinese Society for Agricultural Machinery, **2015**,46(1):299-305.

Measuring method of tree height and volume using total station under canopy cover condition
Jihong, S.; Hongjiang, Z.; Chao, S.; **Zhichao, W**
Transactions of the Chinese Society of Agricultural Engineering **2014**, 30, 182-190

Integrated indoor and field forest measurement by using total station
Wang Z C, Feng Z K Yan F, Wang M Y
Journal of Northwest Forestry University, **2013**,28(6),134-138

Canopy interception of different forest types in the three gorges region of yangtze river
Zhao, F.; Feng, Z.; Gao, X.; Zheng, J.; **Wang, Z**
Science of Soil and Water Conservation **2008**, 15

Selbständigkeitserklärung

Ich erkläre, dass ich die vorliegende Arbeit selbständig und unter Verwendung der angegebenen Hilfsmittel, persönlichen Mitteilungen und Quellen angefertigt habe.

Ort, Datum   Unterschrift der Verfasserin/des Verfassers